TÉCNICO LISBOA

Aeroelastic Analysis of Nonlinear High Aspect Ratio Wings

Christian Spada

Thesis to obtain the Master of Science Degree in

Aerospace Engineering

Supervisor: Prof. Afzal Suleman

Examination Committee

President:	Prof. Filipe Szolnoky Ramos Pinto Cunha
Supervisor:	Prof. Afzal Suleman
Member of the Committee:	Dr. José Lobo do Vale

October 2014

Abstract

Nowadays the aeronautic industry struggles with the demand to enhance flight efficiency and to reduce emissions at the same time. One solution for reducing fuel consumption is increasing wing aspect ratio since it improves the lift-to-drag ratio. Nevertheless, higher deflections are expected, which may lead to relevant nonlinear aeroelastic behavior. In this work, a reference regional aircraft wing structural layout is designed to ensure structural integrity for a load limit of 3.8 g's. A scaled model that represents well the aeroelastic behavior is required for wind tunnel testing to evaluate the nonlinear behavior that can occur in high aspect ratio wings. For this purpose, two classical scaling methodologies were employed. These methodologies use scaling factors that are derived from the governing aeroelastic equations of motion. The first does a direct modal response matching, while the second uncouples the mass and stiffness distribution to achieve the modal response. The scaled structure design parameters are optimized to obtain the target scaled values. The methodologies are compared and the achieved configuration that better represents the full model behavior is selected. A new nonlinear aeroelastic scaling methodology was developed, which uses two different optimization routines to match the nonlinear static response and the mode shapes of the full model. This is the first demonstration of an optimization that simultaneously combines *Equivalent Static Loads* (*ESL*) for matching the nonlinear full model response with structural dynamic for high aspect ratio wings. Results show marked improvement when applying this approach to design the scaled model.

Keywords

High aspect ratio wings, Aeroelastic Analysis, Flutter speed, Aeroelastic Scaling, Equivalent Static Loads (ESL), Nonlinear structural effects.

Abstract - Portuguese

Atualmente a indústria aeronáutica sofre pressões para simultaneamente melhorar a eficiência de voo e reduzir as emissões poluentes. Uma possível solução passa por aumentar a razão de aspeto da asa, uma vez que aumenta o coeficiente de planeio. Contudo, são expectáveis deformações elevadas que poderão levar ao aparecimento de comportamentos aeroelásticos não-lineares relevantes. Nesta tese, a estrutura de uma asa de referência de uma aeronave regional é desenha de forma a suportar uma carga limite de 3.8 g's. É necessário um modelo à escala reduzida para estudar o comportamento aeroelástico não-linear de asas alongadas em túnel de vento. Para este propósito duas metodologias clássicas são empregues, as quais usam fatores de escala que derivam das equações que governam a aeroelasticidade. A primeira iguala diretamente a resposta modal, enquanto a segunda desacopla as distribuições de massa e rigidez para atingir a resposta modal. Em ambas, parâmetros estruturais de desenho são otimizados para obter os valores escalonados alvos. As metodologias são comparadas e do estudo é escolhida a configuração que melhor representa o comportamento aeroelástico do modelo real. Uma nova metodologia de escalonamento aeroelástico não-linear foi desenvolvida, usa duas rotinas diferentes de otimização para igualar a resposta estática não-linear e os modos de vibração do modelo real. É a primeira demostração de uma otimização que simultaneamente combina Carregamentos Estáticos Equivalentes para igualar a resposta não-linear do modelo real com a estrutura dinâmica para asas alongadas. Os resultados mostram melhoramentos quando aplicada esta abordagem para o desenho de um modelo à escala.

Palavras-chave

Asas Alongadas, Análise Aeroelástica, Velocidade de *Flutter*, Escalonamento Aeroelástico, Carregamentos Estáticos Equivalentes, Efeitos estruturais não lineares.

Abstract - Italian

Oggigiorno l'industria aeronautica deve contemporaneamente soddisfare requisiti quali migliorare l'efficienza del volo e ridurre l'inquinamento. Una possibile soluzione è quella di incrementare l'allungamento alare in quanto ciò comporta un aumento del rapporto portanza su resistenza. Tuttavia, ciò potrà causare grandi deformazioni responsabili di un possibile comportamento aeroelastico non lineare della struttura. In questo elaborato la struttura alare di un velivolo da trasporto regionale è stata progettata per un carico limite uguale a 3.8g. È necessario costruire un modello in scala, che rappresenti bene il comportamento aeroelastico dell'ala, per poter effettuare un test in galleria del vento e valutare possibili comportamenti non lineari della struttura reale. Per questa ragione due diverse metodologie classiche di ridimensionamento aeroelastico sono state impiegate. Queste metodologie utilizzano fattori di scala che derivano dalle equazioni che governano l'aeroelasticità. La prima uguaglia la risposta modale del modello reale direttamente; mentre la seconda la ottiene attraverso un disaccoppiamento della distribuzione delle masse e delle rigidezze. I parametri di progetto della struttura scalata sono ottimizzati per ottenere i valori target cercati. Entrambe le metodologie vengono confrontate per scegliere la configurazione scalata che meglio approssima il comportamento aeroelastico della struttura reale. Una nuova metodologia di ridimensionamento aeroelastica non lineare è stata implementata utilizzando due diverse routine, la prima verifica la risposta statica non lineare tra i due modelli mentre la seconda confronta le corrispettive forme modali. Questo è il primo studio di ottimizzazione condotto per velivoli con grandi allungamenti alari che utilizza gli Equivalent Static Loads per ottenere la stessa risposta aeroelastica tra il modello scalato e quello reale. I risultati mostrano che utilizzando questa nuova metodologia è possibile ottenere un modello scalato che approssimi meglio il comportamento aeroelastico della struttura reale.

Parole chiave

Grande allungamento alare, Analisi Aeroelastica, Velocità di flutter, Ridimensionamento aeroelastico, Equivalent Static Loads (ESL), Effetti strutturali non lineari.

Acknowledgments

I start this dissertation by acknowledgements those who helped me the past four and half years. I'm sincerely grateful to *Marco S., Luca, and Margherita* for their great patience and support during the years that I attended the Politecnico of Torino.

I would like to thank Prof. *Gianfranco Chiocchia* who gave me the opportunity to attend an Erasmus double degree project at IST in Lisbon. I'm sincerely grateful to Prof. *Afzal Suleman* which gave me the chance to collaborate with his research team at IST in Lisbon. I would also like to thank *José Vale*, *Frederico Afonso* and *Gonçalo Leal* for their kind guidance and indispensable assistance during this study.

I have to give a special thanks to my girlfriend, *Stefania*, to take care of me and loved every day. I would like to thank all my family for their support and love. I especially want to thank my dad and mom, *Nicola* and *Catia*, for their frequent encouragement and support for all the events occurred in my life, and my brother, *Fabrizio*, for his optimism and cheerfulness. Finally, not least, I want to thank my Friends (*Pietro, Sebastiano, Maurizio, Valerio, Marco F.*) that make life more fun and enjoyable.

Contents

List of Figures

List of Tables

List of Symbols

Chapter 1

AR	Aspect ratio
b	Span
C_D	Drag coefficient
C_{D0}	Profile drag coefficient
C_{Di}	Induced drag coefficient
C_L	Lift coefficient
e'	Span efficiency factor, which is unity if the wing planform is elliptical
w_{max}	Tip deflection

Chapter 3

b	Span/Reference length
F	Force
f	Natural frequency
Fr	Froude number
g	Gravitational acceleration
L, S, C_L	On equation 3.7 correspond to lift, wing area and lift coefficient respectively
M	Represents overall mass in Equation 3.5
M,L,T	Represent Mass, Length and Time units
n_F	Force ratio
n_f	Frequency Ratio
n_g	Length scale
n_M	Mass Ratio
n_v	Velocity Ratio
n_ρ	Air density Ratio
V	Velocity of the aircraft
X	Vector of translational degrees of freedom
θ	Vector of rotational degrees of freedom
ρ	Air density
$[K_{ij}]$	Block matrix terms in stiffness matrix
$[M_{ij}]$	Block matrix terms in inertia/mass matrix
$[Q_{ij}]$	Block matrix of aerodynamic terms

Chapter 4

$\bar{c}$	Reference length
f	Objective function
g	Damping
g, h and *w*	On Equation 4.17 correspond to State variables
H	Hessian
k	Reduced frequency
n	Number of design variables
$n_1 + n_2 + n_3$	On Equation 4.17 correspond to number of state variables restraints
p	Complex eigenvalue = $w(\gamma \pm i)$
q	Flight dynamic pressure
u_k	Aerodynamic box and body degrees of freedom
u_p	Physical degrees of freedom
u_{pa}	Union of u_k and u_{ps}
u_{ps}	Union of $u_{sa}$and u_p
u_{sa}	Permanently constrained degrees of freedom associated with aerodynamic grid points
V	Velocity
x	Vector indicating the design variables
x_0	Initial estimate of the design variables
$[A]$	Real matrix in the PK-method
$[A_{jj}]$	Aerodynamic influence coefficient matrix, a function of Mach number and reduced frequency
$[B_{hh}]$	Modal damping matrix
$[D^1_{jk}], [D^2_{jk}]$	Real and Imaginary parts of substantial differentiation matrix
$\{f_j\}$	Pressure on lifting element *j*
$\{F_k\}, \{F_g\}$	On Equation 4.6 correspond to aerodynamic forces and their structurally equivalent values respectively
$[G_{ka}]$	Spline matrix reduced to a-set
$[K_{hh}]$	Modal stiffness matrix
$[M_{hh}]$	Modal mass matrix
$[Q_{hh}]$	Merged aerodynamic matrix
$[Q^I_{hh}]$	Modal aerodynamic damping matrix
$[Q^R_{hh}]$	Modal aerodynamic stiffness matrix
$[Q_{ie}]$	Generalized aerodynamic matrix for aeroservoelastic analyses.
$[Q_{ii}]$	Generalized aerodynamic matrix
$[Q_{kk}]$	Aerodynamic influence matrix

$[S_{kj}]$	Integration matrix
$\{u_h\}$	Modal amplitude vector
$\{u_k\}, [G_{kg}], \{u_g\}$	On Equation 4.5 correspond to deflections of the aerodynamic grid points, interpolation matrix and structural grid point deflections
$\{u_k\}, \{P_k\}$	Displacements and Forces at aerodynamic grid points
$\{w_j\}$	Downwash
$\{w_j^g\}$	Static aerodynamic downwash; it includes, primarily, the static incidence distribution that may arise from an initial angle of attack, camber, or twist
$[WTFACT]$	A matrix of empirical correction factors to adjust each theoretical aerodynamic box lift and moment to agree with experimental data
γ	Transient decay rate coefficient
ρ	Fluid density
λ	Lagrange multipliers
$[\Phi_{ai}]$	A matrix of i-set normal mode vectors in the physical a-set

Chapter 5

AR	Aspect ratio of the wing
AR_{boxes}	Aspect ratio of the aerodynamic boxes
b	Total span
b_1, b_2	Represent the distance between the root to the break section and between the break to the tip section respectively
$C_{L\alpha}$	Lift curve slop
C_{Lq}	It represents the slope of the curve $\Delta C_L = f(q)$
$C_{M\alpha}$	Pitch stiffness
C_{Mq}	It represents the slope of the curve $\Delta C_M = f(q)$
c	Local chord
$\bar{c}$	Reference chord
c_b	Break chord
c_r	Root chord
c_t	Tip chord
F	Correction factor
f	Natural frequency
f_{FL}	Flutter frequency
g	Damping
M	Mach number
M.A.C.	Mean Aerodynamic Chord
NC	Number of chordwise

ND	No flutter speed
NS	Number of spanwise
n_z	Load factor
q	Pitch angular velocity
S	Wing aria
V, f	On Equation 5.8 correspond to freestream speed and maximum frequency of interest
V_D	Dive speed
V_{DIV}	Divergence speed
V_{EAS}	Equivalent airspeed
V_{FL}	Flutter speed
V_{max}	Minimum flutter speed
W_{engine}	Engine weight
W_{TO}	Take-off weight
w	Circular natural frequency
y	Spanwise distance from the root section
z	Altitude
Λ_{LE}	Sweep angle
Γ	Dihedral angle
ϑ_y	Twist angle
ϑ_x	Bending angle
Δx	Box chord requirement
Δy	Box span requirement
$[M]$	Mass matrix
$[K]$	Stiffness matrix
$\{\Phi\}$	Eigenvector or mode shape

Chapter 6

AA,BB,...,ZZ	Weight parameters for the objective function
b	Semi-span
c	Local chord
C_L	Lift coefficient
F	Force
f	Natural frequency
f_{FL}	Flutter frequency
f	On Equation 6.2 correspond to Objective function
h	Hour

M	Overall mass
M,L,T	On Section 6.3.1 represent Mass, Length and Time units
n_F	Force ratio
n_f	Frequency Ratio
n_g	Length scale
n_M	Mass Ratio
n_P	Pressure Ratio
n_v	Velocity Ratio
n_ρ	Air density Ratio
OM	Overall mass
P	Pressure
R_1, R_2, R_3	Rotation along the x, y and z body axis of the structural model respectively
RMS	Rotational mode shape
T_1, T_2, T_3	Translation along the x, y and z body axis of the structural model respectively
TMS	Translational mode shape
V	Velocity of the aircraft
V_{FL}	Flutter speed
w	Tip deflection
ρ	Air density
[K]	Stiffness matrix
[M]	Mass matrix
[Q]	Aerodynamic matrix

Chapter 7

f_{FL}	Flutter frequency
h	Hour
n_g	Length scale
V_{FL}	Flutter speed
w	Tip deflection
ε	Tolerance parameter
$\{d\}$	Current or initial design
$\{F\}$	Load conditions
$\{F_{eq}\}$	Equivalent load
$[K_{NL}]$	Nonlinear stiffness matrix
$[K_{Lin}]$	Linear stiffness matrix
$\{x_{NL}\}$	Nonlinear static deformations
$\{x_{Lin}\}$	Linear static deformations

Chapter 8

f, b, V	On Equation 8.1 correspond to natural frequency, span and velocity of the aircraft
Fr	Froude number
k	Reduced frequency

Notation

Chapter 3 - 6 - 7

$_s$	Scaled model
$_f$	Full scale model

Chapter 4

$\overline{\ }$	Overbars represent the upper limit
$\underline{\ }$	Underbars represent the lower limit

Chapter 5

$_r$	Reference wing
$_n$	New wing

Chapter 1

HIGH ASPECT RATIO WINGS

1.1 Introduction

In recent years, especially for civil and commercial aircraft, the trend is to design aircraft with high aspect ratio wings. This trend occurs because this configuration offers great advantages.

In general high aspect ratio wings produces more lift and provide aircraft with a higher lift-to-drag ratio and endurance flight [1]. To make the concept feasible in terms of weight restrictions, these wings are very flexible. High aspect ratio wings increase efficiency because they produce less induced drag leading to lower fuel consumptions. The total drag coefficient (see *Equation 1.1*) can be defined as:

$$C_D = C_{D0} + C_{Di} = C_{D0} + \frac{C_L^2}{\pi \cdot e' \cdot AR}$$

Equation 1.1: Total drag coefficient

where:

C_{D0}	Profile drag coefficient
C_{Di}	Induced drag coefficient
C_L	Lift coefficient
e'	Span efficiency factor, which is unity if the wing planform is elliptical
AR	Aspect ratio

Note that the induced drag, which is mainly due to the presence of the wing tip trailing vortex, can be decreased by increasing the aspect ratio.

Nevertheless this challenge requires detailed studies due to large deformations under normal operating loads leading to a geometrical nonlinear behavior and aeroelastic problems [13].

These large deformations can change the natural frequencies of the wing which can produce noticeable changes in its aeroelastic behavior [11]. It is known that rigid-body modes couple with low elastic modes as the wing flexibility increases for highly flexible aircraft [59, 60]. Therefore a nonlinear structural static analysis is required in order to investigate the nonlinearities associated with the structure. When the structural model is subject to large deformations, geometrical nonlinearities has to be taken into account in aeroelastic analysis.

Jinwu *et al.* [30] summarizes the progress and the challenges in nonlinear aeroelasticity in aircraft. Moreover Cooper *et al.* [13] and Bhasin *et al.* [6] explain how to implement geometrical nonlinearities in the design of high aspect ratio wings. The internal structure of the wing must be designed to be stiff enough in order to avoid aeroelastic problems during the entire mission profile of the aircraft [41].

In order to better understand the physical behavior of the wing without building an expensive full scale demonstrator, a reduced scale model must be designed. Experimental testing of aeroelastically scaled models is a common undertaking for flight vehicle development programs [22].

The key objective is to verify the predicted aeroelastic characteristics of the aircraft. In some cases, the objective is simply to validate computational models. For these cases, the model needs only to represent the full-scale vehicle in a qualitative sense. In other cases, the scaled model is intended to closely reproduce the aeroelastic response of the full scale model [22]. This more general form of the aeroelastic model design problem is the one addressed in this work.

Aeroelastic scaling requires consideration of aerodynamic and structural physics. Aerodynamic similitude is achieved analytically. Flight conditions such as airspeed and altitude are selected for matching scaled parameters like Froude number and density ratio, for example. Structural similitude is not realistically achievable by geometrically scaling the structural components. Corresponding analytical scaling requirements will generally specify that a geometrically scaled structure should be made from materials that have unobtainable properties. There is also a high probability that the manufacturing techniques used for the full scale design cannot be duplicated at a smaller scale. The only feasible option is to redesign the internal structure and optimize it such that its scaled mass and stiffness properties are consistent with the full-scale aircraft [50]. The ladder structure is one of several scaled model configurations recommended by Bisplinghoff *et al.* [7].

In the classical approach, aeroelastic scaling is achieved by selection of a discrete subset and modal degrees of freedom that capture the relevant global properties of the full model, and optimizing the scaled aircraft such that the nondimensional modal masses and stiffness coefficients match the full-scale aircraft.

From the governing equations of linear elasticity, it can be proved that every model, which has the same scaled geometry and the same scaled mass and stiffness distributions, will result in the same modal response of the full scale aircraft, after suitable scaling [48].

The most common practice for classical aeroelastic scaling is to use a truncated number of the vibration mode shapes from the target full scale model as the modal degrees of freedom for the scaled model optimization [2, 51]. There is although a drawback, the truncation may omit information that becomes important when geometric nonlinearity is significant (the truncation can be considered analogous to not modeling certain flexibilities such as axial and/or shear).

Classical scaling methods have worked in practice for traditional applications, but the validity of the modeling assumptions needs verification for cases where geometric nonlinearities are important.

1.2 Motivation

Consider the scenario illustrated in *Figure 1.1*. Engineers have developed a high-fidelity computational model representing a full scale concept. The full scale model has a wingspan value of *b*. Wind tunnel size, cost, or safety considerations favor scaled aeroelastic testing rather than full scale testing. A half-span test article is built. Certain aeroelastic response quantities must be scaled in similar conditions.

Static displacement is easy visualized in *Figure 1.1*, for instance if the full scale model has a predicted tip deflection w_{max}, the half-span model should have tip deflection $w_{max}/2$ in scaled conditions.

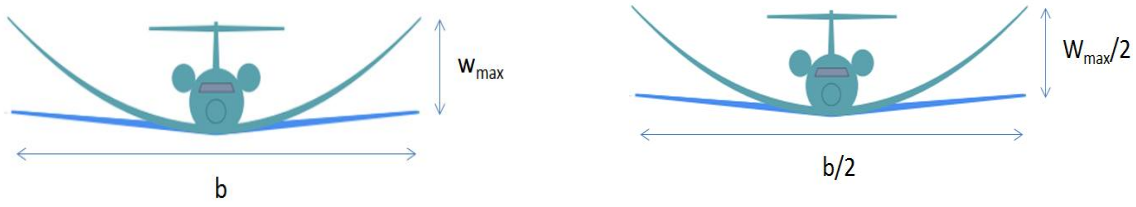

(a): Full Scale concept *(b): Scaled concept*

Figure 1.1: Full scale and scaled aircraft with predicted tip deflection [50]

An aeroelastic methodology must be developed to produce a scaled model that closely replicates the target aeroelastic behavior of the full model.

The main goals of this dissertation are to become familiarized with the aeroelastic study of high aspect ratio wings including geometric nonlinearity through the use of *MSC Nastran*™ software and with the aeroelastic scaling, exploring different methodologies to attain aeroelastic similitude between a scaled model and the full scale model.

A method that uses an optimization routine coupling *MSC Nastran*™ software and *Matlab*™ has been developed with the goal of designing a scaled wind tunnel model that reproduces the same aeroelastic behavior of the full model.

Nonlinear scaling methodologies are needed for designing a scaled wind tunnel model, which requires a nonlinear aeroelastic response that is representative of the full scale design.

1.3 Geometric Nonlinearity

In classic aeroelastic theory, linear assumptions are made for the aerodynamics and the structures, and the aeroelastic problem reduces to the solution of a set of linear equations that can be easily solved [15]. However, when the airspeed increases to high subsonic or transonic speeds, the linear assumption usually leads to results with insufficient accuracy.

With the application of stronger, lighter and more flexible synthetic materials, high aspect ratio wings may exhibit large deformation under aerodynamic loads, and geometrical nonlinearities have to be taken into account when modeling the structure.

With structural nonlinearities, aeroelastic system may exhibit a variety of phenomena such as LCO and chaotic vibration [30].

The geometric nonlinearity of interest is due to nonlinear strain-displacement kinematics and follower forces. Coupling between stiffness and internal loads is an important nonlinear kinematic effect. Although, geometric nonlinearities were not considered in their development, traditional scaled model design methodologies do not include geometric nonlinearities other than coupling between stiffness and internal loads.

Structural nonlinearities could appear from damaged hinges of control surfaces, loose control linkages, and material behavior as well as various other sources [30]. Both old and combat aircraft, which carry heavy external stores, are more prone to present structural nonlinear effects.

Structural nonlinearities may be classified as being either distributed or concentrated. In general, distributed structural nonlinearities are governed by elasto-dynamic deformations that affect the whole structure. Concentrated nonlinearities, on the other hand, act locally and are commonly found in control mechanisms or in the connecting parts between wing, pylon, engine or external stores [33].

1.4 Related Scaling Work

The foundations of dimensional analysis began with Fourier in the early nineteenth century.

Rayleigh *et al.* [58] developed the method of dimensions showing that the period of small amplitude vibrations are proportional to $\mathrm{time}^{-0.5}, \mathrm{mass}^{0.5}$ and $\mathrm{length}^{0.5}$. He observed that proportionally held regardless the units.

Buckingham in 1914 presented the π theorem [9]. It's a formalization of Rayleigh's method of dimensional analysis. The π theorem provides a method for computing sets of dimensionless parameters from a giving set of variables, even if the form of the equation is still unknown. However, the choice of dimensionless parameters is not unique and not always the solution chosen is the best.

In 1955 Bisplinghoff *et al.* [7] published *Aeroelasticity*, which also remains a classic book for the study of aeroelastic problems. The book documents classical structural and aerodynamic methods for fundamental aeroelastic analysis. It provides essential guidance on classic aeroelastic model theory, model design and construction, and testing techniques.

French *et al.* [20] used an optimization process in order to design an aeroelastically scaled model. The stiffness of a low aspect ratio wind tunnel model was designed to match the stiffness of a target model. The optimization minimized the structural weight while satisfying displacement matching constraints.

French *et al.* [22] modified the work presented in reference [20] in order to include scaling for dynamic aeroelasticity. A two-step optimization procedure was used. First, the wing structure was designed to minimize the differences in scaled static deflections between the design and target model. Then, assuming the stiffness

design was complete and accurate, nonstructural masses were designed by constraining the reduced modal frequencies to match while minimizing the differences in mode shapes.

Pereira *et al.* [48] developed a scaling methodology for a joined-wing wind tunnel model. The scaled structure was designed by optimizing the scaled natural frequencies of the model to match the full-scale design. Normalized flutter speed of the scaled model matched the full scale aircraft, but the aeroelastic frequencies did not match around or above flutter speed.

Bond *et al.* [8] demonstrated that matching scaled natural frequencies alone is insufficient when one wants to include geometric nonlinearities. Scaling the first buckling eigenvalue together with the natural frequencies and mode shapes resulted in accurate aeroelastically scaled response in the initial nonlinear range.

Richards *et al.* [53] evaluated two linear scaling methodologies for a joined-wing flight test program. The first methodology used a single-step direct modal matching. Similar to reference [8], natural frequencies and mode shapes were matched in a simultaneous optimization analysis. Design variables included structural stiffness and nonstructural masses. The second method decoupled the stiffness and nonstructural mass design variables. In the first routine the scaled model was designed in order to match the target static deflection. A subsequent optimization analysis matched the natural frequencies and mode shapes by designing nonstructural masses.

Direct optimization of the nonlinear static response is a computationally intensive task. Efficiency can be gained by transformation to an equivalent linear system using the equivalent static loads (ESL) approach [45]. The ESL methodology was originally developed and applied to the joined-wing application by Lee *et al*. [34].

Kim et al. [31] showed that ESL optimization produced a better design that a fully stressed design methodology for a detailed joined-wing case. Ricciardi *et al.* [50] optimized a joined wing structure including geometric nonlinearities using the equivalent static loads and first buckling eigenpair approach respectively. This was the first demonstration of ESL optimization that simultaneously included vibration response. In a 2.5g nonlinear aeroelastic trim maneuver, results including nonlinear effects are considerably more agreeable than the traditionally designed scaled model.

The purpose of this work is to familiarize with the application of modern scaling approaches for high aspect ratio wings including geometric nonlinearities.

1.5 Related Nonlinear Aeroelastic Analysis Development

Nonlinear aeroelastic analysis of high-fidelity structures is not supported by any commercial analysis or released research code.

Commercially available codes like *MSC Nastran*™ and *ZAERO*™ are hugely popular among aeroelasticians due to their ease of modeling and faster analysis using linearized unsteady aerodynamics. Much of the researches in aeroelasticity make use of these commercial codes for generating or validating results.

Several research codes have been developed directly coupling a nonlinear beam element structural model with a linear aerodynamic model.

Patil *et al.* [47] published the NATASHA formulation. Large aircraft motion is coupled with geometrically nonlinear structural deformation subject only to restriction to small strain.

Drela *et al* [17] developed ASWING. The code uses unsteady lifting aerodynamics and a structural model based on geometrically nonlinear isotropic beam analysis.

Patil *et al.* [46] have looked at the effect of structural geometric nonlinearities on the flutter behavior of high aspect ratio wings. A deflection based on constant distributed loading on the wing is calculated and the changes in structural and aeroelastic characteristics are presented. Including geometric nonlinearities there is a significant change in the structural frequencies and thus in the aeroelastic response. This is due to static, dynamic and aeroelastic characteristics of curved wings are affected by curvature-induced changes in the effective bending-torsion coupling and the direction of aerodynamic loading.

Verification of nonlinear aeroelastically designed or scaled models require aeroelastic analysis with high fidelity structural models not limited to beam elements. Options other than beam based structures require in-house development of a tightly coupled aeroelastic code, or in-house development of or integration with a code coupling interface.

Harmin *et al.* [13] evaluated the variation of the flutter speed when geometric nonlinearities are added to the model of a high aspect ratio wing through the use of *MSC Nastran*™ software. This work is used as a guide for the aeroelastic study of the model investigated in this dissertation.

Very few nonlinear aeroelastic models incorporate nonlinear aerodynamics. One such procedure that models both structural and aerodynamic nonlinearities is called ELSTEP/FAT [35]. The nonlinear structural model is coupled with a nonlinear aerodynamic solver to perform a nonlinear aerodynamic and nonlinear structural interaction simulation. However, because of the lack of a full order solution that directly couples a nonlinear dynamic structural solver with a nonlinear aerodynamic solver, this method is difficult to implement.

One goal of this work is to include geometric nonlinearities in the evaluation of the flutter speed through the use of a commercial code, *MSC Nastran*™.

1.6 This Document

In this chapter, high aspect ratio wings concept and classical approach for aeroelastic scaled model design were introduced. Possible limitations of classical methods for geometrically nonlinear applications were identified. Previous work in aeroelastic scaling and nonlinear flutter analysis were reviewed. In order to help the reader, a list of the subsequent chapters and their contents are reported here.

Chapter 2. A brief summary on aeroelastic problems is treated, especially for divergence and flutter phenomenon.

Chapter 3. Two different classical methods have been developed for aeroelastic scaling. The first method match the aeroelastic response directly (Method 1), while the second one match the modal response through a mass and stiffness distributions uncoupling (Method 2).

Chapter 4. In this chapter, the computational tools and scaling methodology developed to design the scaled model are discussed and described.

Chapter 5. In this chapter, the baseline configuration is analyzed. Linear and nonlinear static analyses were performed in order to design the internal configuration of the wing. Nonlinear effects are evaluated and discussed. Modal analysis as well as aeroelastic analysis are done for the wing with full fuel and empty tanks with the objective of verifying if there are occurrences of flutter and divergence phenomenon for different flight conditions.

Chapter 6. The target values for the scaled model are evaluated. Two different approaches (*Configuration 1* and *2*) are proposed in order to build a scaled model. For each approach both classical methods (Method 1 and Method 2) are applied. Differences in terms of global overall error and computational time are evaluated in order to select the best model obtained. Finally, the attention is focused on the aeroelastic analysis of the best scaled wing model and respective comparison with the aeroelastic behavior of the full scale model. This chapter in the scaling process does not take into account nonlinear effects.

Chapter 7. A modern aeroelastic scaling approach using *Equivalent Static Loads (ESL)* was developed in order to improve the results when nonlinear effects act in the structure. The main goal is to compare the differences in terms of global overall error, computational time, flutter speed and frequency error obtained with the same configuration of scaled model (*Configuration 2*) when nonlinear effects are included in the calculation.

Chapter 8. This chapter summarizes the conclusions of this dissertation and shows the differences in the aeroelastic response between the full model and the scaled model obtained using the classical and modern approach (ESL) respectively.

Chapter 2

AEROELASTICITY

2.1 Introduction

Aeroelasticity is the study of the interaction of aerodynamic, elastic and inertia forces for a flexible structure and the phenomena that can result [61]. For fixed wing aircraft there are two key areas:

- Static aeroelasticity - the deformation of the aircraft influences the lift distribution, which can lead to the statically unstable condition of torsional divergence and can reduce the control surface effectiveness, which can even leads to control reversal;
- Dynamic aeroelasticity - includes the critical area of flutter, where the aircraft become dynamically unstable in a condition where the structure extracts energy from the air stream.

Aeroelastic problems would not exist if aircraft structure is perfectly rigid. Modern aircraft structures are very flexible, and this flexibility is fundamentally responsible for various types of aeroelastic phenomena. Structural flexibility itself may not be objectionable. However, aeroelastic phenomena arises when structural deformations induce additional aerodynamic forces. These additional aerodynamic forces may produce additional structural deformations which will induce still greater aerodynamic forces. Such interactions may tend to become smaller and smaller until a condition of stable equilibrium is reached, or they may tend to diverge and destroy the structure. The basic approach to aeroelastic effects is centered on four general areas (see *Figure 2.1*).

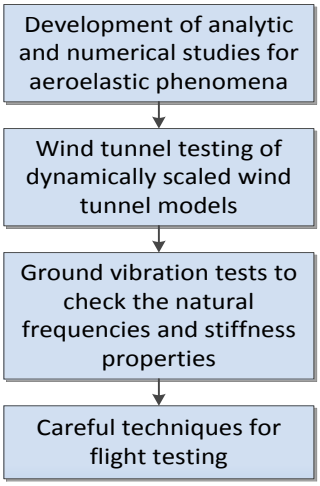

Figure 2.1: Basic approach to aeroelastic effects

Examination of aeroelastic problems on emerging and future flight vehicles can start through the prism of the range of the involved sub-disciplines. Elasticity, aerodynamics, and dynamics are the fundamental building blocks of classic aeroelasticity.

In this work, due to the complexity of the structure in study, it was decided that a commercial code should be used in order to calculate the flutter speed and characteristics. The program used to perform these tasks was the *MSC Nastran*™ software, which integrates the essential disciplines required by aeroelastic design and analysis.

2.2 Static Aeroelasticity

Static aeroelasticity is the study of flexible aircraft structures under aerodynamic loads, where the forces and motions are considered to be independent of time. Aerodynamic lift and moment cause the wing to bend and twist.

The interaction between the wing structural deformations and the aerodynamic loads determines the wing bending and twist at each flight condition, and must be considered in order to model the static aeroelastic behavior.

Through the elimination of time-dependent forces and motion, the inertial forces can be ignored in the equilibrium equations as these are dependent upon acceleration. Also, only steady aerodynamic forces need to be included in the analysis. Consequently, the modeling of static phenomena is much easier than dynamic aeroelastic phenomena where unsteady aerodynamic effects must be considered.

There are two critical static aeroelastic phenomena that can be encountered, namely torsional divergence and control reversal. Divergence occurs when the moments due to aerodynamic forces overcome the restoring moments due to structural stiffness, so resulting in structural failure. Aileron control reversal occurs when the rolling moment caused by the aileron stops producing a rolling moment of expected signal and starts producing a rolling moment of opposite signal.

In modern aircraft, the flutter speed is usually reached before the divergence speed so divergence is not normally a problem. However, the divergence speed is a useful measure of the general stiffness of the aircraft structure.

2.2.1 Divergence

Divergence can be exemplified easily considering *Figure 2.2* that represents the increase of wing incidence due to wing twist.

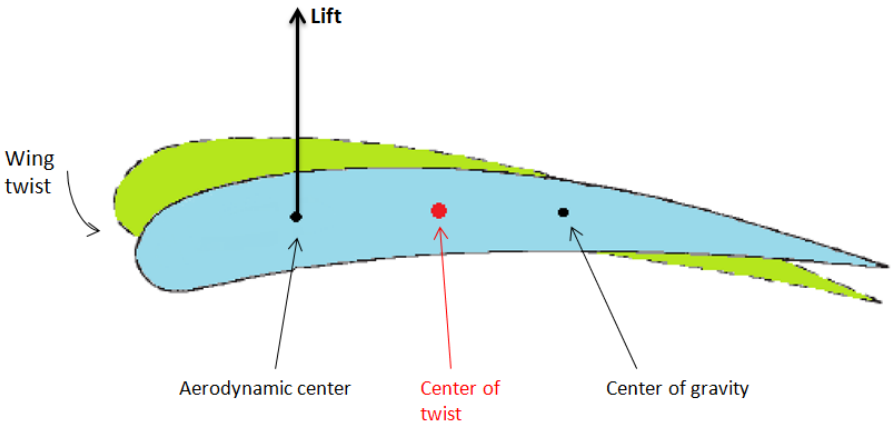

Figure 2.2: Increase of wing incidence due to wing twist

The moment of the lift vector about the center of twist causes an increase in wing incidence which produces a further increase in lift, leading to another increment in incidence so on [40].

At speeds below a critical value, called divergence speed, the increments in lift converge to a condition of stable equilibrium in which the torsional moment of the aerodynamic forces about the center of twist is balanced by the torsional rigidity of the wing. In the opposite case, speed above the divergence speed, the wing will exhibit a divergent behavior, causing structural failure.

One can understand that the divergence speed will be higher for wings with greater torsional stiffness or with the aerodynamic center closer to the twist center; these are important factors indeed to consider in the structural project.

Most aircraft are designed with swept-back wings. The reason for this are mainly aerodynamic, since for subsonic aircraft by sweeping back the wing the airspeed at which shock waves are formed on the wings increases, so delaying the associated increase in drag. Supersonic aircraft are designed with the wings swept inside the Mach cone, which also decreases the associated wave drag. Wright and Cooper *et al.* [61] explain that the divergence speed increases with swept-back wings and decreases for the swept-forward case. This reduction of the divergence speed becomes the limiting case for sweep-forward designs and consequently very few exist.

2.3 Dynamic Aeroelasticity - Flutter

So far, when considering static aeroelastic effects (see Section 2.2), the aerodynamic surfaces are in a steady condition and so the resulting forces and moments are steady (i.e constant with time). However, for flutter, maneuver and gust response analyses the behavior of aerodynamic surfaces under dynamic motion is required.

Flutter is arguably the most important of all the aeroelastic phenomena and is the most difficult to predict. It is an unstable self-excited vibration in which the structure extracts energy from the air stream and often results in catastrophic structural failure. Classical binary flutter occurs when the aerodynamic forces associated with motion in two modes of vibration cause the modes to couple in an unfavorable manner. In aircraft design, flutter is a critical parameter that must be considered in the early stages of design cycle.

At a critical speed, known as flutter speed, the structure sustains oscillations following some initial disturbance. Below this speed the oscillations are damped, whereas above it one of the modes becomes negatively damped and unstable oscillations occur. Flutter can take various forms involving different pair of interacting modes, e.g. wing bending/torsion, wing torsion/control surface, etc.

Flutter, like other aeroelastic phenomenon, is very sensitive to the structure normal modes of vibration.

Some indication of the physical nature of wing bending-torsion flutter may be given from an examination of aerodynamic and inertia forces during a combined bending and torsional oscillation in which the individual motion are 90° out of phase. In a pure bending or pure torsional oscillation the aerodynamic forces produced by the effective wing incidence oppose the motion; the geometric incidence in pure bending remains constant and therefore does not affect the aerodynamic damping force, while in pure torsion the geometric incidence produces aerodynamic forces which oppose the motion during one half of the cycles but assist it during the other half so that the overall effect is nil. Thus, pure bending or pure torsional oscillations are quickly damped out. This is not the case in the combined oscillation when the maximum twist occurs at zero bending and vice versa; that is, a 90° phase difference [40].

The type of flutter described above, in which two distinctly different types of oscillating motion interact such that the resultant motion is divergent, is known as classical flutter. Other types of flutter may involve only one type of motion, in which examples are the stalling flutter and aileron buzz. Stalling flutter of a wing occurs at a high incidence where, for particular positions of the spanwise axis of twist, self-excited twisting oscillations occur which, above a critical speed, diverge. Aileron buzz occurs at high subsonic speeds and is associated with the shock wave on the wing forward of the aileron.

Chapter 3

AEROELASTICITY SCALING MODEL

3.1 Introduction

Examination of the current state of the art in ground and flight testing in the last 30 years reveal major progress in instrumentation, communication, computer power, and associated system identification methods. Nevertheless a number of significant challenges still remain in the area of wind-tunnel testing. Proper scaling laws must be developed. Despite major progress in excitation techniques, instrumentation, data processing, and system identification technology, flutter flight testing is still dangerous, time consuming, and expensive.

Testing aeroelastically scaled wind-tunnel models is a common task in aircraft development programs. The object of the testing is often to validate the numerically predicted aeroelastic characteristics of an entire aircraft or some component of it. The scaled model must represent the full scale model in a qualitative sense. Quite often, though, the scaled model is intended to exactly model the response of the full scale structure. This is the most general form of the aeroelastic model design problem and it is the one addressed here.

A method that uses a numerical optimization approach to design an aeroelastically scaled wind tunnel model has been developed. In an aeroelastically scaled model the static deflection and modal behavior are related to that of a full size model by simple scaling rules. The model designer must produce a structure that matches predetermined deflections, mass, natural frequencies and mode shapes.

The design of a wind tunnel model is fundamentally different of a full scale structure design. The wind tunnel model designer must design a structure that has a predetermined set of stiffness and mass properties. The desired geometry, stiffness and mass characteristics of the wind tunnel model are scaled from the full size model. A properly designed model will display the same aeroelastic behavior as the baseline model, with flutter velocity and vibrational frequencies varying by the scale factors that will be presented in this chapter.

The model similarity laws and scaling ratios depend on the testing conditions, as well as on the full size flight condition as discussed by Bisplinghoff *et al.* [7]. Statically, the stiffness of the model is chosen to show the same relative deformation during testing as the full size aircraft at the corresponding fight condition. The dynamic similarity laws require that the natural frequencies and the mode shapes are preserved. Also, the total mass needs to be accurately scaled.

3.2 Physics Model

Due to the fact of the complex nature of the problem and to the limited time and resources, a simplified physics model was chosen: the small disturbance, linear potential partial differential equations (PDE) [52]. This model reduces the degrees of freedom into only two: displacement and rotation;

$$\begin{bmatrix} M_{11} & M_{12} \\ M_{21} & M_{22} \end{bmatrix} \begin{Bmatrix} \ddot{X} \\ \ddot{\theta} \end{Bmatrix} + \begin{bmatrix} K_{11} & K_{12} \\ K_{21} & K_{22} \end{bmatrix} \begin{Bmatrix} X \\ \theta \end{Bmatrix} = \frac{\rho \cdot V^2}{2} \begin{bmatrix} b^2 & 0 \\ 0 & b^3 \end{bmatrix} \begin{bmatrix} Q_{11} & Q_{12} \\ Q_{21} & Q_{22} \end{bmatrix} \begin{Bmatrix} X \\ \theta \end{Bmatrix}$$

Equation 3.1: Small Disturbance, Linear Potential Partial Difference Equations (PDE)

where:

X	Vector of translational degrees of freedom
θ	Vector of rotational degrees of freedom
M_{ij}	Block matrix terms in inertia/mass matrix
K_{ij}	Block matrix terms in stiffness matrix
b	Reference length
Q_{ij}	Block matrix of aerodynamic terms

Even though these physics are limited, the PDE equations are adequate for a low-cost exploration of flight mechanics in real world conditions. In terms of dimensions of the fundamental quantities (Mass (M), Length (L) and Time (T)) the system of equations (see *Equation 3.1*) takes the form:

$$\begin{bmatrix} M & M \cdot L \\ M \cdot L & M \cdot L^2 \end{bmatrix} \begin{Bmatrix} L \cdot T^{-2} \\ T^{-2} \end{Bmatrix} + \begin{bmatrix} M \cdot T^{-2} & M \cdot L \cdot T^{-2} \\ M \cdot L \cdot T^{-2} & M \cdot L^2 \cdot T^{-2} \end{bmatrix} \begin{Bmatrix} L \\ ND \end{Bmatrix} = M \cdot L^{-1} \cdot T^{-2} \begin{bmatrix} L^2 & 0 \\ 0 & L^3 \end{bmatrix} \begin{bmatrix} L^{-1} & ND \\ L^{-1} & ND \end{bmatrix} \begin{Bmatrix} L \\ ND \end{Bmatrix}$$

Equation 3.2: PDE system in terms of M,L,T dimensions [12]

where ND signifies non-dimensional.

In this work it is only analyzed the free vibration case, so the right part of the *Equation 3.1* disappear and the system of equations become:

$$\begin{bmatrix} M_{11} & M_{12} \\ M_{21} & M_{22} \end{bmatrix} \begin{Bmatrix} \ddot{X} \\ \ddot{\theta} \end{Bmatrix} + \begin{bmatrix} K_{11} & K_{12} \\ K_{21} & K_{22} \end{bmatrix} \begin{Bmatrix} X \\ \theta \end{Bmatrix} = \begin{Bmatrix} 0 \\ 0 \end{Bmatrix}$$

Equation 3.3: Free-vibrations System of Equations

3.3 Scaling Factors

The geometrically scaled model is constrained by a set of scaling parameters, used to map the full scale test point, stiffness, mass and geometry to the reduced scale test point. These scaling factors are derived from non-dimensional parameters, which appear in the equations that govern the aerodynamics, the structure and their coupling. These scaling parameters are subject to constraints posed by the wind tunnel or environment in which the model will operate.

For the purpose of obtaining a non-dimensional set of equations the designer has to choose three primary quantities, which are the only parameters that can be changed. There is a great range of choices that could be made, however only one combination is investigated here which is the combination selected for this work [2]:

- the span *b* (based on the desired reduced scale span; it is due to wind tunnel constraints);
- air density *ρ* (it is due to environmental constraints);
- velocity *V* (it is due to wind tunnel constraints).

These are the primary quantities used in the Buckingham π theorem that is applied to the other important properties, which are needed for a good dynamic similitude between full scale and reduced size models.

The equation above (see *Equation 3.3*) could be rewrite in terms of dimensionless form (see *Equation 3.4*).

$$\frac{1}{\rho \cdot b^2}\begin{bmatrix} M_{11} & M_{12}\cdot b \\ M_{21}\cdot b & M_{22}\cdot b^2 \end{bmatrix}\begin{Bmatrix} \ddot{X}\cdot\frac{b}{V^2} \\ \ddot{\theta}\cdot\left(\frac{b}{V}\right)^2 \end{Bmatrix} + \frac{1}{\rho \cdot b \cdot V^2}\begin{bmatrix} K_{11} & \frac{K_{12}}{b} \\ \frac{K_{21}}{b} & \frac{K_{22}}{b^2} \end{bmatrix}\begin{Bmatrix} X \\ \frac{b}{\theta} \end{Bmatrix} = \begin{Bmatrix} 0 \\ 0 \end{Bmatrix}$$

Equation 3.4: Dimensionless PDE system

The dimensionless parameters can be used to form/determine the scaling factors. The first three scaling factors (see *Table 3.1*) appear directly from the primary quantities. Note that the subscripts of *s* and *f* represent scaled and full scale respectively.

Scaling Factors	
Length Scale	$n_g = \frac{b_s}{b_f}$
Air Density Ratio	$n_\rho = \frac{\rho_s}{\rho_f}$
Velocity Ratio	$n_v = \frac{V_s}{V_f}$

Table 3.1: Scaling factors: Length scale, Air Density ratio, Velocity ratio

It misses the mass and frequency scaling factors. Traditionally the approach that is made in order to scale the mass is to attain the non-dimensional relationship of some reference mass (e.g. total mass) of the aircraft with that of the air [7]. So it can be written similarly to the dimensionless parameter obtained after apply the Buckingham π theorem to M_{11} which has units of Mass (M).

$$\left(\frac{M}{\rho \cdot b^3}\right)_s = \left(\frac{M}{\rho \cdot b^3}\right)_f \rightarrow n_M = \frac{M_s}{M_f} = \left(\frac{b_s}{b_f}\right)^3 \cdot \left(\frac{\rho_s}{\rho_f}\right) = n_g^3 \cdot n_\rho$$

Equation 3.5: Mass Ratio Scaling Factor

This is a fine approach for the determination of the overall mass, however, when it is applied to internal structure, which could differ from the scaled model to the full size aircraft, the results are not good.

To obtain the frequency scale it is needed to apply the Buckingham π theorem to *f*, which has units of T^{-1}, using the primary quantities *V* and b.

$$\left(\frac{f \cdot b}{V}\right)_s = \left(\frac{f \cdot b}{V}\right)_f \rightarrow n_f = \frac{f_s}{f_f} = \left(\frac{V_s}{V_f}\right) \cdot \left(\frac{b_f}{b_s}\right) = \frac{n_v}{n_g}$$

Equation 3.6: Frequency Ratio Scaling Factor

The velocity is a "free-parameter", however it must be constrained by the requirement that both the full scale and the scaled model operate at the same trim state, *i.e.*, the same C_L. Therefore form the lift equation the velocity is evaluated:

$$\frac{L_s}{L_f} = \frac{\left(\frac{\rho \cdot V^2 \cdot S \cdot C_L}{2}\right)_s}{\left(\frac{\rho \cdot V^2 \cdot S \cdot C_L}{2}\right)_f} = n_\rho \cdot n_v^2 \cdot n_g^2$$

$$\frac{L_s}{L_f} = \frac{W_s}{W_f} = n_M$$

$$n_M = n_\rho \cdot n_v^2 \cdot n_g^2 \rightarrow n_v = \frac{V_s}{V_f} = \sqrt{\frac{n_M}{n_\rho \cdot n_g^2}}$$

Equation 3.7: Velocity Scaling Factor

The Froude number is a ratio between inertial and gravitational forces and in turn determines the ratio of deflections due to gravity compared to those due to aerodynamic forces. In many cases, the deflection due to gravity can be assumed insignificant compared to aerodynamic forces. If this assumption is valid the Froude number can be ignored (often the case in wind tunnel). However, in the case of the unconstrained model in free flight, the Froude number may play a more significant role [52]. In order to maintain a similitude of Froude number, the following ratio (see *Equation 3.8*) must be maintained:

$$\left(\frac{V}{\sqrt{b \cdot g}}\right)_s = \left(\frac{V}{\sqrt{b \cdot g}}\right)_f$$

Equation 3.8: Froude number

Additional scale factors could be added in order to achieve a more representative model, leading to lower errors between the design scaled model and the full model. The load applied to the structure has units of force ($M \cdot L \cdot T^{-2}$) and applying the Buckingham π theorem, the force ratio become:

$$\left(\frac{F}{\rho \cdot V^2 \cdot b^2}\right)_s = \left(\frac{F}{\rho \cdot V^2 \cdot b^2}\right)_f \rightarrow n_F = \frac{F_s}{F_f} = \left(\frac{\rho_s}{\rho_f}\right) \cdot \left(\frac{V_s}{V_f}\right)^2 \cdot \left(\frac{b_s}{b_f}\right)^2 = n_\rho \cdot n_v^2 \cdot n_g^2$$

Equation 3.9: Force Ratio Scaling Factor

The task of matching the Reynolds number at a desired velocity-altitude is a difficult one. It requires that the viscosity of the surrounding medium be changed, which in most cases is not easily accomplished. For this reason the matching of the Reynolds number will likely not be satisfied. Although this may seem of concern, experience has shown that it is generally of minor importance as far as aeroelastic effects for main lifting surfaces are concerned [49].

The scaling based on simplified physic model permit a reduction of the model restrictions, which would be much more complex if it was chosen a scaling based on the Navier-Stokes equations.

3.4 *Dynamic* Scaling Methodologies

The goal in this section is to replicate the structural properties of the full scale model by matching the dimensionless mass and stiffness properties. One design approach for developing accurate mass and stiffness distributions is to scale down the exact geometry of the full scale model.

Unfortunately, this is not practical for several reasons. For instance, the manufacture of scaled components may be very expensive and in some cases impossible due to their small resulting sizes.

There is the need to find an alternative to the exact scaling of the full scale model geometry in order to achieve a match between the two models mass and stiffness distributions while at the same time ensuring manufacturability [51].

From the governing equations of linear elasticity, it can be proved that every model, which has the same scaled geometry and the same scaled mass and stiffness distributions, will result in the same modal response (mode shapes and frequencies) as those of the full model, after appropriate scaling.

By designing a model with similar modal response to the full model, similarity of the mass and stiffness distributions will be achieved independent of internal structure. This allows a simplified internal structure to be employed. Due to material and manufacturing constraints not all the components of the full model are scaled with the same material.

In reference [21] it is profoundly discussed the advantages of the use of a physical parameter based optimization over the use of other methods. This method consists on the updating of the physical model properties (e.g. spar height or thickness), which will became design variables in an optimization routine.

From the full scale models are obtained the target values that should be attained by the scaled models. To achieve the target values two different classical scaling methodologies can be used.

The first match the modal response directly (Method 1) while the second one match the modal response through a mass and stiffness distributions uncoupling (Method 2) [52]. In *Figures 3.1* and *3.2* are shown the Method 1 and the Method 2 diagram respectively.

The design optimization used in Method 1 match directly the modal response (frequencies and mode shapes) in just one routine. First of all the input data is passed to the geometry, which is built, next a mesh is generated before performing a modal analysis from which it is attained the modal results. Then it is calculated the modal results errors that are the state variables and take part in the objective function to be minimized. When the objective error margin and convergence are achieved after performing a design optimization, the results are saved.

Method 2 assumes that a similarity of modal responses will be attained if the mass and stiffness distributions are matched separately. Here the stiffness distribution is achieved by reproducing a given set of displacements under a known load using an optimization routine which updates the element sizes of the FEM model. Then the static deflection error is calculated, which is the unique state variable of the design optimization that is applied and also the only parameter that takes part of the objective function to be minimized in the first routine. When the structure stiffness is achieved, concentrated masses can be added to attain the desired mass distribution. So the modal analysis is performed, from which is obtained the modal results and calculated the respective errors. The errors are the state variables of the design optimization process and take also part of the objective function to be minimized in the second routine. Once the objective modal result errors and convergence are achieved the final results are saved.

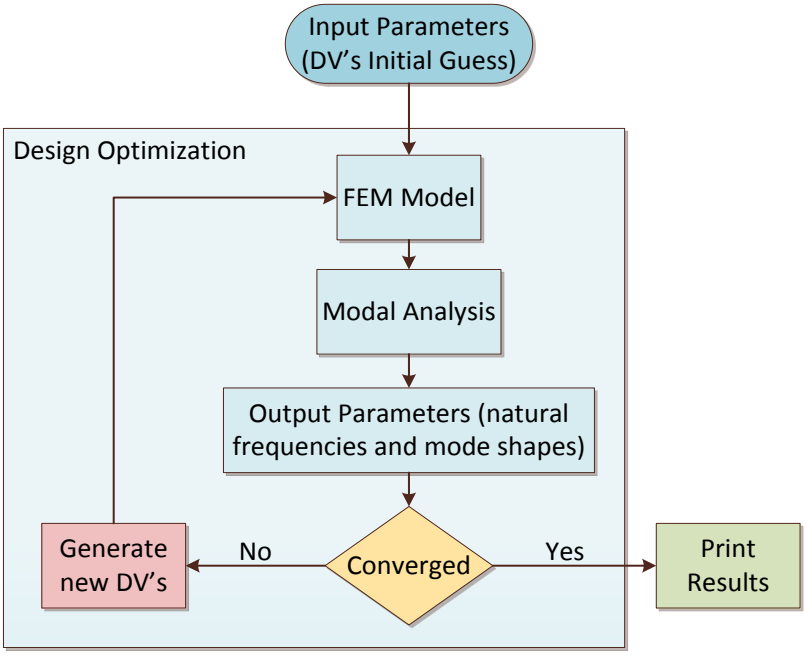

Figure 3.1: Method 1

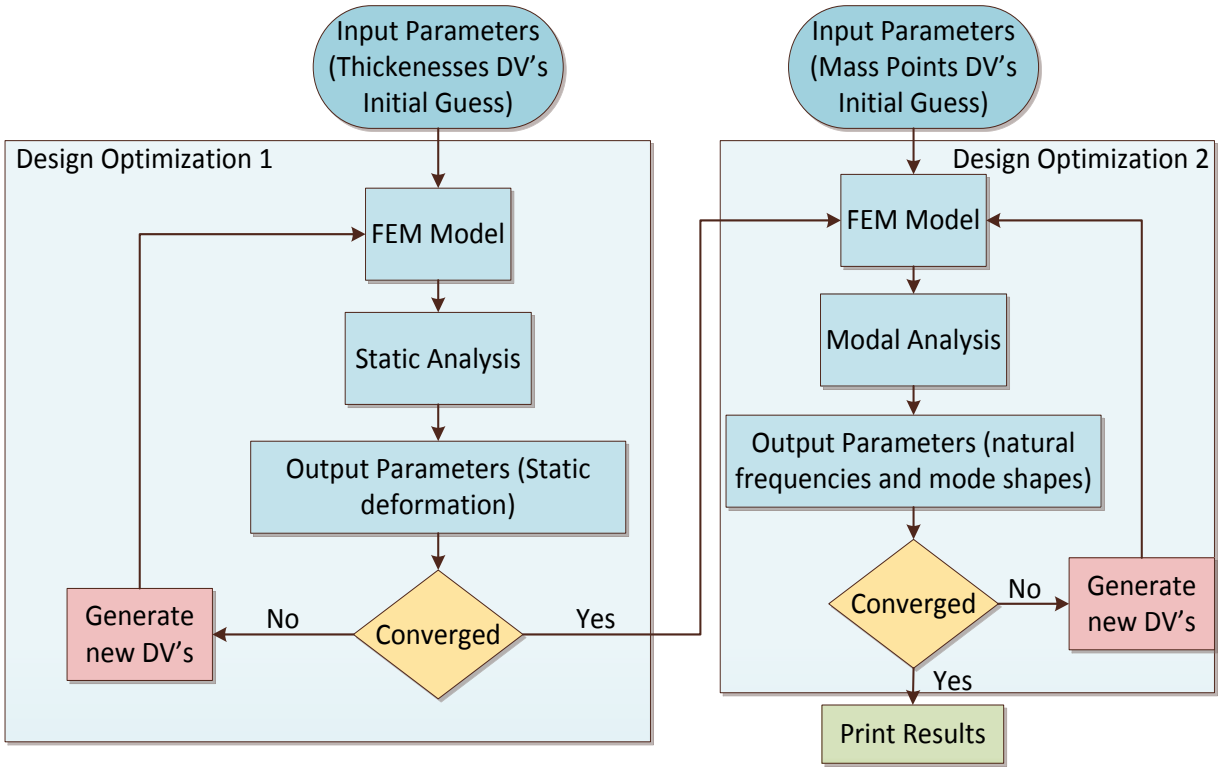

Figure 3.2: Method 2

3.5 Summary of Scale Factors

The scaling factors that were introduced in this chapter are summarized in *Table 3.2*. Note that the subscripts of *s* and *f* represent scaled and full scale respectively.

Scaling Factors	
Length Scale	$n_g = \frac{b_s}{b_f}$
Air Density Ratio	$n_\rho = \frac{\rho_s}{\rho_f}$
Velocity Ratio	$n_v = \frac{V_s}{V_f}$
Mass Ratio	$n_M = \frac{M_s}{M_f} = n_g^3 \cdot n_\rho$
Frequency Ratio	$n_f = \frac{f_s}{f_f} = \frac{n_v}{n_g}$
Force Ratio	$n_F = \frac{F_s}{F_f} = n_\rho \cdot n_v^2 \cdot n_g^2$

Table 3.2: Scaling factors

Chapter 4

COMPUTATIONAL TOOLS

4.1 Introduction

The objective of this chapter is to introduce the computational tools and the methodology used to simulate and analyze the structural model. The structural model consists on a finite element model done in *MSC Nastran*™ software and aerodynamic model uses a Doublet Lattice Method (DLM) also in *MSC Nastran*™. All the aeroelastic analyses were conducted in *MSC Nastran*™ software as well. A *Matlab*™ code was used to perform the optimized process required for the dynamic scaling of the full model.

Summarizing, this chapter provides an overview of the aeroelastic tools included in *MSC Nastran*™ software explaining mainly the Doublet Lattice Method (DLM) and the PK-method to detect the flutter speed. In addition the optimization process is summarized, listing the steps necessary to perform the optimization using *MSC Nastran*™ and *Matlab*™ softwares.

4.2 Aeroelastic Analysis by MSC Nastran™ software

In this work, because of the structure complexity at study, it was decided that a commercial code will be used in order to calculate the flutter speed. The program code to perform these tasks is the *MSC Nastran*™ software.

MSC Nastran™ aerodynamic analysis is based upon a finite element approach. The finite aerodynamic elements are strips or boxes on which there are aerodynamic forces. These elements are defined by their geometry, their motions and by the degrees of freedom at the aerodynamic grid points.

Doublet Lattice Method (DLM) assumes trapezoidal boxes with sides that are parallel to the airflow. By the use of aerodynamic input data, aerodynamic elements and grid points are automatically generated to help ensuring that many of the theoretical requirements are met.

Aerodynamic calculations are defined using a Cartesian coordinate system. By the usual convention, the flow is in the positive x-direction, and the x-axis of every aerodynamic element must be parallel to the flow in its undeformed position. The structural coordinate system may be defined independently, since the use of the same system for both may place an undesirable restriction upon the description of the structural model.

For dynamic aeroelasticity these aerodynamic degrees of freedom are introduced:

$$\left.\begin{matrix} u_k \\ \left.\begin{matrix} u_{sa} \\ u_p \end{matrix}\right\} u_{ps} \end{matrix}\right\} u_{pa}$$

where:

u_k	Aerodynamic box and body degrees of freedom
u_{sa}	Permanently constrained degrees of freedom associated with aerodynamic grid points
u_p	Physical degrees of freedom
u_{ps}	Union of $u_{sa}$and u_p
u_{pa}	Union of u_k and u_{ps}

Because the grid points defining the structure usually do not coincide with the grid points defining the aerodynamic elements, it is necessary to generate equations for interpolating between the two. This interpolation is a key feature since it allows the choice of structural and aerodynamic elements to be based upon structural and aerodynamic considerations independently.

Unsteady aerodynamic forces are generated when the flow is disturbed by the moving structure, or, as in the case of atmospheric turbulence, when the flow itself is unsteady. In the first case, theory leads to a matrix that relates the forces acting upon the structure due to the deflection of the structure. Methods that involve interactions among aerodynamic elements are available only for steady-state sinusoidal motion. These complex influence coefficient matrices depend upon two parameters of the flow: reduced frequency and Mach number.

MSC Nastran™ software developed several theories, but only the Doublet Lattice Method will be explained in this work (see Section 4.2.1).

The DLM is a panel method for the calculation of aerodynamic loads relatively fast and simple if compared to the modern methods which use unsteady panels or a direct solution of the Navier-Stokes equations. Its use is fully justified in the preliminary stages of an aircraft design, when one needs quick calculations and the accuracy of the geometry and the distribution of masses and stiffnesses is rather low.

4.2.1 Doublet-Lattice Theory

The Doublet-Lattice Method (DLM) can be used for interfering lifting surfaces in subsonic flow. The theory is presented by Albano *et al*. [3] and Giesing *et al*. [24, 25, 26].

The theoretical basis of the DLM is linearized aerodynamic potential theory. The undisturbed flow is uniform and is either steady or varying (gusting) harmonically. The DLM is an extension of the steady Vortex-Lattice Method to unsteady flow.

The method consists in splitting the lifting surface in a finite number of panels. These panels are aligned to the free stream direction. A distribution of doublets (acceleration potential) is placed at each panel, so it is equivalent to a pressure drop between the pressure and suction surface respectively. Each doublet is of unknown oscillating intensity and it is disposed on the line set at a quarter of the chord.

Each panel is divided into trapezoidal boxes which contain a control point placed at the 75% chordwise station and spanwise center of the box (see *Figure 4.1*) in order to evaluate the downwash.

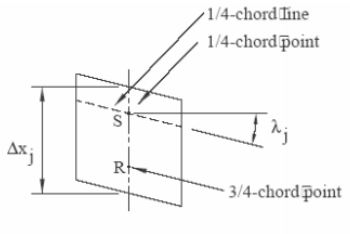

Figure 4.1: Control point [36]

The downwash induced on a panel is given by the contribution of the remaining panels. The assigned value for downwash is for example due to oscillation of the elastic structure itself. Writing these equations for all panels of the model, a set of algebraic equations is obtained. The resolution of these equations allows the calculation of the intensities of doublets, and therefore the evaluation of the pressure drop through the lifting surface. The integration of these pressures on the surface allows the calculation of aerodynamic forces and aerodynamic coefficients of the aircraft.

These are the basic relationship between the lifting pressure and the dimensionless vertical or normal velocity induced by the inclination of the surface to the airstream, i.e., the downwash,

$$\{w_j\} = [A_{jj}]\left\{{}^{f_j}/_{q}\right\}$$

Equation 4.1: Downwash effect

the substantial differentiation matrix of the deflections to obtain downwash,

$$\{w_j\} = \left[D_{jk}^1 + ikD_{jk}^2\right]\{u_k\} + \{w_j^g\}$$

Equation 4.2: Downwash effect evaluated including displacements at aerodynamic grid points

and the integration of the pressure to obtain forces and moments,

$$\{P_k\} = [S_{kj}]\{f_j\}$$

Equation 4.3: Forces at aerodynamic grid points

where:

w_j	Downwash
w_j^g	Static aerodynamic downwash; it includes, primarily, the static incidence distribution that may arise from an initial angle of attack, camber, or twist
f_j	Pressure on lifting element *j*
q	Flight dynamic pressure
k	Reduced frequency
A_{jj}	Aerodynamic influence coefficient matrix, a function of Mach number and reduced frequency
u_k, P_k	Displacements and Forces at aerodynamic grid points
D_{jk}^1, D_{jk}^2	Real and Imaginary parts of substantial differentiation matrix.
S_{kj}	Integration matrix

The three matrices of *Equation 4.1*, *4.2* and *4.3* can be combined to give an aerodynamic influence coefficient matrix:

$$[Q_{kk}] = [S_{kj}][A_{jj}]^{-1}[D_{jk}^1 + ikD_{jk}^2]$$

Equation 4.4: Aerodynamic influence matrix

All aerodynamic methods compute the $[S_{kj}]$, $[D_{jk}^1]$ and $[D_{jk}^2]$ matrices at user-supplied Mach numbers and reduced frequency. The Doublet-Lattice method computes the $[A_{jj}]$ matrix. Then, matrix decomposition and forward and backward substitution are used in the computation of the $[Q_{kk}]$ matrix.

4.2.2 Subsonic Wing-Body Interference Theory

The method of images, with Slender Body Theory, has been added to Doublet-Lattice method (DLM) by Giesing *et al.* [27]. The DLM is used to represent the configuration of interfering lifting surfaces, while Slender Body Theory is used to represent the lifting characteristics of each body (i.e., fuselage, nacelle, or external store).

The primary wing-body interference is modeled by a system of images of the DLM edge vortices and doublets within a cylindrical interference body that circumscribes each slender body.

The secondary wing-body interference that results from the DLM bound vortices and doublets are accounted for by a line of doublets located on the longitudinal axis of each slender body.

The boundary conditions of no flow through the lifting surfaces or through the body lead to equations for the lifting pressures on the surfaces and for the longitudinal (and/or lateral) loading on the bodies in terms of the downwashes on the wing-body combination.

The method of Giesing *et al.* [27] finds the forces on the lifting boxes and bodies of an idealized aircraft in terms of the motions of these elements. The aircraft is modeled with lifting surfaces (wing, tail) and slender body (fuselage, nacelle, or external store). The lifting surfaces are divided into boxes. The bodies are divided into elements. There are two types of body elements: slender elements, which are used to simulate a body's own motion, and interference elements that are used to simulate the interaction with other bodies and lifting surfaces. For more details it is recommended to consult reference [44].

4.2.3 Interconnection of the Structure with Aerodynamics

Structural and aerodynamic grids are connected by interpolation. This allows the independent selection of grid points of the structure and aerodynamic elements of the lifting surfaces/bodies in a manner to better suit the particular theory. Any aerodynamic panel or body can be subdivided into sub regions for interpolation, using a separate function for each. The interpolation method is calling splining. The theory involves the mathematical analysis of beams and plates (see *Figure 4.2*). Three different methods are available:

- linear splines, which are a generalization of an infinite beam and allow torsional as well as bending degrees of freedom;
- surface splines, which are solutions for infinite uniform plates;
- an explicit user-defined interpolation.

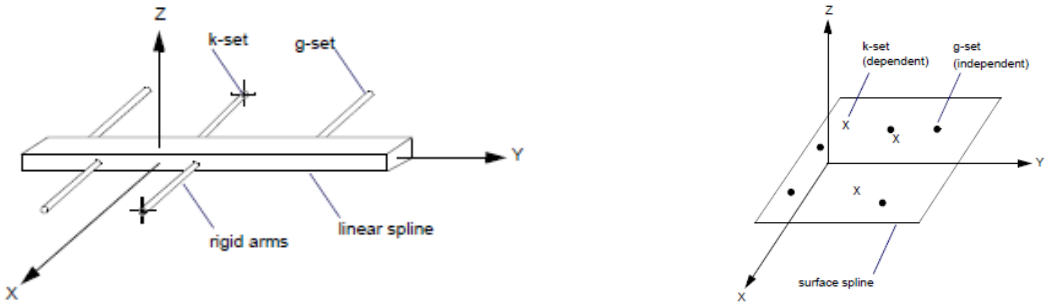

(a): linear spline (b): surface spline

Figure 4.2: Splines and their coordinate systems [44]

Several splines, including combinations of the three types, can be used in one model. The structural degrees of freedom have been chosen in *MSC Nastran*™ software as the independent degrees of freedom; the aerodynamic degreed of freedom are dependent. A matrix is derived that relates the dependent degrees of freedom to the independent ones. Two transformations are required: the interpolation from the structural deflections to the aerodynamic deflections; and the relationship between the aerodynamic forces and the structurally equivalent forces acting on the structural grid points.

The splining methods lead to an interpolation matrix $[G_{kg}]$ that relates the components of structural grid point deflections $\{u_g\}$ to the deflections of the aerodynamic grid points $\{u_k\}$.

$$\{u_k\} = [G_{kg}]\{u_g\}$$

Equation 4.5: Interpolation of the deflections

The derivation of the elements of $[G_{kg}]$ depends on the type of interpolation choice. The transformation between the aerodynamic and structural force systems is found from the requirement that two force systems be "structurally equivalent" rather than statically equivalent. Structural equivalence means that two force systems deflect the structure equally.

$$\{F_g\} = [G_{kg}]^T \{F_k\}$$

Equation 4.6: Interpolation of the forces

$\{F_k\}$ and $\{F_g\}$ are aerodynamic forces and their structurally equivalent values respectively.

4.2.4 Flutter Solution Technique

Flutter is the dynamic aeroelastic stability problem that is obtained when the damping of the system become zero. The manner in which the aerodynamic loads are included in the aerolestatic equations determines the choice of the method to be used. *MSC Nastran*™ software developed three different methods (K, PK, KE) in order to evaluate the flutter speed of an aircraft. Only the PK method is treated in this chapter.

Frazer and Duncan *et al.* [19] in England solved the flutter problem using aerodynamic stability derivatives. This approach introduced the aerodynamic loads into the equations of motion as frequency dependent stiffness and damping terms. In this representation it should be noted that the aerodynamic terms are slowly varying functions of the reduced frequencies. In what has become known as the "British method" of flutter analysis some iteration is still necessary to "line-up" the eigenvalue solution for frequency with the reduced frequency in each mode. A variation of the British method in which the aerodynamic loads are treated as complex springs has been developed by Hassig *et al.* [29]. Hassig called this method PK method, and *MSC Nastran*™ software has adopted his terminology.

4.2.4.1 Generalized Aerodynamic Matrices

Equation 4.4 defines an aerodynamic coefficient matrix $[Q_{kk}]$ that is computed based on the aerodynamic model. For this matrix to be useful in a flutter analysis, two transformations have to take place: the matrices have to be applied to the structural model using the spline techniques; and a modal reduction has to be applied to obtain matrices in generalized form.

Mathematically, those transformations can be expressed as:

$$[Q_{ii}] = [\Phi_{ai}]^T [G_{ka}]^T [WTFACT] [Q_{kk}] [G_{ka}] [\Phi_{ai}]$$

Equation 4.7: Generalized aerodynamic matrix

where:

$[Q_{ii}]$	generalized aerodynamic matrix
$[\Phi_{ai}]$	a matrix of i-set normal mode vectors in the physical a-set

$[G_{ka}]$	spline matrix reduced to a-set
$[WTFACT]$	a matrix of empirical correction factors to adjust each theoretical aerodynamic box lift and moment to agree with experimental data

A level of complexity is added if the flutter analysis includes the use of extra points. Extra points are used for the representation of control systems and are therefore required in aeroservoelastic analyses. In this case a new generalized aerodynamic matrix $[Q_{ie}]$ is computed (see reference [44]).

The flutter analysis then uses a merged matrix:

$$[Q_{hh}] = \begin{bmatrix} Q_{ii} & Q_{ie} \\ 0 & 0 \end{bmatrix}$$

Equation 4.8: Complete generalized aerodynamic matrix

where the *h*-set is a combination of the *i*-set normal modes and the *e*-set extra points. It is seen that the lower *e*-set rows in the matrix are null. Physically, this indicates that the normal mode deflections do not produce aerodynamic forces on the extra points ($Q_{ie} = 0$) and that the extra point deflections do not produce aerodynamic loads on the extra points ($Q_{ee} = 0$).

These aerodynamic matrices are generated for discrete values of Mach number and reduced frequency. The actual flutter analysis is likely to be performed at reduced frequencies (and sometimes Mach numbers) other than one of the available values. These intermediate values are obtained from an interpolation of the available values. PK-flutter method uses a linear spline method for the interpolation scheme.

4.2.4.2 The PK-Method

The fundamental equation for modal flutter analysis by the PK-method (see *Equation 4.9*) is:

$$\left[M_{hh}p^2 + \left(B_{hh} - \frac{1}{4}\rho\bar{c}VQ_{hh}^I/k\right)p + \left(K_{hh} - \frac{1}{2}\rho V^2 Q_{hh}^R\right)\right]\{u_h\} = 0$$

Equation 4.9: Fundamental equation in the PK-method

where:

$[M_{hh}]$	modal mass matrix
$[B_{hh}]$	modal damping matrix
$[K_{hh}]$	modal stiffness matrix
$[Q_{hh}^I]$	modal aerodynamic damping matrix, imaginary parts of $Q_{hh}(m,k)$
$[Q_{hh}^R]$	modal aerodynamic stiffness matrix, real parts of $Q_{hh}(m,k)$
p	complex eigenvalue = $w(\gamma \pm i)$
γ	transient decay rate coefficient
$\bar{c}$	reference length

ρ	fluid density
V	velocity
k	reduced frequency
$\{u_h\}$	modal amplitude vector

Note that the circular frequency and the reduced frequency are not independent since:

$$k = \frac{wc}{2V}$$

Equation 4.10: Reduced frequency

and furthermore, that:

$$k = \left(\frac{c}{2V}\right) Im(p)$$

Equation 4.11: Reduced frequency

For the PK-method of solution, *Equation 4.9* is rewritten in the state-space form with twice the order (see *Equation 4.12*).

$$[A - pI]\{u_h\} = 0$$

Equation 4.12: Fundamental equation rewritten in the state-space form

The eigenvalues of the real matrix $[A]$ are either real or complex conjugate pairs. Real roots indicate a convergence or divergence of the roll subsidence (rigid body) mode or structural (torsional) divergence mode. For the real roots, the damping is expressed as the decay rate coefficient (see *Equation 4.13*).

$$g = 2\gamma = \frac{2p\bar{c}}{(\ln 2)V}$$

Equation 4.13: Damping coefficient

However, the majority of the eigenvalues will be complex conjugate pairs. The oscillatory solutions of *Equation 4.9* require an iterative solution so that *Equation 4.11* is satisfied along with *Equation 4.9*. The roll subsidence root or static structural divergence roots require no iteration but are found by setting $k = 0$. The oscillatory rigid body (i.e., short-period or Dutch-roll) roots and oscillatory roots are found through an algorithm described in reference [44]. This algorithm is based on the desire for capability to determine stability at a given speed independently of the stability at lower or higher speed.

The principal advantage of the PK-method is that it produces results directly for given values of velocity, whereas the K- and KE- methods require iterations to determine the reduced frequency of flutter. In addition,

the damping is given through an iterative process is a more realistic estimate of the physical damping than the parameter *g* in *Equation 4.13*, which is a mathematical artifice.

4.3 Design Optimization

The structural analysis of the model is performed using the finite element method of *MSC Nastran*™ software. It has a computational tool, the Design Optimization that helps to search for an optimum design. However, this tool is difficult to use and is extremely slow, so it was decided to use and optimization process via *Matlab*™ in order to circumvent the limitations of the commercial analysis. Using *Matlab*™*'s fmincon function*, a Sequential Quadratic Programming (SQP) algorithm is used, which is a robust, efficient and reliable gradient-based optimization technique. This *function* finds the minimum of constrained nonlinear multivariable function.

The optimum design process is represented in *Figure 4.3*. It is a coupling between *Matlab*™ and *MSC Nastran*™ software. The first step is to identify the design variables, the function to be minimized (Objective function) and the constraints that must be satisfied (State Variables). In a *Matlab*™ code it is necessary to write a *.bdf file* containing all the data of the problem (i.e grids, elements, properties, constraints, loads). Run *MSC Nastran* directly from *Matlab*™ and achieve the results. At this point the optimization process (*fmincon function*) can be launched. When convergence is achieved and all the constraints are satisfied, the *Matlab*™ code ends and saves the optimized design variables.

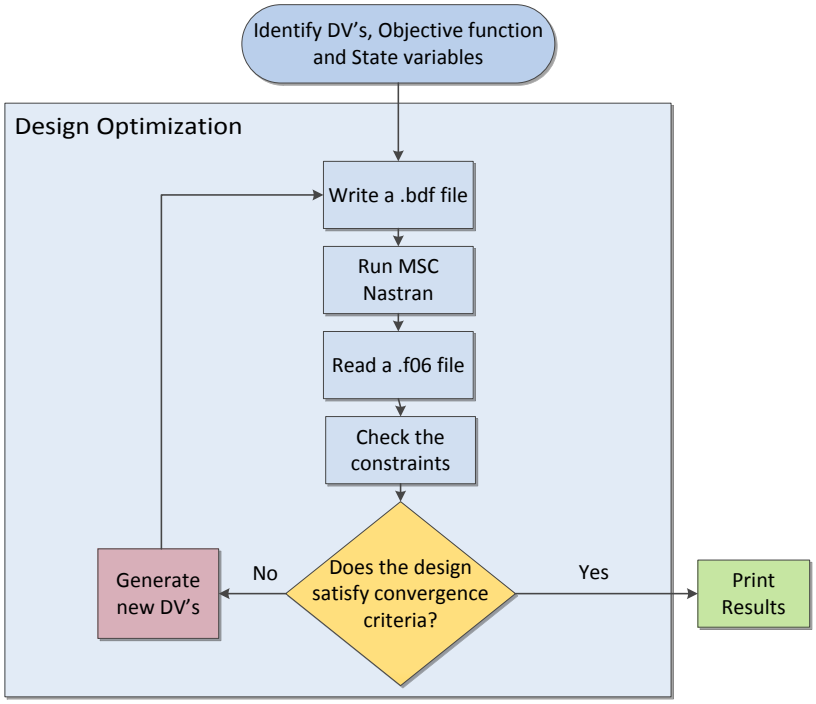

Figure 4.3: Optimization Process

The optimum design signifies that every specified requirement is attained with the minimum cost of certain factors. These factors could be so different such as mass (overall mass for example), dimensions (such as thickness or lengths), natural frequencies, mode shapes, manufacturing costs, displacements of mass points, and so on. All the design parameters can be optimized.

It is the structural optimization that introduces the greatest complexity for physically realizing the scaling requirements when designing the scaled model. The first complication comes from likely structural configuration inconsistency. For example, a full scale model that is designed using skins, spars, and ribs might have a scaled model that uses a ladder structure and skin fairings. When discretized, the finite element models will have different relative node locations and a different number of degrees of freedom. Thus, the discretized aeroelastic equations can never be matched exactly. A globally representative subset of nodes must be selected or interpolated. Once a representative subset is selected, a number of modal masses, modal frequencies and mode shapes can be matched in the optimization process. The number that is matched can only be a truncated number of the total number of eigenpairs for optimization feasibility. Eigenpair truncation is a potential problem for geometrically nonlinear applications. Higher frequency eigenpairs will likely contain flexibility information (for example, axial flexibility) that may be important for geometrically nonlinear applications, especially if there are globally indeterminate load paths.

4.3.1 Introduction to Design Optimization Problem

The Design Optimization of *Matlab*™ software uses three different types of variables in order to obtain the optimum design. These variables are scalar parameters and are the followings:

- Design variables (DV's): independent quantities that are varied in order to achieve the optimum design. Upper and lower limits are specified to serve as constraints on the design variables. Thickness, lengths, weights or even coordinates are some example of DV's.
- State variables (SV's): quantities that constrain the design. They are also known as dependent variables, and are typically response quantities that are function of the design variables (i.e., stress, temperatures, heat flow rate, frequencies, deflections, mode shapes, etc).
- Objective Function: this is the scalar variable that one aims to minimize. It is a function of the design variables and therefore changing the value of the design variables its value also changes. The objective function is defined by the designer, and can integrate some variables such as natural frequencies, mode shapes, volumes, weight and so on.

The independent variables in an optimization analysis are the design variables. The vector of design variables is indicated in *Equation 4.14*.

$$x = [x_1, x_2, x_3, \dots, x_n] \quad with \quad i = 1,2,3, \dots, n$$

Equation 4.14: Vector that contains design variables

Design variables are subject to *n* constraints with upper and lower limits, that is:

$$\underline{x_i} \leq x_i \leq \overline{x_i} \quad with \quad i = 1,2,3, \dots, n$$

Equation 4.15: Upper and lower limits for the design variables

where *n* corresponds to the number of DV's.

The purpose of the design optimization is to minimize the Objective function *f*,

$$f = f(x)$$

Equation 4.16: Objective function to minimize

subject to:

$$g_i(x) \leq \overline{g_i} \qquad with \quad i = 1,2,3,\dots,n_1$$

$$\underline{h_i} \leq h_i(x) \qquad with \quad i = 1,2,3,\dots,n_2$$

$$\underline{w_i} \leq w_i(x) \leq \overline{w_i} \quad with \quad i = 1,2,3,\dots,n_3$$

Equation 4.17: SV's restraints

where g_i, h_i and w_i are state variables containing in function of the design variables (the underbars and overbars represent the lower and upper limits of the state variables respectively), and the $(n_1 + n_2 + n_3)$ is the number of SV's restraints with various upper and lower limit values.

Equations 4.16 and *4.17* represent a constrained minimization problem whose aim is to minimize the objective function *f* under the constraints imposed by *Equations 4.15* and *4.17*.

The goal of design optimization is to minimize the Objective function, while respecting the constraints imposed to the problem.

4.3.2 SQP Implementation

The SQP implementation consists of three main stages:

- Updating of the Hessian matrix of the Lagrangian function;
- Quadratic programming problem solution;
- Line search and merit function calculation.

This section shows only the first step of the SQP implementation, i.e. updating of the Hessian matrix of the Lagrangian function. At each major iteration *k* a positive definite quasi-Newton approximation of the Hessian of the Lagrangian function, *H*, is calculated using the BFGS method.

Broyden-Fletcher-Goldfarb-Shanno algorithm is an iterative method for solving unconstrained nonlinear optimization process. The BFGS method approximates Newton's method, a class of hill-climbing optimization techniques that seeks a stationary point of a function,

$$H_{k+1} = H_k + \frac{q_k q_k^T}{q_k^T s_k} - \frac{H_k^T H_k}{s_k^T H_k s_k}$$

Equation 4.18: Updating the Hessian Matrix

where:

$$s_k = x_{k+1} - x_k$$

Equation 4.19: Evaluation of the difference of the design variables between two subsequent iterates

$$q_k = \nabla f(x_{k+1}) - \nabla f(x_k) + \sum_{i=1}^{n} \lambda_i \cdot \nabla g_i(x_{k+1}) - \sum_{i=1}^{n} \lambda_i \cdot \nabla g_i(x_k)$$

Equation 4.20: Evaluation of the q parameter for each iteration

in which λ_i is an estimate of the Lagrange multipliers.

The other two steps of the SQP implementation are complicated and therefore for the scrupulous reader is advisable to read reference [39].

4.4 Scaling Methodology

Below are listed the steps required to perform an aeroelastic scaling and optimization model in order to design a scaled model that match the mass and stiffness distributions of the full model.

- The first step is to obtain information about the full scale model using a commercial finite element code. It is necessary to achieve static deformations, stress distributions by a static analysis and natural frequencies-mode shapes by a dynamic analysis. The software *MSC Nastran*™ can be employed;
- Make the aeroelastic analysis of the full scale model by *MSC Nastran*™ software;
- To construct a dynamic scaled model it is really important that a proper scaling is achieved. Therefore, it is required to choose wisely the scale factors and apply them to the results obtained from the FEM analysis of the full scale model. The new parameters achieved are the target values and the results obtained by a FEM analysis of the scaled model should converge to them;
- Design the scaled model and make the static-dynamic analysis by *MSC Nastran*™ software;
- Compare the results obtained with the target values;
- Optimization process through a *Matlab*™ code in order to reduce the discrepancies between target parameters and computational parameters;
- Aeroelastic analysis for the scaled model;
- Compare the aeroelastic results obtained by the full and scaled model.

Figure 4.4 presents a simple flowchart showing how the various computational tools are organized in order to develop the scaled model.

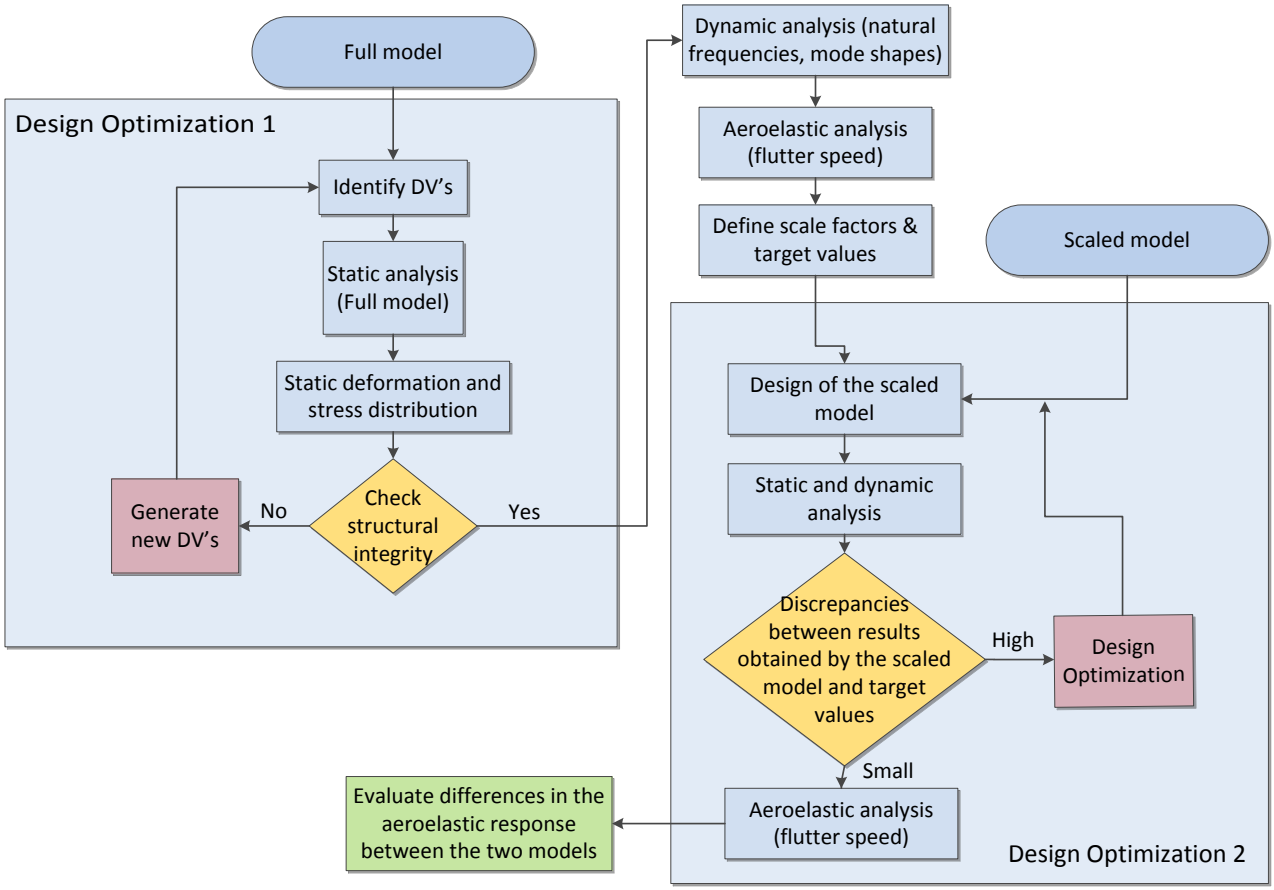

Figure 4.4: Scaling Methodology

Chapter 5

FULL WING MODEL

5.1 Introduction

In this chapter a complete three-dimensional wing was analyzed. The software used is *MSC Nastran*™. In order to help capturing the structural wing behavior a more complex structural model was applied rather than a simplified equivalent beam model. The wing is based on the NOVEMOR project of the EU 7th framework reference wing, which was altered to exhibit a higher aspect ratio. The geometric characteristics of this reference wing are listed in *Table 5.1*.

Data	
b_r [m]	31.46
b_{1r} [m]	6.18
b_{2r} [m]	9.55
S_r [m^2]	110
c_{r_r} [m]	7.57
c_{b_r} [m]	3.99
c_{t_r} [m]	1.72
M.A.C.$_r$ [m]	4.0
Λ_{LEr} [°]	25
Γ_r [°]	4.5
W_{TOr} [kg]	58000
W_{engine_r} [kg]	2800

Table 5.1: Geometric characteristics of the reference wing

The new wing is designed with an aspect ratio equal to twelve ($AR = 12$) keeping the wing area, the sweep and dihedral angle, the maximum takeoff weight and the engine weight constant values. Note that the subscripts of *r* and *n* represent reference and new wing respectively.

$$AR = \frac{b^2}{S} \rightarrow b_n = \sqrt{AR \cdot S_r} = 36.33\ m$$

$$M.A.C. = \frac{S}{b} \rightarrow M.A.C._n = \frac{S_r}{b_n} = 3.02\ m$$

$$M.A.C._n = F \cdot M.A.C._r \rightarrow M.A.C._n = F \cdot \left[\frac{c_{r\_r} + c_{b\_r}}{2} \cdot \frac{b_{1r}}{b_r/_2} + \frac{c_{b\_r} + c_{t\_r}}{2} \cdot \frac{b_{2r}}{b_r/_2} \right] \rightarrow F = 0.755$$

Equation 5.1: New parameters of the wing

Knowing *F* which is a correction factor it is possible to evaluate the new root, break and tip chord respectively (see *Equation 5.2*). Finally *Equation 5.3* and *5.4* allow to evaluate the new values of b_{1n} and b_{2n}.

$$\begin{Bmatrix} c_{r\_n} \\ c_{b\_n} \\ c_{t\_n} \end{Bmatrix} = 0.755 \cdot \begin{Bmatrix} c_{r\_r} \\ c_{b\_r} \\ c_{t\_r} \end{Bmatrix} = \begin{Bmatrix} 5.71\ m \\ 3.01\ m \\ 1.30\ m \end{Bmatrix}$$

Equation 5.2: New root, break and tip chord respectively

$$b_{1n} = \frac{b_{1r}}{b_r/_2} \cdot b_n/_2 = 7.13\ m$$

Equation 5.3: New distance between the root to the break section

$$b_{2n} = b_n/_2 - b_{1n} = 11.03\ m$$

Equation 5.4: New distance between the break to the tip section

Table 5.2 summarizes the geometric characteristics of this new wing.

Data	
b_n [m]	36.33
b_{1n} [m]	7.13
b_{2n} [m]	11.03
c_{r_n} [m]	5.71
c_{b_n} [m]	3.01
c_{t_n} [m]	1.30
M.A.C.$_n$ [m]	3.02

Table 5.2: Geometric characteristics of the new wing

The structural finite element model, shown in *Figure 5.1*, is a half-span model of a high aspect ratio ($AR = 12$) swept back wing with underwing mounted engine. In order to obtain more accurate results, it was decided to model also the pylon which connects the engine with the wing structure and its size, it is the same for right and left wing parts. The same cruise point of the unmodified wing geometry defined in the NOVEMOR project was selected: a Mach number of 0.78; and an altitude of 38000 feet.

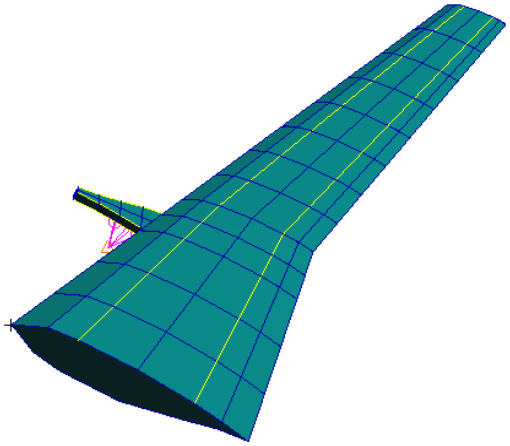

Figure 5.1: Structural model

The structural layout is designed to ensure structural integrity for a load limit of 3.8 g's. Linear and nonlinear static analyses are performed in order to design the internal configuration of the wing evaluating the differences between both analyses. Afterwards a modal analysis of the wing with and without fuel is performed in order to evaluate the differences in the dynamic behavior. Finally, this chapter ends with an aeroelastic analysis of the full model for different phases of flight, with and without fuel, for a load factor equal to one. The purpose is to calculate the flutter speed including geometric nonlinearities.

5.2 Static Analysis

As mentioned in the introduction (see Section 5.1), linear and nonlinear static analyses are performed to develop the internal configuration of the wing. The ultimate goal of the static analysis is to design a wing stiff enough to avoid aeroelastic problems, while at the same having the lighter structure possible. The design of the structure is based on a limit load factor, which according to Corke for regional jet can assume a value of 3.8 [14].

5.2.1 Structural Model

On the baseline model the wing contains an industrial standard two-spar configuration at 25% and 75% chord. In order to keep the internal configuration of the wing simple and to avoid further problems on the scaling of the full model, the pylon (eight ribs) and the wing (fourteen ribs) are modeled with equally spaced ribs. In the section where the engine is placed it was decided to add another rib with the purpose of increasing the wing stiffness. The spar/rib configuration is shown in *Figure 5.2*.

For the purpose of designing the wingbox, beam and shell elements are employed to model the wingbox caps and webs, respectively. Skins and ribs are modeled by shell elements.

For all the components of the structural model the material selected is the *7075 Aluminum* alloy. The yield stress for this alloy is 450 MPa [4]. Since the safety factor 1.5 is used, the allowable stress is reduced to 300 MPa.

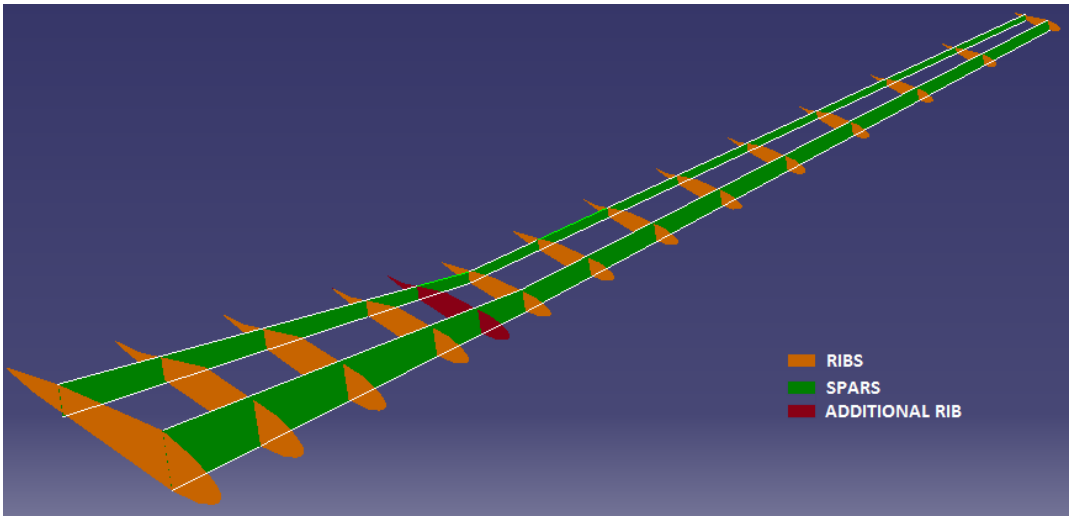

Figure 5.2: Internal configuration of the wing

The engine is modeled as a lumped mass placed in its center of gravity and it is linked with rigid links RBE2 to the ribs connecting the pylon to the engine. Rigid links RBE2 have been also used to ensure the connection between the pylon and the wing [16].

In accordance with the reference [23] the pylon is modeled by beam and shell elements in order to model the caps and webs, respectively. Skins and ribs are modeled by shell elements. *Figure 5.3* shows the final configuration of the pylon.

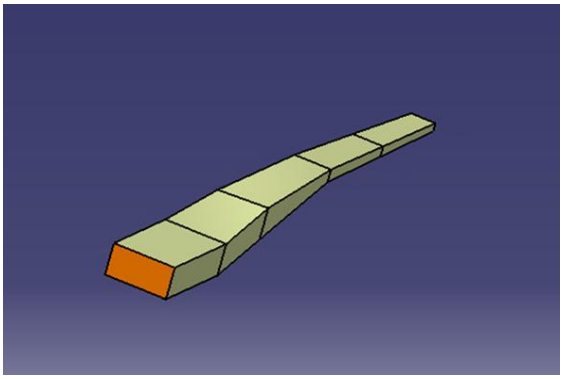

Figure 5.3: Pylon

Fuel is included in the calculations and it is modeled as lumped masses placed between wing sections and redistributed to surroundings nodes of the wingbox by MPC elements (see *Figure 5.4*) [32]. To calculate the amount of fuel storable in the tanks, the first step is to calculate their free volume and then this result must be multiplied for the density of a typical fuel for turboject, JET A-1 [57]. It was assumed that the fuel tanks have a length equal to 65% of the wing semi span and in this case the fuel storable in the wing is equal to 5600 kg.

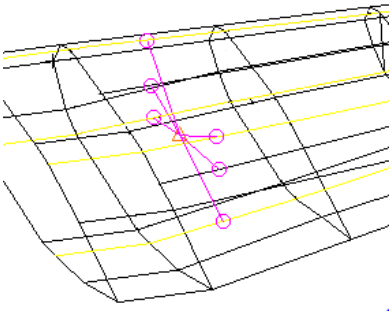

Figure 5.4: Fuel in each section modeled as lumped masses

The wing is clamped to the fuselage through the front and rear spar and it is analyzed under the aerodynamic pressure and gravity load. It was considered an elliptical distribution of lift.

The entire structural model is presented in *Figure 5.1*. It consists of 8952 nodes, 382 beam and 2084 shell elements respectively.

An optimization process is performed in order to develop the internal configuration of the wing. The following eight items are design variables:

- Size of the front wing spar;
- Size of the rear wing spar;
- Thickness of the wing ribs;
- Thickness of the wing skins;
- Size of the front pylon spar;
- Size of the rear pylon spar;
- Thickness of the pylon ribs;
- Thickness of the pylon skins;

The design variables are subject to the lower and upper limits. Lower limits are set at one millimeter in order to avoid manufacturing problems and high costs.

It was considered a classical spar configuration with an I-shaped cross section. The maximum spar cap width and height is fixed equal to $0.13 \cdot c$ and $0.01 \cdot c$ respectively where c is the local chord while the maximum spar web thickness is fixed equal to eight millimeters. The maximum allowable thickness of the rib and skin is set to one centimeter and five millimeters respectively.

The problem is subjected to constraints of maximum stress in the structural components and it is optimized by adjusting the design variables to minimize an Objective function which in this case is the structural mass of the model. The optimization process is executed in *Matlab*™ using *Matlab*™*'s fmincon function*, a Sequential Quadratic Programming (SQP) algorithm was employed. *Figure 5.5* shows the methodology used in order to develop the internal structure of the wing.

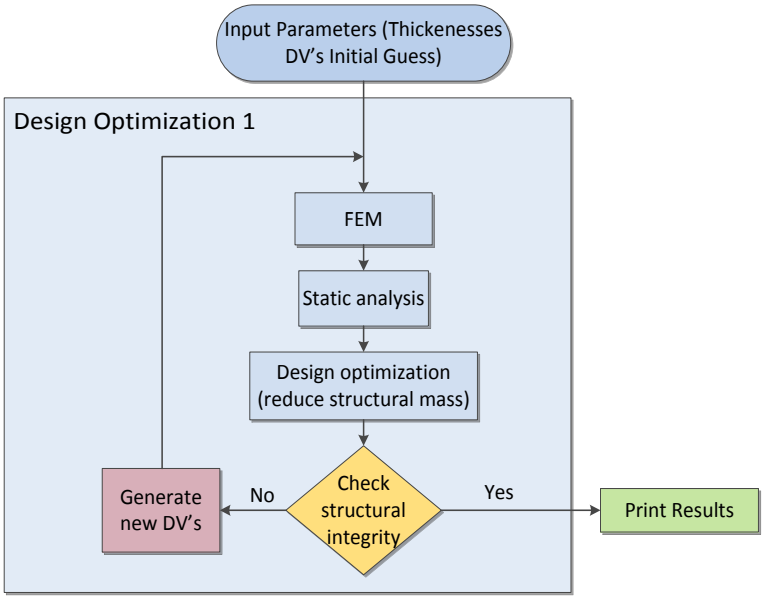

Figure 5.5: Methodology for static analysis

5.2.2 Linear and Nonlinear Static Analysis

Linear and nonlinear static analyses were performed in condition of full and empty tanks. For all cases examined, the maximum deflection is at the wing tip. The tip deflection obtained via linear static analysis in condition of empty tanks for a load factor equal to 3.8g, is 3.87 meter (see *Figure 5.6*). This is a relatively high deflection as it was expected. The maximum stress occurs near the wing root. Away from the wing root, the stresses decrease rapidly (see *Figure 5.7*). The front spar is more subjected to higher stress values than the rear spar and it is mainly due to the engine placement. In summary the optimization process to ensure structural integrity provides the following results:

- the front wing spar is thicker than the rear spar;
- the size of the spar is maximum at the root wing section. In this section the cap width and height for the front spar is equal to 0.26 meters and 42 millimeters, respectively. In addition the thickness of the web is equal to 4.3 millimeters;
- the thickness of the wing ribs varies from 5.5 to 1 millimeter along the wingspan;
- the additional rib has a thickness equal to 6.3 millimeters;
- the thickness of the skins from the root to the break station is 2.3 millimeters, 1.4 millimeters in the rest of the wing;
- no significant difference between the size of the front and rear pylon spar was found. However the size of the pylon spars in the joint section between the wing and the pylon is less than the size of the wing spars in the root section.
- the thickness of the pylon ribs varies from 3.5 millimeters (joint section) to 1.7 millimeters (tip section).

Theoretically the last three wing ribs can have a thickness less than 1 millimeter but this value was selected in order to avoid manufacturing problems.

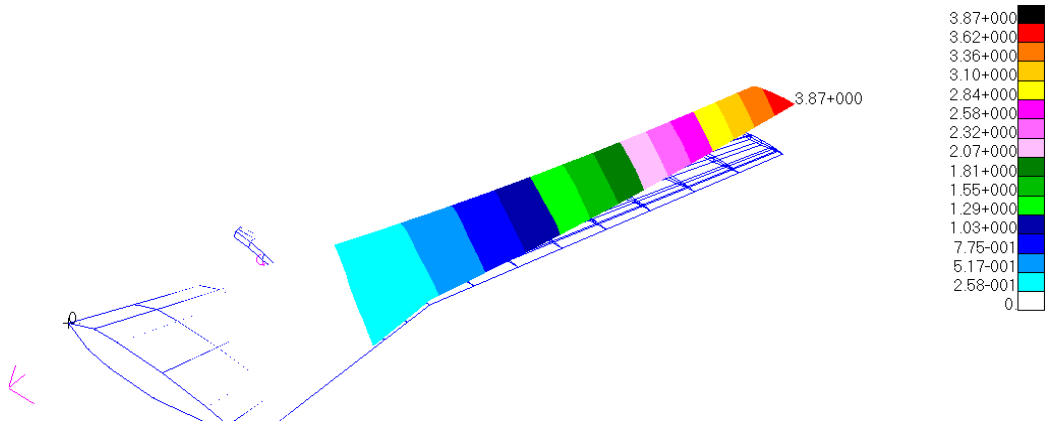

Figure 5.6: Tip deflection in meter obtained by linear static analysis in condition of empty tanks (n_z=3.8)

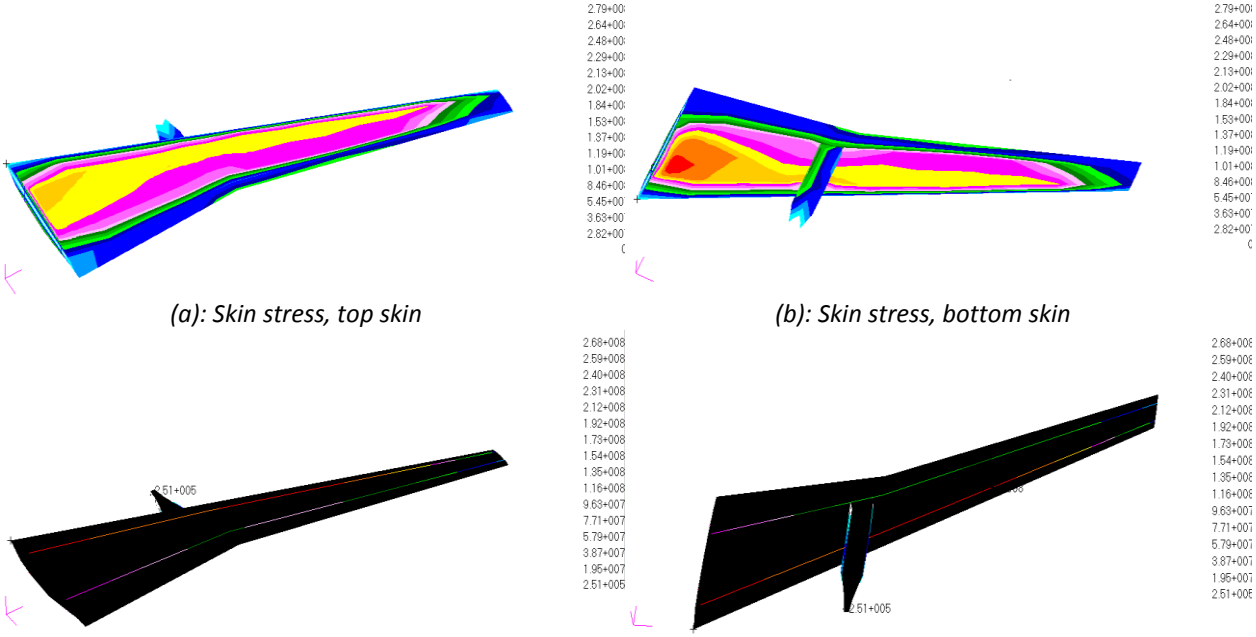

(a): Skin stress, top skin

(b): Skin stress, bottom skin

(c): Axial stress, top view

(d): Axial stress, bottom view

Figure 5.7: Stresses in Pascal obtained by linear static analysis in condition of empty tanks (n_z=3.8)

Table 5.3 summarizes the most important results for full fuel and empty tanks conditions ($n_z = 3.8$) respectively when linear and nonlinear static analyses are performed for the same structural model.

	Linear Analysis		Nonlinear Analysis	
Parameters	**No fuel**	**Full Fuel**	**No fuel**	**Full fuel**
Maximum skin stress [MPa]	279	296	196	201
Maximum caps stress [MPa]	268	286	275	294
Maximum ribs stress [MPa]	241	246	215	220
Tip deflection [m]	3.87	4.12	1.62	1.74

Table 5.3: Results for linear and nonlinear static analysis for both configurations (n_z=3.8)

The structure with full fuel tanks has a higher tip deflection and consequently exhibits the highest stress. This is due to the fact that it is required more lift to sustain a higher overall weight, as consequence the wing loading is higher as well and since no fuel is placed after 65% of wing span, the wing near the tip bends more for the full tanks configuration.

Important differences between linear and nonlinear results are observed (see *Table 5.3*). *Figure 5.8* shows the differences in terms of tip deflection when linear and nonlinear static analyses are performed for different values of load factor. The results diverge gradually increasing the load factor. At 4g, tip deflection is about 2.4 times lower from the one predicted by linear analysis. For a load factor equal to one the difference between the two analyses is around 16%.

Figure 5.9a and *5.9b* shows the variation of the bending and twist angle respectively belong the wing span for a load factor equal to one when linear and nonlinear static analyses are performed. The results confirm that the structure experiences a stiffness hardening effect when a nonlinear static analysis is performed.

In both the figures one can note a discontinuity in proximity to the break station ($y = 0.43 \cdot {}^{b}/_{2}$) that is due to a change in stiffness of the wing. From the root to the break station the wing is stiffer and this is mainly due for the placement of the engine.

Structural geometric nonlinearities can be attributed to nontrivial state deformation and/or large motion. The infinitesimal deformation condition is disobeyed, while the material is thought to be not beyond the elastic limitation for the little strain. The basis of the nonlinearity lies in kinematics, particularly the relations expressing generalized velocity and strain measures in terms of displacement and rotation variables of the wing.

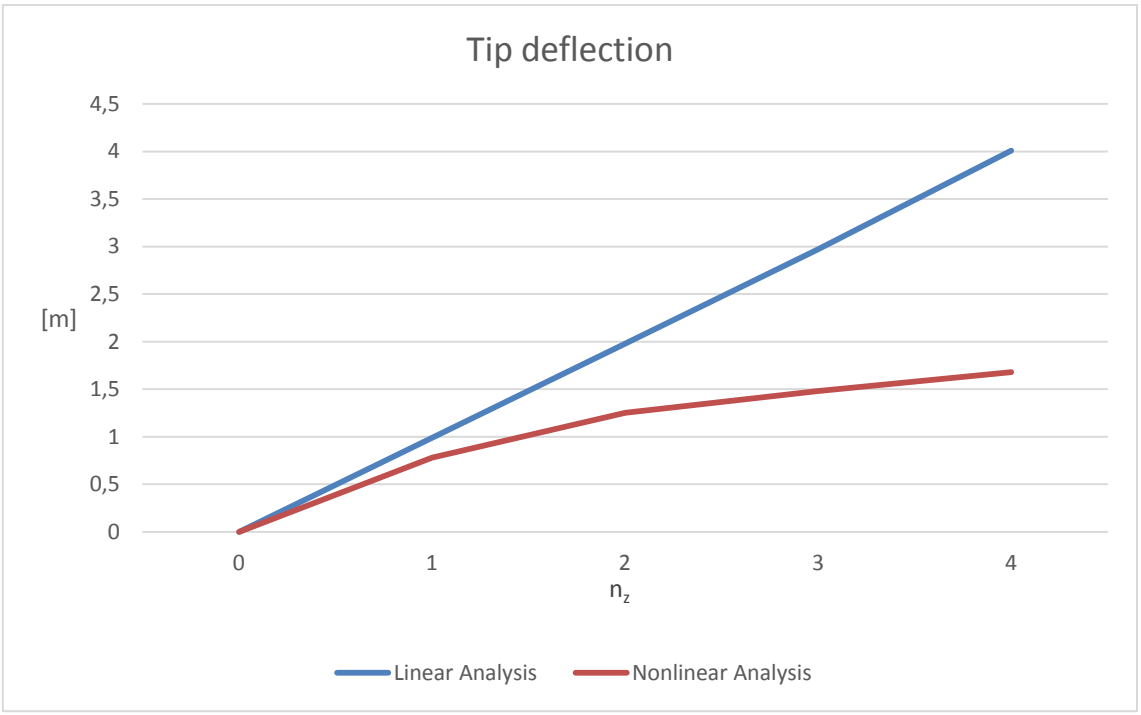

Figure 5.8: Different tip deflection when linear and nonlinear static analysis is performed in condition of empty tanks

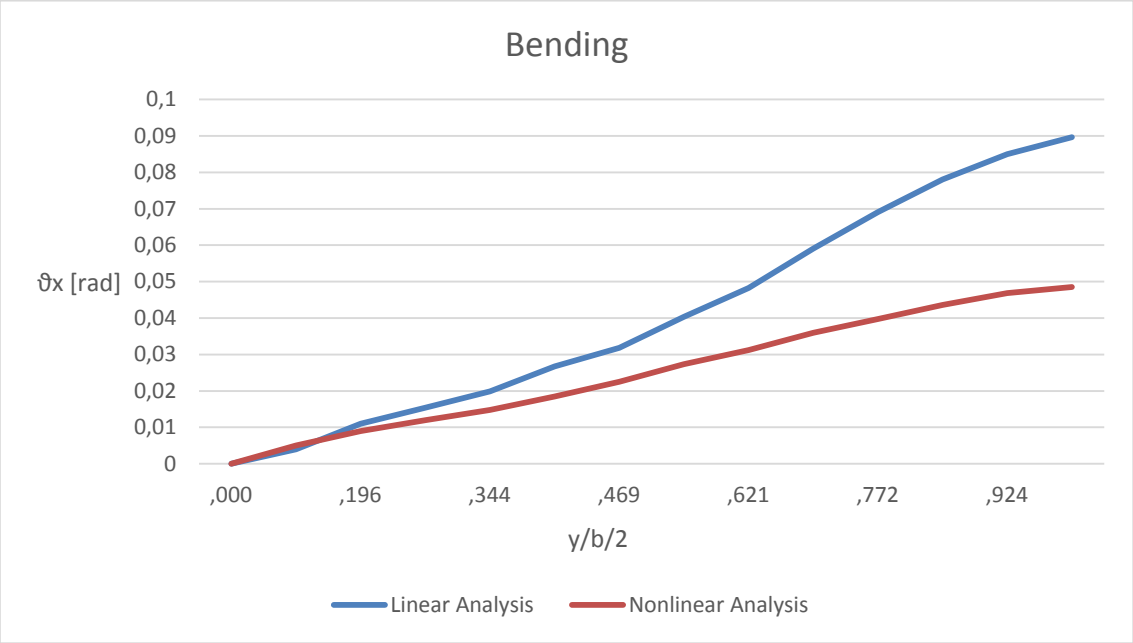

Figure 5.9a: Variation of the bending angle along the wing span (n_z=1) in condition of empty tanks

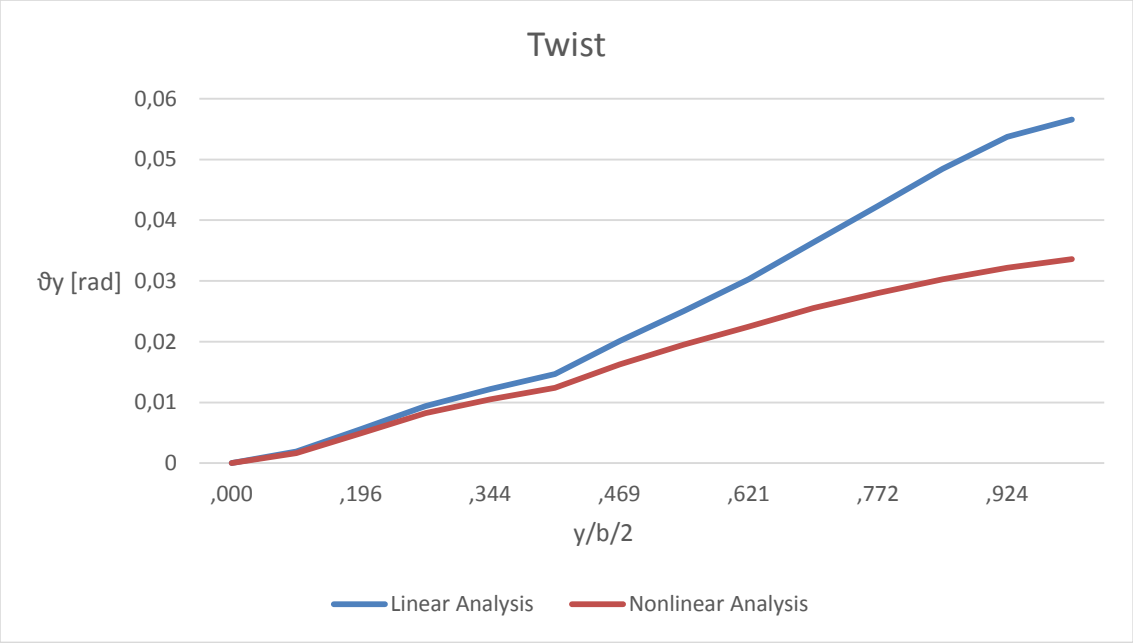

Figure 5.9b: Variation of the twist angle along the wing span (n_z=1) in condition of empty tanks

The final wing structural mass is 2438 kilograms. The entire structural model is modeled with 7075 Aluminum alloy, although by using lighter materials a weight reduction is expected to be achieved. Nowadays, two of the largest airplane manufactures, Airbus and Boeing are building new commercial models made of more than 50 percent carbon-fiber composite parts. The greatest benefit of composite materials is that they can be both lightweight and strong. The heavier an aircraft is, the more fuel it burns, so reducing weight is an important goal for aeronautical engineers. The aluminum alloy was used in this dissertation because the main purpose is an

aeroelastic scaling of the full model wing and not to investigate the benefits of composite materials in aeronautics.

5.3 Modal Analysis

In this section a linear modal analysis and pre-stressed normal modes of the wing with and without fuel are performed with *MSC Nastran*™ SOL 103 and SOL 106 respectively with the purposes of evaluating the differences in the wing dynamic behavior. The Lanczos algorithm is used for both analyses to obtain the natural frequencies and mode shapes.

Nastran™ solution SOL 103 uses reduced form of the equation of motion where no damping and no applied loading are considered,

$$[M]\{\ddot{u}\} + [K]\{u\} = 0$$

Equation 5.5: Reduced form of the equation of motion

where:

$[M]$	Mass matrix
$[K]$	Stiffness matrix
$\{u\}$	It assumes an harmonic solution $\{u\} = \{\Phi\}\sin(w \cdot t)$
$\{\Phi\}$	Eigenvector or mode shape
w	Circular natural frequency

Solutions of reduced form of the equation of motion are:

$$([K] - w_i^2[M])\{\Phi_i\} = 0 \quad i = 1,2,3 \ldots$$

Equation 5.6: Solutions of reduced form of the equation of motion

The results of *Equation 5.6* are eigenvalues and eigenvector which define mode shape of the structure and are in relation with natural frequency for certain mode:

$$f_i = \frac{w_i}{2\pi} \quad i = 1,2,3 \ldots$$

Equation 5.7: Natural frequencies

where f_i are the natural frequencies.

The first ten solutions are extracted. *Table 5.4* summarizes the results obtained while *Figure 5.10* shows some mode shapes of the wing for the configuration of empty tanks.

In *Table 5.4*, one can note that the natural frequencies associated to the wing with full fuel are lower than the respective natural frequencies of the wing without fuel. These results are expected due the extra mass added by the fuel. Regarding the mode shapes both wing models with and without fuel are similar.

		Natural frequencies [Hz]			
		SOL 103		SOL 106	
Mode	**Title**	**FULL FUEL**	**NO FUEL**	**FULL FUEL**	**NO FUEL**
1	Wing 1st flatwise bending	2.29	2.74	2.42	3.04
2	Engine pitching translation plus wing flatwise bending	3.46	3.62	3.57	3.68
3	Engine horizontal translation plus wing flatwise bending	4.70	5.06	4.53	4.68
4	Wing 2nd flatwise bending	5.46	6.36	6.03	7.06
5	Wing 3rd flatwise bending	9.21	10.35	9.51	11.56
6	Wing 1st edgewise bending	12.39	13.86	13.15	14.05
7	Wing 1st torsion	16.03	16.90	17.93	17.99
8	Wing 4th flatwise bending	19.40	20.41	20.70	20.62
9	Wing 2nd torsion	26.14	27.15	27.31	28.35
10	Wing 2nd edgewise bending	32.97	34.44	29.65	33.95

Table 5.4: Natural frequencies for both analyses

The initial modes are primarily bending modes while significant torsion and out-of-plane motion can be observed in the higher modes.

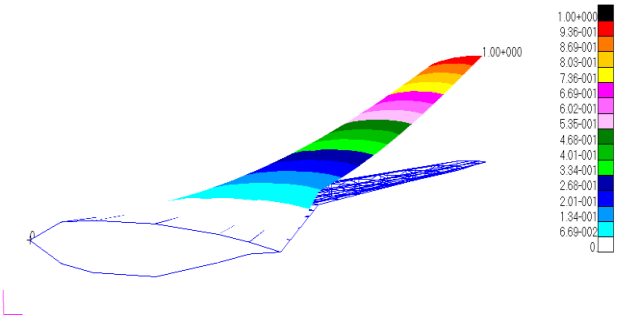

(a): First mode shape

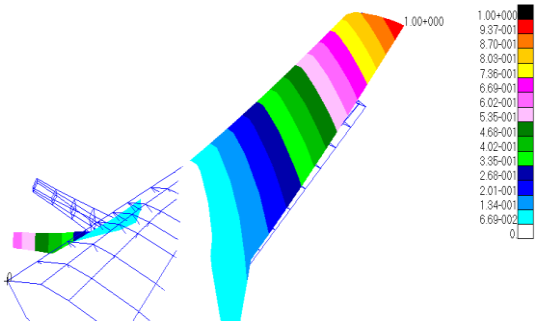

(b): Second mode shape

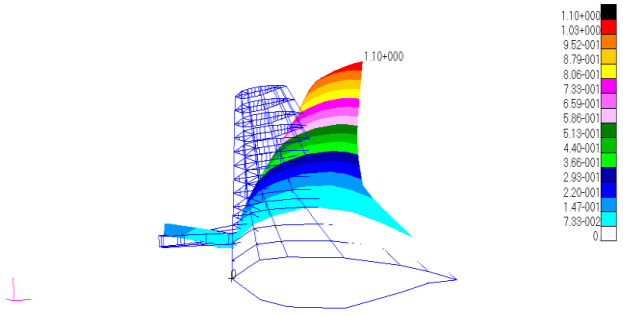

(c): Sixth mode shape

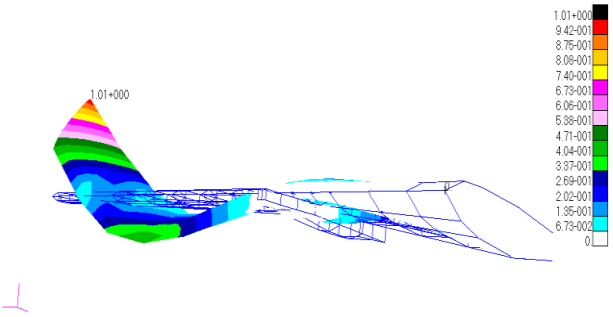

(d): Seventh mode shape

Figure 5.10: First, Second, Sixth and Seventh mode shape in condition of empty tanks predicted by Nastran™

Pre-stressed modal analysis uses the stress results of the nonlinear static analysis (SOL 106) as the initial condition for the dynamic analysis. As suggested by Harmin and Cooper *et al.* [13] the pre-stressed modal analysis was performed considering the wing in its deformed state for a load factor equal to one.

As one can see from *Table 5.4* most of the structural mode frequencies at the nonlinear equilibrium state are higher than the linear ones, except for the 3rd and 10th mode. This is because the structure experiences a stiffness hardening effect when a nonlinear analysis is performed.

With the results obtained for this work, it is interesting to compare these with other wing with similar configuration. The linear natural frequencies obtained by Cecrdle and Vich *et al.* [10] for an airline wing with underwing mounted engine confirm the results obtained in this work. Especially, not only the natural frequencies but also the mode shapes of the structural model are very similar.

5.4 Aeroelastic Analysis

In this section the aeroelastic characteristics of the high aspect ratio wings are described for different phases of flight, with and without fuel, for a load factor equal to one. To perform the analyses, *MSC Nastran*™ software was used.

In classic aeroelastic theory, linear assumptions are made for the aerodynamics and the structures. However, when the airspeed increases to high subsonic or transonic speeds, linear assumptions usually leads to results with insufficient accuracy [15]. Nonlinear aerodynamic effects are more difficult to analyze because the fluid motion is governed by equations where analytical solutions are practically non-existent.

In accordance with reference [13], *Figure 5.11* shows the steps required to perform a flutter analysis for high aspect ratio wings.

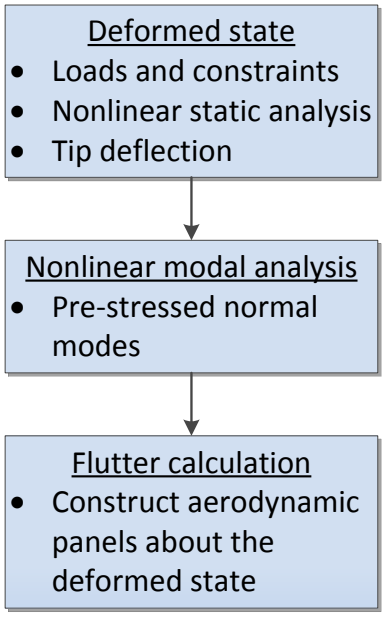

Figure 5.11: Methodology for a flutter analysis on a high aspect ratio wing

The first step is to perform a nonlinear static analysis in order to evaluate the displacement field of the structural model. It is necessary to compute the natural frequencies through pre-stressed normal mode on the deformed state because the reduced frequencies are inputs of a flutter analysis. In the last step for an aeroelastic analysis it is essential to construct the aerodynamic panels of the wing about its deformed state (see *Figure 5.12*).

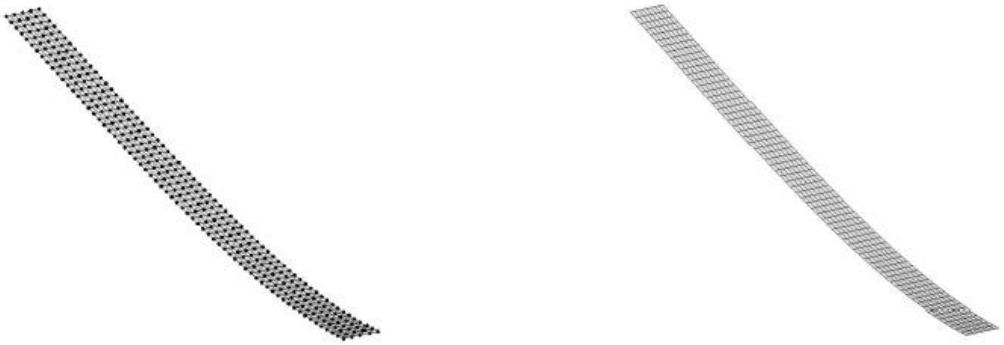

(a): Structural grid *(b): Aerodynamic grid*

Figure 5.12: Aerodynamic panels built on the deformed state [13].

5.4.1 Aeroelastic Model

In this section the aeroelastic model of the high aspect ratio wing is described. Based on the calculated mode shapes at the nonlinear static equilibrium state the Double Lattice Method (DLM) is applied in this work since the subsonic flow. It is a panel method that represents lifting surfaces by flat panels that are normally parallel to the flow and its theoretical basis is the linearized aerodynamic potential theory.

To better fit the aerodynamic model with the structural model, the wing is divided into two panels: the inboard wing (Wing1) is from the wing root to the break station while the outboard wing (Wing 2) is from the break station to the tip section, as shown in *Figure 5.13*.

Each panel is modeled with a CAERO1 element. The DLM is a finite element method, as such, needs suitable criteria to achieve sufficient accuracy. The number of finite elements (boxes) depends on aspect ratio and reduced frequencies, among other parameters.

Convergence and additional studies are contained respectively in reference [54] and [55].

The box chord requirement can be stated as:

$$\Delta x \leq 0.02 \cdot {}^{V}/_{f}$$

Equation 5.8: Box chord requirement

where *V* is the freestream speed of interest and *f* is the maximum frequency of interest in *Hz*.

The number of chordwise boxes becomes:

$$NC = {\bar{c}}/{\Delta x}$$

Equation 5.9: Number of chordwise

where $\bar{c}$ is the reference chord.

In order to obtain good results in subsonic flow, the aspect ratio of the boxes should be:

$$1 < AR_{boxes} < 3$$

The box span requirement becomes:

$$\Delta y = AR_{boxes} \cdot \Delta x$$

Equation 5.10: Box span requirement

Finally the number of spanwise divisions can be found as shown in *Equation 5.11*.

$$NS = {b}/{2}\Big/{\Delta y}$$

Equation 5.11: Number of spanwise divisions

Considering that in conditions of empty tanks the maximum frequency of interest is around 34 Hz and choosing the aspect ratio of the boxes equal to two, the entire aerodynamic panel of the wing contains 2924 boxes.

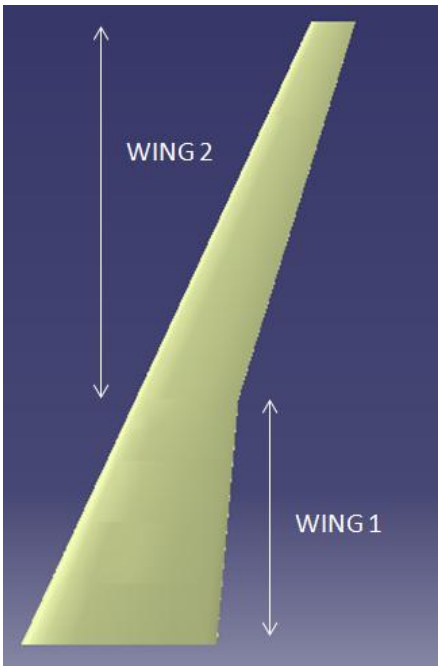

Figure 5.13: Components of the high aspect ratio wing

Two beam splines are created by connecting the aerodynamic panels of the wing to the structural model using the input command SPLINE2. The spline function transforms the aerodynamic loads into the structural model and structural deformations into the aerodynamic model. In *Figure 5.14* one can note that five structural points for each rib section (leading edge, front spar, 0.5·*c*, rear spar, trailing edge) are used to avoid ill-conditioned spline matrix which occurs when two grid points on the spline plane are too close to one other. Also for this reason it is recommended to choose either the upper or lower grid points, but not both [43].

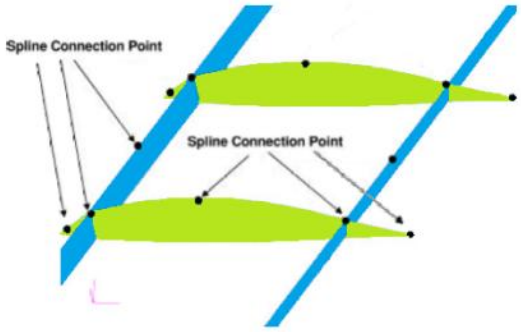

Figure 5.14: Spline connection points

The engine is modeled as a body-like component using the element CAERO2 and its dimensions can be inserted whit a PAERO2 entry [44].

During an aeroelastic analysis in *MSC Nastran*™ many correction factors can be entered manually (after tests in wind tunnel, CFD analysis), although, due to the lack of data, only the effects of the wing incidence and the dihedral effect through DMI entries are taken into account [44].

5.4.2 Static Aeroelastic Analysis

Static aeroelastic problems deal with the interaction of aerodynamic and structural forces on a flexible vehicle. This interaction causes a redistribution of the aerodynamic loading as a function of airspeed, which is of concern to both the structural and aerodynamic analyses. Such redistribution can cause internal structural load and stress redistributions, as well as modify the stability and control derivatives [56].

MSC Nastran™ software computes the aircraft TRIM conditions, resulting in the recovery of structural responses, aeroelastic stability derivatives, and static aeroelasticity divergence dynamic pressure.

In this study a rigid stability derivative analysis is performed to examine the aeroelastic results. This type of analysis provides both splined and unsplined rigid stability derivatives, which can be compared to provide an assessment of the spline quality. If the numbers differ significantly, it may indicates that the aerodynamic forces may not have been transferred consistently to the structure.

Table 5.5 shows an example of splined and unsplined lift coefficient derivatives with angle of attack equal to 0.5° and nominal design condition ($M = 0.78$, $z = 38000$ feet).

Aerodynamic derivatives $\left[{}^{1}/_{rad}\right]$	Splined	Unsplined
$C_{L\alpha}$	5.0284	4.9415
$C_{M\alpha}$	-2.0480	-1.9844
C_{Lq}	28.448	27.482
C_{Mq}	-46.871	-45.699

Table 5.5: Splined ad unsplined lift coefficient derivatives

From *Table 5.5* one can note a good matching between the unsplined and splined column, indicating the spline is satisfactory.

5.4.3 Flutter Analysis

In this section the wing flutter analysis was performed for both configurations, with and without fuel, for a load factor equal to one.

Regulations **FARs - Part25 - Section 629** require that the aircraft must be free from aeroelastic problems for speeds higher than 1.2 V_D where V_D is the dive speed [18].

In nominal design condition, the dive speed is 343 m/s, so the minimum flutter speed in this work is limited to a maximum speed of 411.6 m/s (see *Equation 5.12*).

$$V_{max} = 1.2 \cdot V_D = 411.6\ {}^{m}/_{s}$$

Equation 5.12: Minimum flutter speed

Nastran™ solution SOL 145 is used and the problem is studied with the British PK-Method. The analysis includes 10 modes. The structural damping is included via common value of damping ratio of 1% [10]. Input for flutter solutions are dynamic characteristics which are represented by reduced frequencies and flight conditions (density, velocity).

Results for design condition ($M = 0.78,\ z = 38000$ feet) with full and empty tanks are shown respectively in *Figure 5.15* and *5.16*

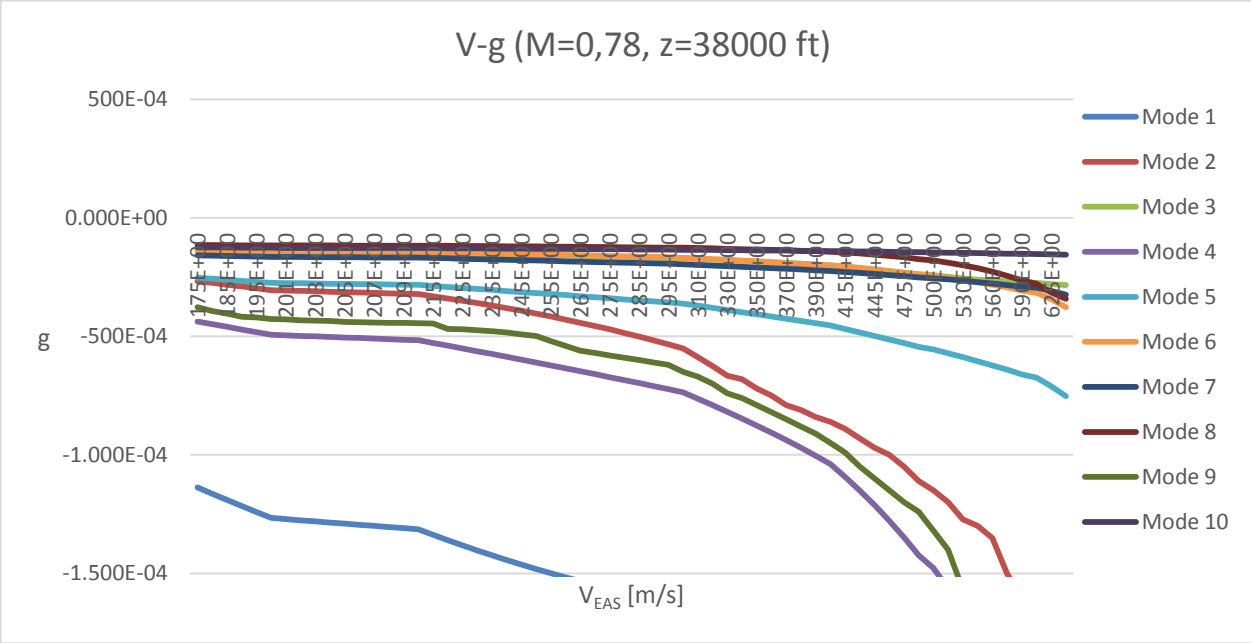

(a): V-g diagram

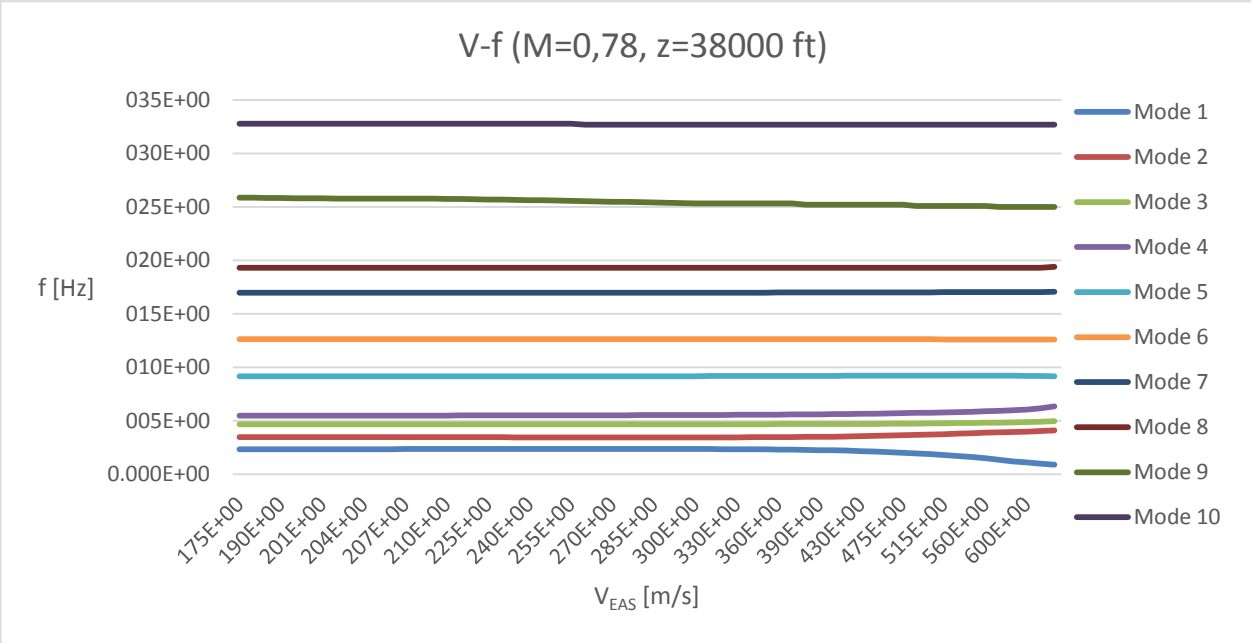

(b): V-f diagram

Figure 5.15: V-g and V-f diagram in design condition for full fuel tanks

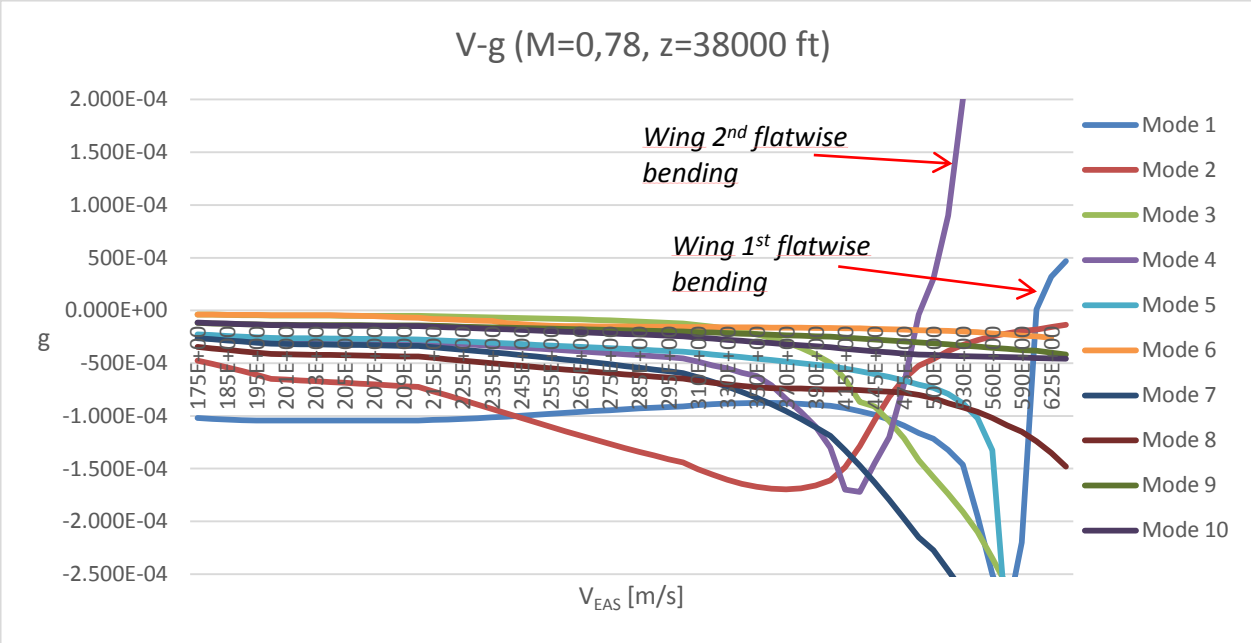

(a): V-g diagram

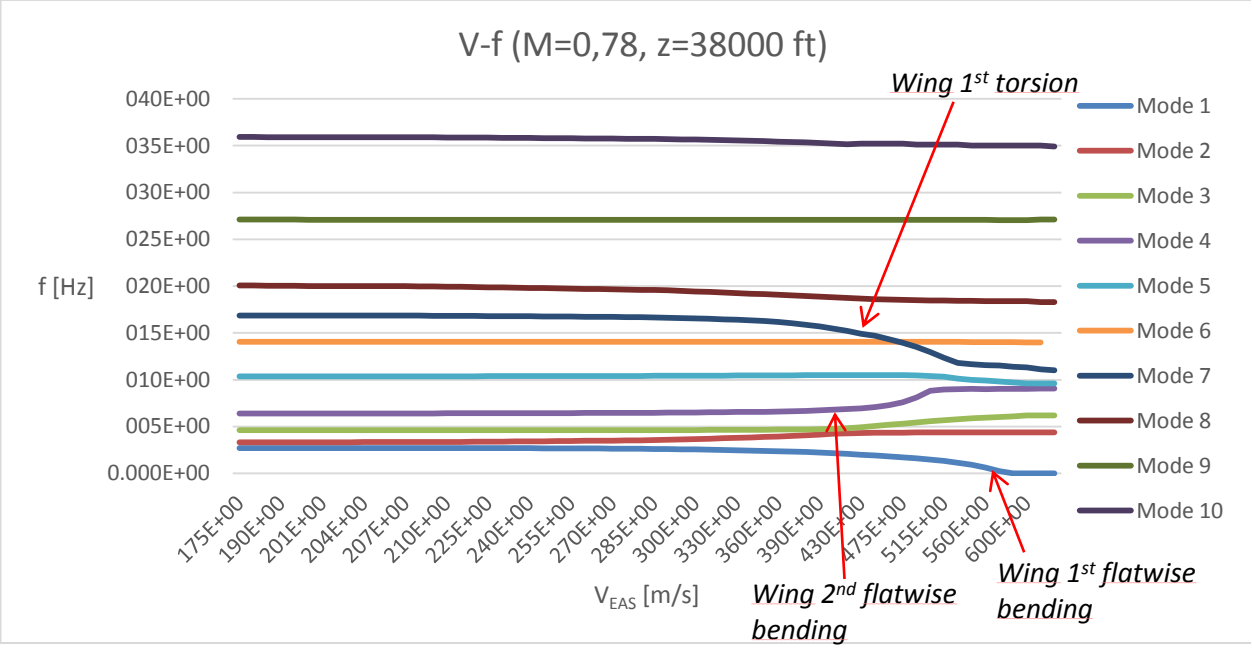

(b): V-f diagram

Figure 5.16: V-g and V-f diagram in design condition for empty tanks

Negative aeroelastic damping is an indication of aeroelastic stability.

From *Figure 5.15* one can note that no mode of flutter occurs in design condition with full fuel tanks.

Figure 5.16 shows that in condition of empty tanks the flutter speed is $V_{FL} = 496\ ^{m}/_{s}$ with a corresponding flutter frequency equal to $f_{FL} = 7.54\ Hz$. The primary flutter mode is the fourth, the critical combination of the modes is: fourth (Wing 2nd flatwise bending) and seventh (Wing 1st torsion).

Moreover the flutter speed is higher than the V_{max} (see *Equation 5.12*). It is possible also to note that the divergence speed occurs for a velocity equal to $V_{DIV} = 581\ ^{m}/_{S}$. This result confirms that for swept back wings the main aeroelastic problem is flutter and not divergence as discussed in reference [7].

A flutter analysis with the non-deformed wing was performed in order to evaluate the differences in terms of flutter speed. *Table 5.6* summarizes the results for the nonlinear deformed and non-deformed state respectively. One can observe that it is essential to investigate the flutter problem with the wing in its deformed state in order to avoid obtaining an over-estimation of the flutter speed. A wing with high stiffness has a small tip deflection and therefore the flutter speed is usually quite high, vice versa if the deformed state increases the flutter speed tends to decrease.

Flutter Speed	Full fuel tanks		Empty tanks	
	Nonlinear deformed wing	Non deformed wing	Nonlinear deformed wing	Non deformed wing
$V_{FL}[^{m}/_{S}]$	*ND*	*ND*	496	514

Table 5.6: Flutter speed for the non deformed and deformed condition respectively

In *Table 5.6 ND* signifies that no flutter speed had occurred.

For a greater overview of the flutter problem two different analyses were performed. In the first analysis the altitude is a fixed parameter equal to the design altitude ($z = 38000$ feet), while the Mach number can vary between 0.75 and 0.80. Vice versa in the second analysis where the Mach number is fixed at 0.78, while the altitude varies between 25000 and 50000 feet.

The results of the first analysis, both in terms of full fuel and empty tanks conditions are very similar to those shown in *Figure 5.15* and *5.16*. No flutter mode occurs for full fuel conditions. Instead for empty tanks the critical mode is the fourth and the flutter speed for different Mach numbers is summarized in *Table 5.7*. Increasing the Mach number the flutter speed tends to decrease but its value remains higher than the maximum allowed speed.

Mach	$V_{FL}[^{m}/_{S}]$	
	Full fuel tanks	Empty tanks
0.75	ND	580
0.76	ND	566
0.77	ND	531
0.78	ND	496
0.79	ND	475
0.80	ND	452

Table 5.7: Results obtained from the first analysis

The critical flutter speed is reached for a Mach number equal to 0.82. However, a regional jet hardly has a Mach cruise number higher than 0.80. In addition the Doublet Lattice Method (DLM) should be applied only for subsonic flow, so increasing the Mach number this theory provides results with less accuracy. In fact the DLM under-predicts the drag that increases highly in the transonic region, which can lead to different values of flutter speed; but differently the lift of the model is evaluated with good accuracy. For these reasons, it was decided that the Mach number can vary only between 0.75 and 0.80.

The second analysis shows that no critical altitude is present for the wing in full fuel tanks conditions but it suggests flying at an altitude greater than 27000 feet in condition of empty tanks. In this last case the flutter sped is $V_{FL} = 428\ {}^{m}/_{S}$ and this value is slightly lower than the minimum allowable flutter speed. The minimum allowable flutter speed is different from the value evaluated in *Equation 5.12* because when the altitude changes the speed of sound also changes, so the cruise speed changes and consequently the minimum allowable flutter speed (see *Equation 5.12*). The minimum flutter speed at 27000 feet is equal to $V_{max} = 430\ {}^{m}/_{S}$.

The critical mode is the fourth. The result in term of V-g diagram for empty tanks is shown in *Figure 5.17*.

Therefore, in order to avoid aeroelastic problems in cruise conditions two different solutions are possible: in the first case it is possible to fly at the design altitude ($z = 38000$ feet) with full fuel or empty tanks and with Mach number that varies from 0.75 and 0.80, while in the second case, when the Mach number is a fixed value of 0.78, it is necessary to fly at altitudes above 27000 feet in the event of empty tanks.

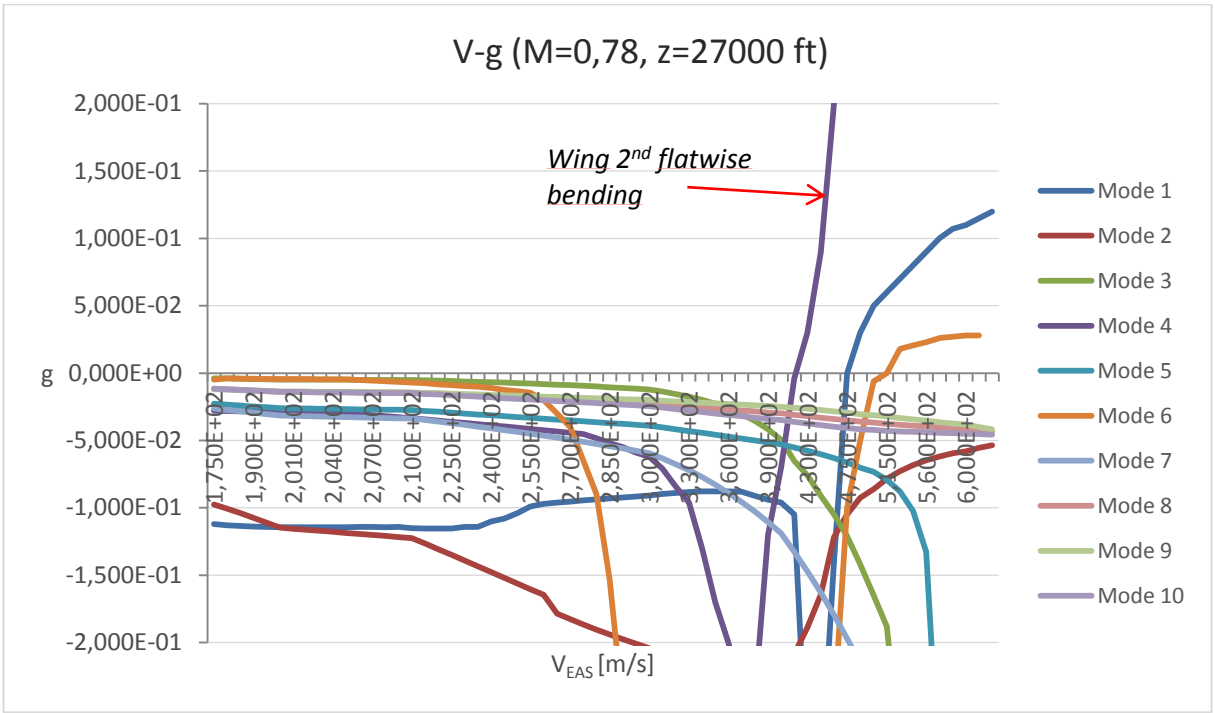

Figure 5.17: V-g diagram for empty tanks conditions

Chapter 6

SCALED MODEL

6.1 Introduction

The aeroelastic scaling laws allow some freedom in building a scaled model that aeroelastically represents the full scale model. Such freedom allows the model designer to choose materials and distribution of the materials to accommodate model manufacturing limitations.

The task of the model designer is to use this design freedom to produce a model for which the non-dimensional mass [M], stiffness [K] and aerodynamic influence [Q] matrices match those of the full scale model.

The design problem is solved using optimization techniques. The objective function to be minimized is the difference between the weight and natural frequencies/mode shapes of the scaled model and the corresponding variables of the full model. Scaling is necessary because the scaled model and the full model are different in size, and the atmospheric flight conditions are different from the scaled model conditions.

The results obtained in this chapter for the aeroelastic scaling do not take into account nonlinear effects and the scaled model matches the aeroelastic response for the full model with empty tanks.

6.2 Design Parameters of the Scaled Model

To build a dynamic scaled model it is of capital importance that a proper scaling is achieved. In this section, the target values for the scaled wing parameters will be presented. It is taken as a reference the wing full scale model with empty tanks and a load factor equal to one.

Length Ratio

The length ratio is established by the size of the full scale model compared to wind tunnel restrictions. It was considered that the wind tunnel has a cross section of 1.5 m X 1 m. The wing semi-span must be 1.2 meter long, in order to maintain uniform flow over the entire wing.

$$n_g = \frac{b_s}{b_f} = \frac{1.2\ m}{18.16\ m} = 0.066$$

Equation 6.1: Length scale

The grid points of the full scale model must be scaled down by a factor of 0.066 to define the grid points of the scaled model.

Air Density Ratio

To calculate the air density ratio (see *Table 6.1*) it is necessary to know the altitude in which the full model operates and the altitude where the scaled model is going to be tested in the wind tunnel. The full model operates at 38000 feet while the scaled model will be tested in sea level conditions

Input Parameters		Output Parameter
$\rho_s = 1.225\ {}^{kg}/_{m^3}$ $\rho_f = 0.333\ {}^{kg}/_{m^3}$	$n_\rho = \frac{\rho_s}{\rho_f}$	$n_\rho = 3.671$

Table 6.1: Air density scaling factor

Mass Ratio

To acquire the mass of the scaled model (see *Table 6.2*) it is used the mass-ratio scaling factor, for which it is needed to know the altitude of operation of both models and the length scale previously calculated.

Input Parameters		Output Parameter
$M_f = 2438\ Kg$ $n_g = 0.066$ $n_\rho = 3.671$	$n_M = \frac{M_s}{M_f} = n_g^3 \cdot n_\rho$	$n_M = 1.0554 \cdot 10^{-3}$ $M_s = 2.573\ kg$

Table 6.2: Target mass value

Velocity Ratio

One of the full scale conditions is the aircraft speed of 228.1 ${}^{m}/_{s}$ and knowing that velocity is a primary quantity, it can be chosen liberally. However it must be constrained by the requirement that both full scale and scaled aircrafts operate at the same trim state, i.e., the same C_L (see Section 3.3).

Input Parameters		Output Parameter
$V_f = 228.1\ {}^{m}/_{s}$ $n_g = 0.066$ $n_\rho = 3.671$ $n_M = 1.0554 \cdot 10^{-3}$	$n_v = \frac{V_s}{V_f} = \sqrt{\frac{n_M}{n_\rho \cdot n_g^2}}$	$n_v = 0.2569$ $V_s = 58.6\ {}^{m}/_{s}$

Table 6.3: Velocity of the scaled model

Frequency Ratio

Knowing the natural frequencies of the full model (SOL 103) and applying the frequency scale factor, one can determine the target natural frequencies of the scaled model (see *Table 6.4*). To use the frequency scaling factor it is needed the length and velocity scaling factors. Note that it is taken as a reference full scale model the wing with empty tanks.

Full Scale model			Scaled model
Mode	Natural frequency [Hz]	$n_f = \frac{f_s}{f_f} = \frac{n_v}{n_g}$	Natural frequency [Hz]
1	2.74		**10.66**
2	3.62		**14.09**
3	5.06		**19.69**
4	6.36		**24.75**
5	10.35		**40.28**
6	13.86		**53.95**
7	16.90		**65.78**
8	20.41		**79.44**
9	27.15		**105.68**
10	33.44		**130.16**

Table 6.4: Natural frequencies of the scaled model

Mode shapes

In the case of the free-vibration modes, it is only needed to match the shapes, not their values. With the objective shape and the associated target frequency, the desired modal response is attained. Therefore, for the mode shapes matching it is required a normalization of displacements and rotations. The following table (see *Table 6.5*) shows the first mode shape displacements and rotations for some points of the full model, the maximum positive displacement and rotation and the target values for the scaled model. The normalization is based on the division of the displacements and rotations of the full scale model by the maximum positive displacements and rotations respectively. The resulting values are the desired normalized mode shape to be attained in the scaling process.

Full Scale Model						Scaled Model			
Node	T_2 [m]	T_3 [m]	R_1 [rad]	R_2 [rad]	**Maximum Displacement 0.986 m** **Maximum Rotation 0.081 rad**	T_2 [-]	T_3 [-]	R_1 [-]	R_2 [-]
2613	-0.055	0.688	0.074	-0.030		-0.0557	0.6977	0.9135	0.3703
2615	-0.061	0.721	0.073	-0.038		-0.0618	0.7312	0.9012	0.4691
2713	-0.064	0.821	0.079	-0.042		-0.0649	0.8326	0.9753	0.5185
2715	-0.070	0.852	0.078	-0.042		-0.0709	0.8640	0.9629	0.5185
2813	-0.073	0.958	0.081	-0.043		-0.0739	0.9716	1	0.5308
2815	-0.079	0.986	0.081	-0.043		-0.0801	1	1	0.5308

Table 6.5: Full scale first mode shape displacements-rotations and respective target values for the scaled model

Force-ratio and Static deflection

It is required for Method 2 the application of some load to the structure in order to uncouple the mass and stiffness distribution (see *Figure 3.2*). For that it is needed the force-ratio, which requires the length scale, air density ratio and velocity ratio (see Section 3.3).

The total load to apply to the scaled model is evaluated in *Table 6.6*. The wing is clamped in the root section and it is analyzed under the aerodynamic pressure and gravity load. It was considered an elliptical distribution of lift.

Input Parameters		Output Parameter
$\boldsymbol{F_f = 189263\ N}$ $\boldsymbol{n_\rho = 3.671}$ $\boldsymbol{n_v = 0.2569}$ $\boldsymbol{n_g = 0.066}$	$\boldsymbol{n_F = \frac{F_s}{F_f} = n_\rho \cdot n_v^2 \cdot n_g^2}$	$n_F = 1.0553 \cdot 10^{-3}$ $\boldsymbol{F_s = 199.73\ N}$

Table 6.6: Design scaled load

The target linear static deflection (see *Table 6.7*) is obtained applying the length scale to the full static deflection. The rotations do not need to be scaled, since they are dimensionless parameters

Input Parameters		Output Parameter
$\boldsymbol{w_f = 0.96\ m}$ $\boldsymbol{n_g = 0.066}$	$\boldsymbol{\frac{w_s}{w_f} = n_g}$	$\boldsymbol{w_s = 0.063\ m}$

Table 6.7: Scaled static deflection

6.3 Build a Scaled Model

In order to properly represent the full model by the scaled model, it was decided to match the first seven natural frequencies and respective translational and rotational modes with a discrepancy of 5%. This choice is because the flutter phenomenon occurs as result of coupling of the second flatwise bending (fourth mode) and first torsional (seventh mode) natural modes of the wing (see Section 5.4.3). Also the overall mass should not exceed a 5% of error margin.

Due to material and manufacturing constraints, the scaled model cannot be manufactured with the same wing box structural layout. Bisplinghoff *et al.* [7] recommends a ladder structure, among other options, as an alternative configuration for aeroelastically scaled models. The rectangular spars and cylindrical rungs can be tailored to match the required stiffness. Modern foam materials allow the construction technique illustrated in *Figure 6.1*. Aerodynamic shape is maintained by *Polyethylene* foam. *Balsa* ribs and leading and trailing edge strips would provide local support, but overall the *Polyethylene* and *Balsa* would provide negligible global stiffness. Designable lead mass allow inertia matching.

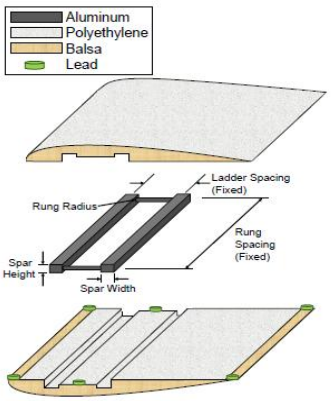

Figure 6.1: Scaled model wing section concept [50]

Beam elements are most appropriate to model the ladder structure. Nonstructural mass is modeled as lumped masses at the leading edge, center, and trailing edge of each rib section.

The following eleven items are design variables:

- width of front wing spars;
- height of front wing spars;
- width of rear wing spars;
- height of rear wing spars;
- diameter of wing rungs;
- width of front pylon spars;
- height of front pylon spars;
- width of rear pylon spars;
- height of front pylon spars;
- diameter of pylon rungs (*Configuration 1*) / thickness of pylon ribs (*Configuration 2*);
- lumped masses.

The problem is subject to maximum stress constraints in the structural components and it is optimized by adjusting the design variables to minimize an Objective function with the goal of matching the desired natural frequencies and mode shapes. The optimization process is executed in *Matlab*™, using *Matlab*™*'s fmincon function* and applying Sequential Quadratic Programming (SQP) algorithm.

6.3.1 Material Choice

The geometry of the scaled model is externally the exact scaled geometric of the full model. Moreover the scaled model has the same constraints of the full scale, all degrees of freedom of the points at root of the front and rear spars have no displacements and rotations.

Typically it is known the full scale model completely. All the structural components of the full model are modeled with the *7075 Aluminum* alloy (see Section 5.2.1). The question is to find the best material to model the

ladder structure of the scaled model. An exact scale of the *7075 Aluminum* alloy will lead to a none existing isotropic material.

In this sub-section three different materials are chosen for a comparison study (see *Table 6.8*), and from which the material that most suit is selected.

Material	Young Modulus [Pa]	Yield strength [Pa]	Poisson ratio [-]	Density [kg·m^{-3}]
7075 Aluminum alloy	7.20E+10	4.50E+08	0.32	2810
Elektron 43	4.40E+10	1.15E+08	0.29	1840
Stainless steel	1.95E+11	2.20E+08	0.30	8100

Table 6.8: Material properties

References [37] and [5] summarize the mechanical properties of the *Elektron 43* and *Stainless steel* respectively. *Elektron 43* is a lightweight magnesium alloy.

The Poisson ratio does not need any scaling factor but the other three properties need. For density there is the density ratio n_ρ previously calculated.

The other properties have units of pressure and it was not created any scaling factor for pressure. To obtain the pressure scale it is needed to apply the Buckingham π theorem to *P*, which has units of $M \cdot L^{-1} \cdot T^{-2}$, using the primary quantities ρ, *V* and *b*, the pressure-ratio scaling factor (see *Equation 6.2*) became:

$$\left(\frac{P}{\rho \cdot V^2}\right)_s = \left(\frac{P}{\rho \cdot V^2}\right)_f \rightarrow n_P = \frac{P_s}{P_f} = \frac{(\rho \cdot V^2)_s}{(\rho \cdot V^2)_f} = n_\rho \cdot n_v^2$$

Equation 6.2: Pressure scaling factor

The resulting properties after scaling the *7075 Aluminum* alloy are summarized in *Table 6.9*.

	Target Scaled Material
Young modulus [Pa]	1.17E+10
Yield strength [Pa]	1.09E+08
Poisson ratio [-]	0.32
Density [kg·m^{-3}]	10315

Table 6.9: Target scaled material

This scaled material has the same Poisson ratio of the *7075 Aluminum* alloy but has 3.67 times more density and sixteen times less Young modulus and Yield strength.

Using the materials from *Table 6.8* it was made an average error of the four properties with the target scaled material. From *Table 6.10* it is observable that *Elektron 43* has the lowest average error, so it is the selected material to model the ladder structure of the scaled model.

Material	Average error
7075 Aluminum alloy	275%
Elektron 43	162%
Stainless steel	474%

Table 6.10: Materials average error in relation to the target scaled material

6.3.2 Approaches Description

As discussed earlier, Bisplinghoff et al. [7] recommends a ladder structure, among other options, as an alternative configuration for aeroelastically scaled wing models. From the governing equations of linear elasticity, it can be proved that every model, which has the same scaled geometry and the same scaled mass and stiffness distributions, will result in the same modal response (mode shapes and frequencies) as those of the full model, after appropriate scaling independently of the internal configuration. Therefore in this study in order to prevent building ribs too close together eight equally spaced ribs for the wing were used (see *Figure 6.2a*). Four *Balsa* ribs are distributed from the root to the break station (rung spacing=0.15 meter) while the remaining four are present in the second part of the wing (rung spacing = 0.20 meter). The mechanical properties of *Balsa* are summarized in reference [28]. In *MSC Patran*™ software ribs are modeled by shell elements.

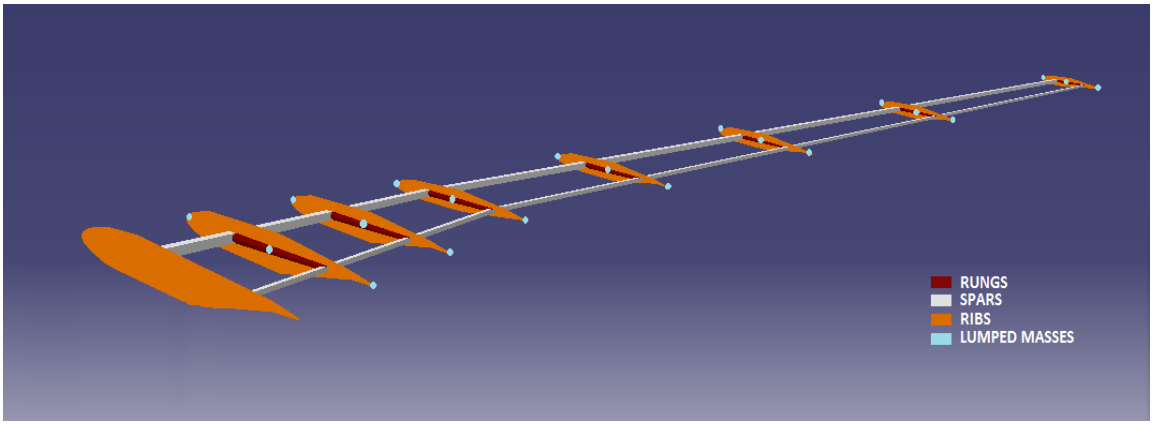

(a): Internal configuration of the wing scaled model

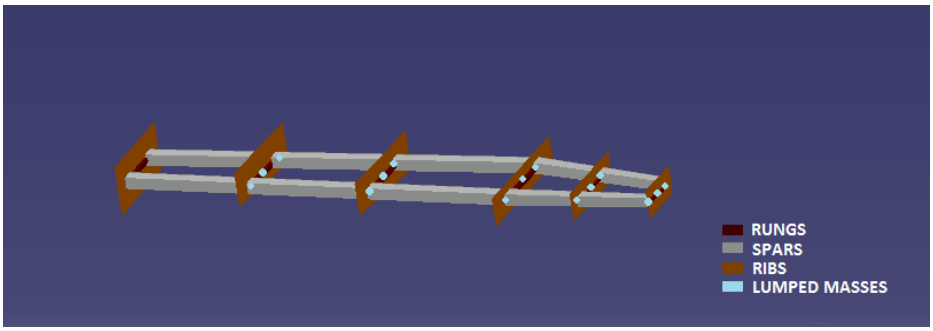

(b): Internal configuration of the pylon scaled model

Figure 6.2: Internal configuration of the scaled model

For simplicity, in *MSC Patran*™ software the *Polyethylene* was not modeled because it is a material with a very low density and its main goal is only to maintain the aerodynamic shape of the airfoil. To perform this task it was decided to model the wing skins with shell elements to simulate the behavior of a very thin layer (0.5

millimeters) of *Balsa* material. The ladder wing structure consists of a front and rear rectangular spar plus seven cylindrical rungs (see *Figure 6.2a*). The two spars are placed at 25% and 75% chord. The front and rear spars can be different in size while each rung has a constant diameter for each section, but their properties can change with the wingspan. In *MSC Patran*™ software this ladder structure is modeled by beam elements and the material selected is *Elektron 43* as previously described (see Section 6.3.1).

In this section the question is to decide how to model the pylon. Usually in the aeroelastic scaled model only the wing is scaled, but for this work it was decided to scale also the pylon. Two different *Configurations* have been developed.

In *Configuration 1* the pylon is modeled with another ladder structure. It consists of a front and rear rectangular spar plus six cylindrical rungs. The two spars are placed at 25% and 75% chord. The front and rear spars can be different in size while each rung has a constant diameter for each section, but their properties can change with the pylon span. The scaled pylon model is shown in *Figure 6.2b*. In *Configuration 2* the pylon is an exact scale down of the full scale model (see *Figure 5.3*). Especially in this last case, the design variables (size of front and rear spar and thickness of the ribs of the pylon) can easily become very small. It should be avoided in order to prevent manufacturing problems and high costs. In both configurations, *Configuration 1* and *Configuration 2*, the scaled pylon is modeled with *Elektron 43*.

6.4 Method 1

Method 1 was described in Section 3.4 and it performs a direct modal response matching. The design variables were introduced earlier in this chapter (see Section 6.3).

Sum of the squares of the residuals (SSR) is the most basic scheme for quantifying differences in the responses. Each term in the response is normalized by its target value. The major drawback of this scheme is the likelihood of near singularities. If target values approach zero, the corresponding objective terms approach infinity. So for the evaluation of translational and rotational mode shapes only nodes with higher values are included in the calculations. The Objective function is shown in *Equation 6.3*,

$$f = AA \cdot \left(\frac{OM - OM^T}{OM^T}\right)^2 + BB \cdot \left(\frac{1^{st}\mathrm{f} - 1^{st}\mathrm{f}^T}{1^{st}\mathrm{f}^T}\right)^2 + CC \cdot \left(\frac{1^{st}TMS - 1^{st}TMS^T}{1^{st}TMS^T}\right)^2 +$$

$$+ DD \cdot \left(\frac{1^{st}RMS - 1^{st}RMS^T}{1^{st}RMS^T}\right)^2 + EE \cdot \left(\frac{2^{nd}\mathrm{f} - 2^{nd}\mathrm{f}^T}{2^{nd}\mathrm{f}^T}\right)^2 + FF \cdot \left(\frac{2^{nd}TMS - 2^{nd}TMS^T}{2^{nd}TMS^T}\right)^2 +$$

$$+ GG \cdot \left(\frac{2^{nd}RMS - 2^{nd}RMS^T}{2^{nd}RMS^T}\right)^2 + HH \cdot \left(\frac{3^{rd}\mathrm{f} - 3^{rd}\mathrm{f}^T}{3^{rd}\mathrm{f}^T}\right)^2 + II \cdot \left(\frac{3^{rd}TMS - 3^{rd}TMS^T}{3^{rd}TMS^T}\right)^2 +$$

$$+LL \cdot \left(\frac{3^{rd}RMS - 3^{rd}RMS^T}{3^{rd}RMS^T}\right)^2 + MM \cdot \left(\frac{4^{th}\mathrm{f} - 4^{th}\mathrm{f}^T}{4^{th}\mathrm{f}^T}\right)^2 + NN \cdot \left(\frac{4^{th}TMS - 4^{th}TMS^T}{4^{th}TMS^T}\right)^2 +$$

$$+OO \cdot \left(\frac{4^{th}RMS - 4^{th}RMS^T}{4^{th}RMS^T}\right)^2 + PP \cdot \left(\frac{5^{th}\mathrm{f} - 5^{th}\mathrm{f}^T}{5^{th}\mathrm{f}^T}\right)^2 + QQ \cdot \left(\frac{5^{th}TMS - 5^{th}TMS^T}{5^{th}TMS^T}\right)^2 +$$

$$+ RR \cdot \left(\frac{5^{th}RMS - 5^{th}RMS^{T}}{5^{th}RMS^{T}}\right)^{2} + SS \cdot \left(\frac{6^{th}\mathrm{f} - 6^{th}\mathrm{f}^{T}}{6^{th}\mathrm{f}^{T}}\right)^{2} + TT \cdot \left(\frac{6^{th}TMS - 6^{th}TMS^{T}}{6^{th}TMS^{T}}\right)^{2} +$$

$$+ UU \cdot \left(\frac{6^{th}RMS - 6^{th}RMS^{T}}{6^{th}RMS^{T}}\right)^{2} + VV \cdot \left(\frac{7^{th}\mathrm{f} - 7^{th}\mathrm{f}^{T}}{7^{th}\mathrm{f}^{T}}\right)^{2} + WW \cdot \left(\frac{7^{th}TMS - 7^{th}TMS^{T}}{7^{th}TMS^{T}}\right)^{2} +$$

$$+ ZZ \cdot \left(\frac{7^{th}RMS - 7^{th}RMS^{T}}{7^{th}RMS^{T}}\right)^{2}$$

Equation 6.3: First objective function

where:

OM	Overall mass
f	Natural frequency
TMS	Translational mode shape
RMS	Rotational mode shape
^{T}	Target value
AA, BB,...,ZZ	Weight parameters

The weights AA, BB, ..., ZZ were chosen in such a way that the mass, frequencies and translational modes have more weight than the rotational modes except for the third and seventh mode. This is due to the fact that in the third mode it is important to match the rotation of the pylon while the seventh mode is the first torsion mode and therefore it is very important to match the torsion behavior of the wing (see *Table 6.11*).

Weight Parameters		First mode	Second mode	Third mode	Fourth mode	Fifth mode	Sixth mode	Seventh mode
Overall Mass	AA 0.08							
Natural frequencies		BB 0.07	EE 0.07	HH 0.06	MM 0.05	PP 0.05	SS 0.04	VV 0.04
Mode shapes	TMS	CC 0.05	FF 0.05	II 0.04	NN 0.05	QQ 0.05	TT 0.05	WW 0.03
	RMS	DD 0.02	GG 0.02	LL 0.04	OO 0.03	RR 0.03	UU 0.03	ZZ 0.05

Table 6.11: Weight parameters

Note that the values of translational and rotational mode shapes must be normalized as described in Section 6.2. The mode shapes errors are the modes shapes average errors, and the values used were only those superior to $|1.0E-02|$, because with inferior values it is more difficult to be precise and the error fluctuate more, which could lead to higher errors.

The optimization process is executed in *Matlab*™, using *Matlab*™*'s fmincon function* and a Sequential Quadratic Programming (SQP) algorithm was applied to minimize the Objective function *f* while at the same time

ensuring that the constraints set are respected.. One issue of this optimization process is the possibility of several local minima. For this work, a search for the global minimum is conducted. Multiple SQP optimizations are executed using random initial design variables. When several analyses are convergent on the same optimized design variables vector, the code ends and saves the latest results.

The design variables are subject to the lower and upper limits. For spars and rungs the lower limits are set at one millimeter in order to avoid manufacturing problems and high costs. The maximum spar width and height is fixed equal to $0.18 \cdot c$ and $0.06 \cdot c$ respectively where c is the local chord. The maximum diameter of the rung is set to be at most equal to the maximum height of the relative spar. The minimum and maximum thickness of the ribs of the pylon (*Configuration 2*) is equal to 1 and 4 millimeters respectively. Thirty six mass points design variables are used and their mass can vary within one gram and 150 grams. The results after the optimization process are summarized in *Table 6.12*.

Method 1	Configuration 1	Configuration 2
	Error	
Overall Mass	7.34%	7.47%
1st Natural Frequency	0.97%	0.98%
2nd Natural Frequency	0.91%	0.84%
3rd Natural Frequency	5.42%	5.59%
4th Natural Frequency	2.78%	2.70%
5th Natural Frequency	3.85%	3.63%
6th Natural Frequency	5.01%	4.82%
7th Natural Frequency	6.67%	6.36%
	Average Error	
1st Translational Mode Shape	1.58%	1.46%
2nd Translational Mode Shape	1.61%	1.29%
3rd Translational Mode Shape	6.26%	5.98%
4th Translational Mode Shape	4.31%	4.01%
5th Translational Mode Shape	4.38%	4.15%
6th Translational Mode Shape	5.89%	5.68%
7th Translational Mode Shape	7.32%	7.16%
1st Rotational Mode Shape	3.16%	2.84%
2nd Rotational Mode Shape	3.48%	3.28%
3rd Rotational Mode Shape	7.22%	6.81%
4th Rotational Mode Shape	3.97%	3.43%
5th Rotational Mode Shape	6.04%	5.88%
6th Rotational Mode Shape	7.23%	6.79%
7th Rotational Mode Shape	7.81%	7.68%
	Global Average Error	
	4.69%	4.49%

Table 6.12: Method 1, results for Configuration 1 and 2

Comparing the results of *Configuration 1* and *Configuration 2*, it is observable that the second approach has a global average error lower than the first approach. Global average error is obtained as an average of the errors (natural frequencies and overall mass) and average errors (translational and rotational mode shapes).

However one can note that the difference in terms of global average error between the two configurations is not very high, it is only 0.20%. This is a proof that the ladder structure even in the event of a pylon is a good solution for aeroelastic scaling problems. *Configuration 1* allows obtaining an error on the overall mass slightly lower than the *Configuration 2* with associate cost of reducing the accuracy of the other parameters.

The optimization process has not been able to obtain errors and average errors less than 5% and this is mainly due to the complexity of the structural model. Nevertheless the results obtained are quite satisfactory, the errors and average errors are below 8% of error for the first seven natural frequencies and associated mode shapes. It is expected, although that by employing a higher number of design variables, the global average error can be reduced, although with a substantial computational time cost increase.

6.5 Method 2

An alternative to Method 1 is the use of two routines to uncouple the mass and stiffness distributions, which needs a static analysis of the full scale model under a determinate load.

A first design optimization is employed to attain the static deflection, using only the size of the front and rear spars, the diameter of the wing rungs and the diameter of the pylon rungs (*Configuration 1*)/thickness of the ribs of the pylon (*Configuration 2*) as design variables.

These design variables are subject to lower and upper limits. The lower limits are set at one millimeter in order to avoid manufacturing problems and high costs. The maximum spar width and height is fixed equal to $0.18 \cdot c$ and $0.06 \cdot c$ respectively where c is the local chord. The maximum diameter of the rung is set to be at most equal to the maximum height of the relative spar. The maximum thickness of the ribs of the pylon (*Configuration 2*) is equal to four millimeters. No lumped masses are introduced in the first routine and the Objective function to minimize is shown in *Equation 6.4*,

$$f = \sqrt{\left(\frac{T_1 - T_1^T}{T_1^T}\right)^2 + \left(\frac{T_2 - T_2^T}{T_2^T}\right)^2 + \left(\frac{T_3 - T_3^T}{T_3^T}\right)^2 + \left(\frac{R_1 - R_1^T}{R_1^T}\right)^2 + \left(\frac{R_2 - R_2^T}{R_2^T}\right)^2 + \left(\frac{R_3 - R_3^T}{R_3^T}\right)^2}$$

Equation 6.4: Second objective function

where:

T_1, T_2, T_3	Translations along the x, y and z body axes respectively
R_1, R_2, R_3	Rotations along the x, y and z body axes respectively
^{T}	Target value

Equation 6.4 includes translations and rotations. It is very important in addition to the vertical translation T_3 to achieve the rotation in pitching R_2 because otherwise the scaled model during a test in a wind tunnel can result with a different pressure distribution and this means in a variation of aerodynamic forces, not calculated a priori.

As discussed in Section 6.4 each translational and rotational value must be normalized.

The values used for the evaluation of the Objective function are only the ones with an average error superior to $|1.0E-02|$, because with inferior values it is more difficult to be precise and the error fluctuate more, which could lead to higher errors.

The goal in the first routine is to minimize the Objective function described in *Equation 6.4* while at the same time satisfying the constraints of maximum stress in the structural components.

With the stiffness distribution achieved in the linear static analysis, a second design optimization routine is performed using the mass points as design variables for the modal analysis. Thirty six mass points design variables are used and they can vary within one gram and 150 grams. The Objective function applied (see *Equation 6.3*) in the second routine is the same as that applied in Method 1. Also the same weight parameters are used (see *Table 6.11*) because it is important to compare the results obtained minimizing the same Objective function for both the Methods.

The results after the optimization process are summarized in *Table 6.13*.

Method 2	Configuration 1	Configuration 2
	Error	
Overall Mass	5.52%	5.71 %
1st Natural Frequency	1.12%	1.14%
2nd Natural Frequency	0.90%	0.86%
3rd Natural Frequency	6.05%	6.93%
4th Natural Frequency	3.61%	3.01%
5th Natural Frequency	4.31%	4.12%
6th Natural Frequency	5.49%	5.21%
7th Natural Frequency	7.68%	7.32%
	Average Error	
Static deflection	1.22%	1.24%
1st Translational Mode Shape	1.52%	1.54%
2nd Translational Mode Shape	1.51%	1.47%
3rd Translational Mode Shape	7.31%	7.12%
4th Translational Mode Shape	4.75%	4.26%
5th Translational Mode Shape	4.91%	4.86%
6th Translational Mode Shape	6.21%	6.04%
7th Translational Mode Shape	7.77%	7.57%

1st Rotational Mode Shape	3.24%	3.12%
2nd Rotational Mode Shape	3.74%	3.50%
3rd Rotational Mode Shape	7.51%	7.21%
4th Rotational Mode Shape	4.03%	3.86%
5th Rotational Mode Shape	6.35%	6.13%
6th Rotational Mode Shape	8.14%	7.54%
7th Rotational Mode Shape	8.92%	8.33%
	Global Average Error	
	4.86%	4.70%

Table 6.13: Method 2, results for Configuration 1 and 2

The first design optimization routine has converged for both the *Configurations* with a very low static deflection error obtained, 1.22% and 1.24% respectively. As discussed in Section 6.4 it is observable that for Method 2 the *Configuration 2* has also a global average error lower than the *Configuration 1*.

6.6 Methods Comparison

In this section the comparison between Method 1 and Method 2 is made only for the best configuration studied in Sections 6.4 and 6.5, i.e. *Configuration 2*. *Table 6.14* summarizes the optimized results for both methods.

	Configuration 2	
	Method 1	**Method 2**
Global average error	4.49 %	4.70%
Computational Time	29.1 *h*	17.4 h (7 *h* + 10.4 *h*)
Number of design variables	86	86 (50 +36)
Front wing spars	The width and the height varies from 61 to 3 millimeter and from 17 to 1 millimeter at root and tip section respectively	The width and the height varies from 55 to 3 millimeter and from 18 to 1 millimeter at root and tip section respectively
Rear wing spars	The width and the height varies from 57 to 1 millimeter and from 18 to 1 millimeter at root and tip section respectively	The width and the height varies from 48 to 2 millimeter and from 18 to 1 millimeter at root and tip section respectively
Diameter of wing rungs	It varies from 15 to 3 millimeter at engine and tip section respectively	It varies from 13 to 3 millimeter at engine and tip section respectively
Pylon spars	There is not a significant difference between the front and rear spar. Width and height varies from 9 to 4 millimeter and from 3 to 1 millimeter, respectively.	There is not a significant difference between the front and rear spar. Width and height varies from 10 to 4 millimeter and from 3 to 1 millimeter, respectively.
Nonstructural mass [kg]	1.052	0.937

Table 6.14: Results Comparison for Configuration 2

From *Table 6.14* it is observable that Method 1 allows obtaining a global average error slightly lower compared to Method 2, but the latter considerably needs less computational time to attain good results. As mentioned previously global average error is obtained as an average of the errors and average errors shown in *Table 6.12* and *6.13*.

The optimization process was performed with a personal computer with these characteristics:

CPU	Intel(R) Core(TM)2 Duo CPU T6400 @ 2.00 GHz
RAM	4.00 GB

The difference between the global average errors of both methods is not high, 0.21%. *Figure 6.3* and *6.4* shows the differences between Method 1 and Method 2 for the *Configuration 2* in order to match the first seven natural frequencies and respective mode shapes of the full model. The ordinate of the plots is normalized with the relative target value in order to improve the interpretation of results (for example in *Figure 6.3* the ordinate of the plot is equal to $\frac{f^T - error \cdot f^T}{f^T}$).

From *Figure 6.3* and *6.4* one can note that Method 1 is the most accurate especially if it is necessary to match the natural frequencies and respective mode shapes over the second mode.

The first natural frequencies and respective mode shapes are pretty simple to check, the last are more complicated for both methods. However, the differences between the two methods are not very high.

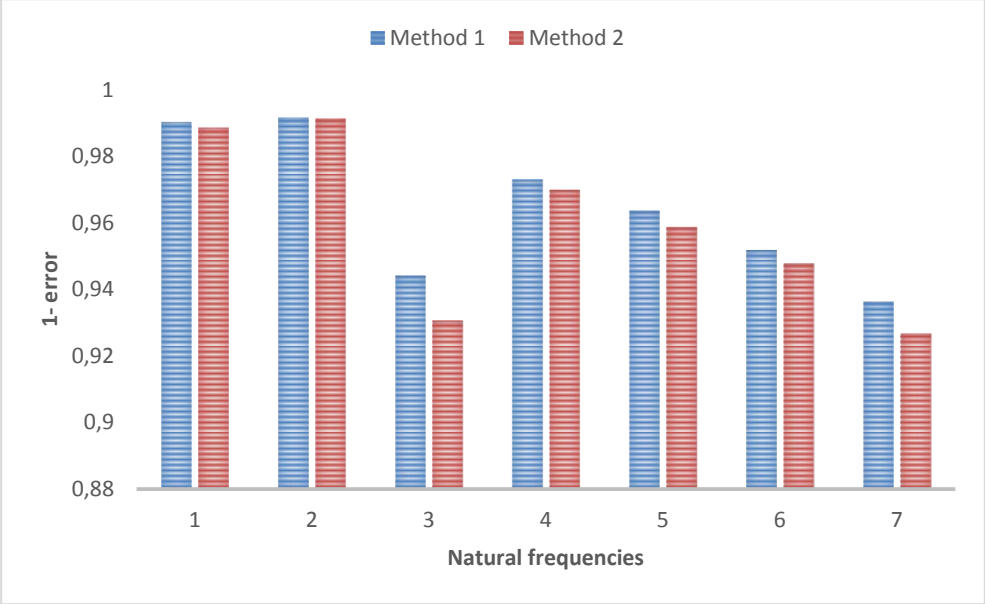

Figure 6.3: Discrepancies between Method 1 and Method 2 for Configuration 2 to match the first seven natural frequencies of the full model

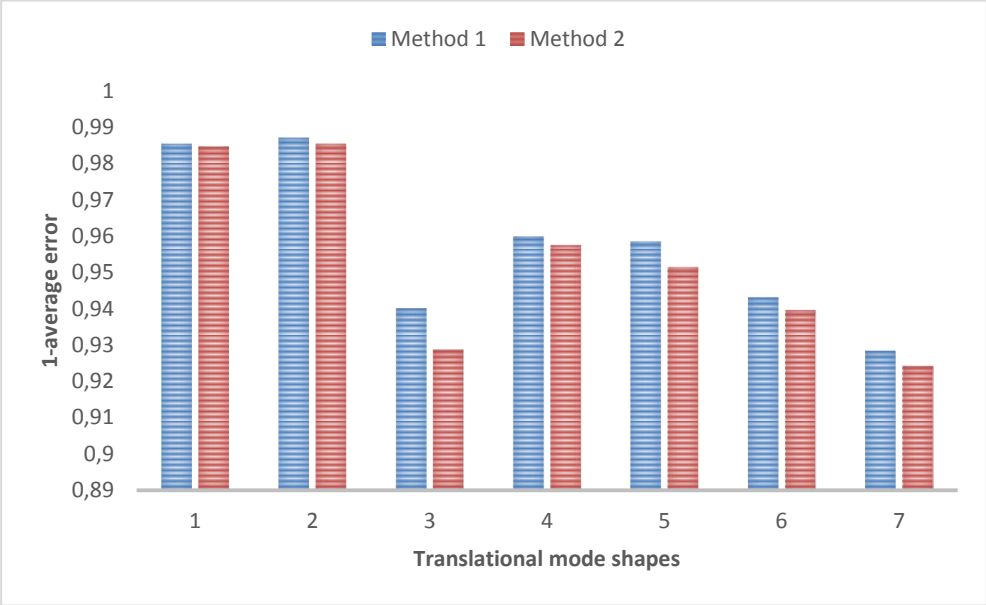

(a): Discrepancies between Method 1 and Method 2 for translational mode shapes

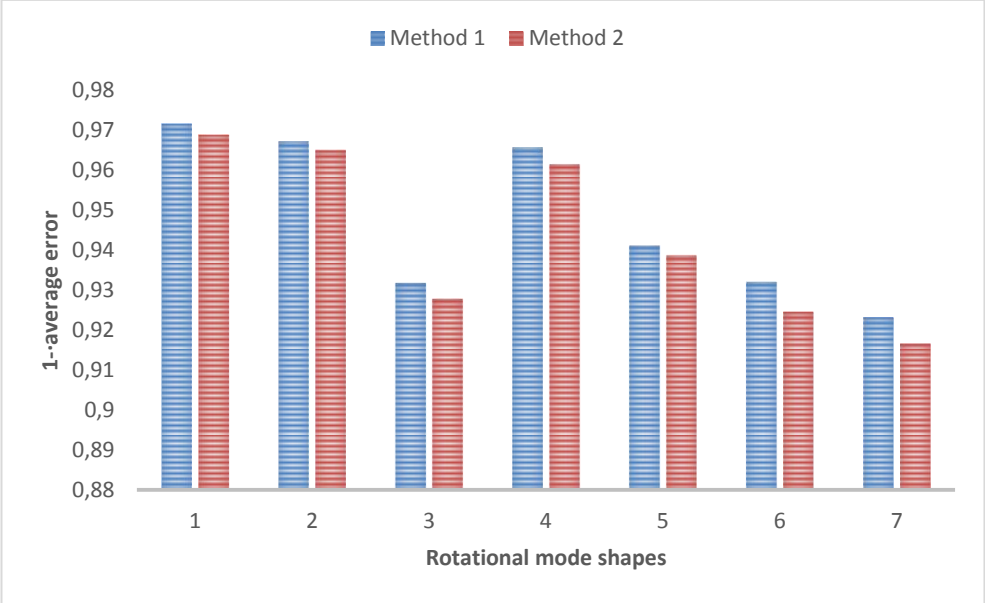

(b): Discrepancies between Method 1 and Method 2 for rotational mode shapes

Figure 6.4: Discrepancies between Method 1 and Method 2 for Configuration 2 to match the first seven mode shapes of the full model

Method 1 is a more robust optimization process due to the coupling of mass and stiffness matrices, but with an advantage of using only one routine. Method 2 uses instead two routines, one for the stiffness distribution matching and the other for the mass distribution matching, but with better computational time efficiency. This is due to the fact that the uncoupling of mass and stiffness distributions leads to simplified optimization routines, which results in a decrease of computational time needed for attaining good modal results.

From the employed scaling methodologies, it is recommended to use the second method, due to the lower computational time required to attain good results, which can be of great relevancy.

In addition the size of the structural elements and the nonstructural mass in Method 2 are lower than in Method 1 and it is the reason because the overall mass error in Method 2 (5.71%) is lower than Method 1 (7.47%). Save structural mass allows building a cheaper scaled model. For these reasons the scaled model obtained in Method 2 is more efficient than the one attained in Method 1.

Figure 6.5 shows the first seven mode shapes for the full and the best design of the scaled models (*Configuration 2,* Method 2) respectively. One can note a good matching for the first mode shapes except for the third because this mode is not representative due to very small full scale mode shape displacements.

Full model **Scaled model**

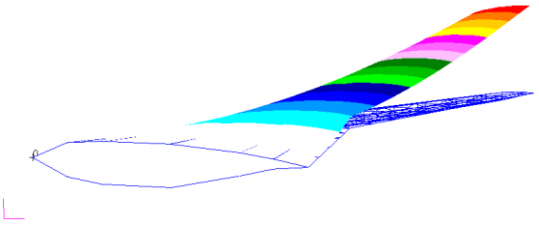

(a): First mode shape

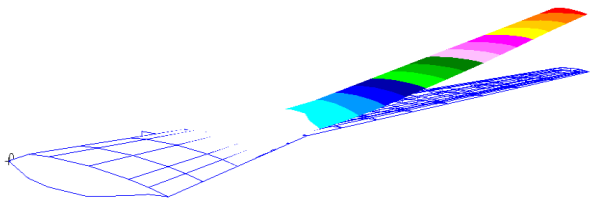

(a'): First mode shape

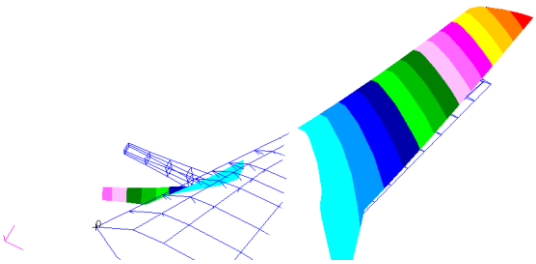

(b): Second mode shape

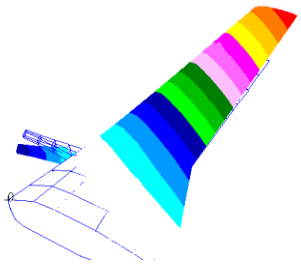

(b'): Second mode shape

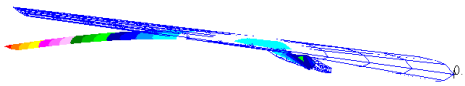

(c): Third mode shape

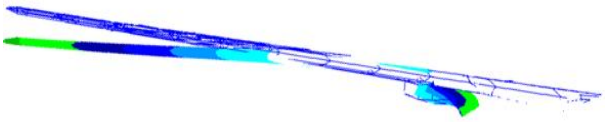

(c'): Third mode shape

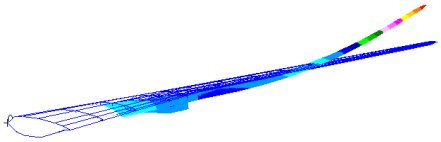

(d): Fourth mode shape

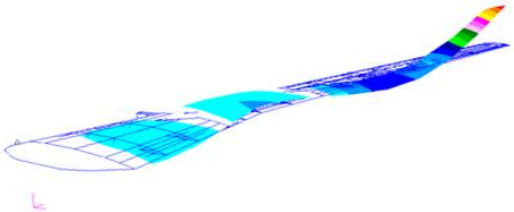

(d'): Fourth mode shape

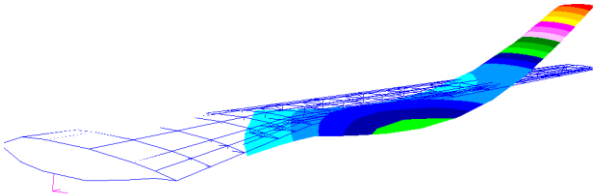

(e): Fifth mode shape

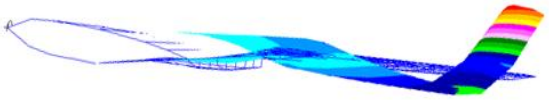

(e'): Fifth mode shape

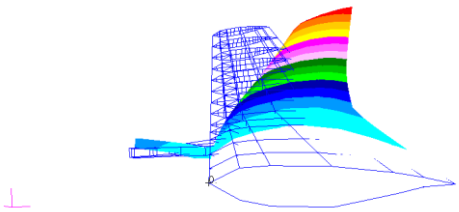

(f): Sixth mode shape

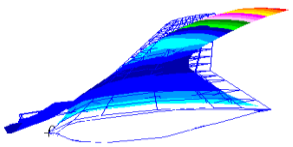

(f'): Sixth mode shape

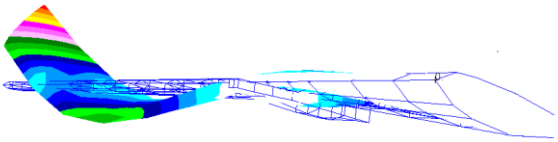

(g). Seventh mode shape

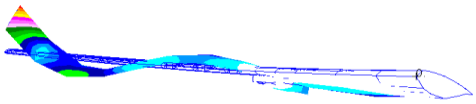

(g'): Seventh mode shape

Figure 6.5: First seven mode shapes for the full model and scaled model (Configuration 2, Method 2) respectively

Table A.1 summarizes the size for the optimized design variables for the best design (*Configuration 2,* Method 2).

6.7 Aeroelastic Analysis

In this section the aeroelastic analysis of the best scaled model, i.e. *Configuration 2* - Method 2, was performed in order to evaluate if the aeroelastic response of the scaled model reproduces the aeroelastic behavior of the baseline wing model. To evaluate the aeroelastic behavior of the scaled model, it was considered the condition of the full scaled aircraft operating at 38000 feet without fuel (see Section 5.4.3).

Since it is planned to perform wing tunnel tests with the scaled wing model, it is important to reproduce in MSC Nastran™ software the procedure followed in wind tunnel, i.e., one has to recreate the same scenery in both tests. Therefore, for the full model one fixed the density in $0333\ \mathrm{kg}\cdot\mathrm{m}^{-3}$ and then one varied the velocity since $175\ m\cdot s^{-1}$ to $600\ m\cdot s^{-1}$, and for the scaled model one fixed the density in $1.225\ \mathrm{kg}\cdot\mathrm{m}^{-3}$ and the velocity varied from $45\ m\cdot s^{-1}$ to $155\ m\cdot s^{-1}$.

In Section 5.4.3 one can note that at 38000 feet with empty tanks for the full model the flutter speed and the corresponding flutter frequency are equal to $V_{FL}=496\ {}^{m}/_{s}$ and $f_{FL}=7.54\ Hz$ respectively. With the scale factors presented in Section 6.2, one can scale the flutter frequency and the flutter speed of the full wing model in order to obtain the corresponding target values for the scaled model. *Table 6.15* shows the aeroelastic target values for the scaled model.

Input Parameters		Output Parameter
$V_{FLf} = 496\ ^{m}/_{s}$ $f_{FLf} = 7.54\ Hz$ $n_v = 0.2569$ $n_f = 3.8924$	$n_v = \frac{V_s}{V_f}$ $n_f = \frac{f_s}{f_f}$	$V_{FLs} = 127.4\ ^{m}/_{s}$ $f_{FLs} = 29.35\ Hz$

Table 6.15: Aeroelastic target values for the scaled model

The aerodynamic panels of the scaled model are built on its deformed state obtained after a nonlinear static analysis in order to evaluate its flutter speed as discussed in Section 5.4.

Table 6.16 shows the discrepancies between aeroelastic target values and the results obtained after an aeroelastic analysis (flutter analysis).

Flutter Mode	Error	
	ΔV_{FL}	Δf_{FL}
4	4.16%	14.52%

Table 6.16: Discrepancies between target and aeroelastic values of the scaled model.

From *Table 6.16* one can see that these values are relatively satisfactory in terms of the velocity's discrepancy. Relatively to the frequency, the results are not good, but in this case the priority is the flutter speed. In aeronautic world it is more important to known the speed that the flutter instability occurs, than to know the exact frequency because independently of the flutter frequency the flutter instability occurs at the specific speed.

Fr-g and *Fr-k* diagram is shown in *Figure 8.2*.

Chapter 7

SCALED MODEL INCLUDING NONLINEAR EFFECTS

7.1 Introduction

The most common practice for classical aeroelastic scaling is to use a truncated number of the vibration mode shapes from the target full scale model as the modal degrees of freedom for the scaled model optimization (see Section 1.1). The matched number can only be a truncated number of the total number of vibration eigenpairs. The truncation is necessary for optimization feasibility.

There is although a drawback, the truncation may omit information that becomes important when geometric nonlinearities are significant. The truncation of higher frequency mode shapes in the modern aeroelastic scaling approach can be considered analogous to not modeling certain flexibilities (e.g., axial and shear) in the classical scaling approach.

This chapter proposes a modern complementary technique (*Equivalent Static Loads - ESL*) intended to help capturing structural nonlinearities. The goal in this chapter is to compare the results obtained with the same scaled structural model when nonlinear effects are included in the calculations.

7.2 Equivalent Static Loads (ELS)

Direct optimization of the nonlinear static response is a computationally intensive task. Efficiency can be gained by transformation to an equivalent linear system using the equivalent static loads approach [45]. The *ESL* is defined as the static load that generates the same displacement field by an analysis which is not linear static.

The current or initial design $\{d\}$ and loading conditions $\{F\}$ are specified. Nonlinear static analysis provides the nonlinear static deformations $\{x_{NL}\}$ by solving the nonlinear equation of equilibrium (see *Equation 7.1*):

$$[K_{NL}(d)]\{x_{NL}\} = \{F\}$$

Equation 7.1: Nonlinear equation of equilibrium

The load set that will result in equivalent linear static displacements and rotations $\{F_{eq}\}$ is determined by multiplying the nonlinear deformations by the linear stiffness matrix $[K_{Lin}]$ (see *Equation 7.2*).

$$\{F_{eq}\} = [K_{Lin}(d)]\{x_{NL}\}$$

Equation 7.2: Evaluation of the equivalent static loads

Efficient optimization process can be performed on the equivalent linearized system (see *Equation 7.3*).

$$[K_{Lin}(d)]\{x_{Lin}\} = \{F_{eq}\}$$

Equation 7.3: Equivalent linearized system

The *ESL* approach requires an iterative procedure that updates the linearized system as the design changes. The optimization converge when:

$$\left\|d^{(k+1)} - d^{(k)}\right\| \leq \varepsilon$$

Equation 7.4: Stopping criteria

where ε is a tolerance parameter and it is a small number.

The basic idea of *ESL* is presented in *Figure 7.1*.

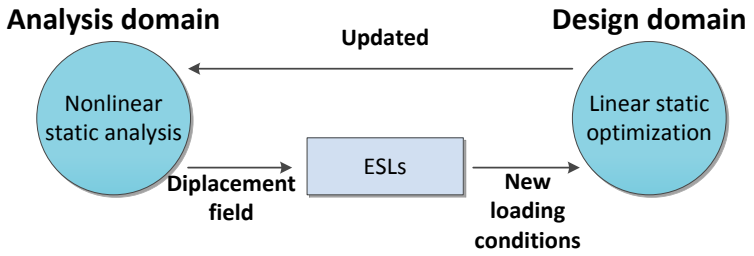

Figure 7.1: Schematic process between the analysis and the design domain respectively

The optimization process is divided into two domains: analysis domain and design domain. Nonlinear static analysis is performed in the analysis domain. The nonlinear displacement field is evaluated and the equivalent load sets are calculated to ensure the same displacement field between nonlinear and linear static analysis. The equivalent load sets are transferred to the design domain. In the design domain, linear static optimization is performed by using the equivalent loads as external loads. The design variables are updated in the design domain and nonlinear static analysis is performed again with the update design variables. The process proceeds until the convergence criteria is satisfied (see *Equation 7.4*). The scaling methodology implemented in order to obtain a new scaled model including geometric nonlinearities is shown in *Figure 7.2*.

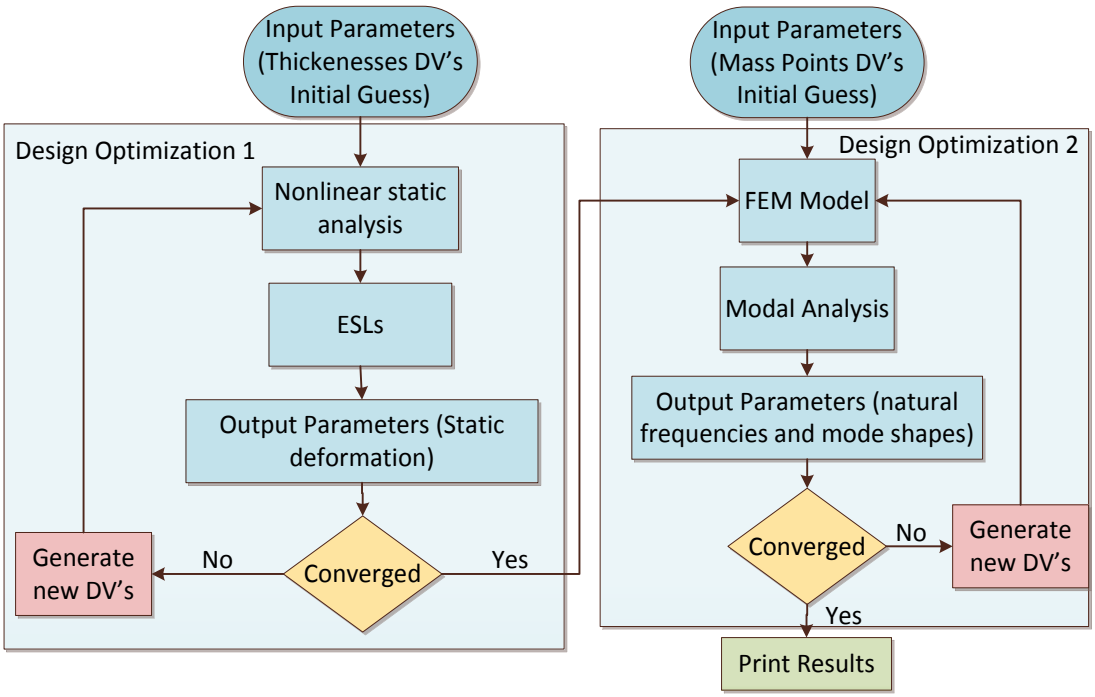

Figure 7.2: Scaling methodology including geometric nonlinearities

As a first step, a baseline scaled model was designed using a classical approach intended for linear aeroelastic scaling (see Chapter 6). The best design (see Section 6.6) provides a favorable initial design and a control for evaluating the modified method.

In this new methodology the aeroelastic response of the scaled model will be attained if the stiffness and mass distributions are matched separately. The differences between this new methodology (see *Figure 7.2*) and Method 2 (see *Figure 3.2*) is essentially in the evaluation of the first routine. A nonlinear static analysis of the scaled model is performed in order to evaluate the nonlinear displacement field. The *ESL* approach is used in order to perform a classical linear static optimization of the scaled model. The optimization process in the Design domain (see *Figure 7.1*) is performed in *Matlab*™ using *Matlab*™*'s fmincon function* and applying Sequential Quadratic Programming (SQP) algorithm. The static deflection error is calculated, which is the unique state variable of the design optimization that is applied and also the only parameter that takes part of the Objective function to be minimized in the first routine. When the structure stiffness is achieved, concentrated masses are added to attain the desired mass distribution. So the modal analysis is performed, from which the modal results are obtained and the respective errors are evaluated. The errors are the state variables of the design optimization process and take also part of the Objective function to be minimized in the second routine. Once the objective modal result errors and convergence are achieved the final results are saved.

The Objective function to minimize in the first and in the second routine is shown in *Equation 6.4* and *Equation 6.3* respectively. For this new scaling methodology the same weight parameters are used (see *Table 6.11*) because it is important to compare the results obtained minimizing the same Objective function for both the scaled models obtained applying classical and modern scaling methodology respectively.

7.3 Build a Scaled Model

The scaled model built in this section is analogous to the model obtained in Section 6.3 (*Configuration 2*). The same design variables with lower and upper limits are used in this new optimization process.

The purpose of this section is to compare the results between the optimized design obtained in Section 6.6 (*Configuration 2*, Method 2) with the same structural model obtained by applying the methodology represented in *Figure 7.2*.

The same scaling factors applied in Chapter 6 (see Section 6.2) are applied in this section and therefore the target values remain unchanged.

The only difference in this new methodology is a nonlinear analysis in the first routine (see *Figure 7.2*) and therefore the target value for the static deflection is different from *Table 6.7* which was obtained by a linear static analysis. *Table 7.1* shows this new target value.

Input Parameters		Output Parameter
$w_f = 0.81\ m$ $n_g = 0.066$	$\frac{w_s}{w_f} = n_g$	$w_s = 0.053\ m$

Table 7.1: Non linear scaled static deflection

Note that the subscripts of *s* and *f* represent scaled and full scale respectively.

This new scaled model was again designed in order to match the first seven natural frequencies and respective mode shapes of the full model with a discrepancy of 5%. Also the overall mass should not exceed a 5% of error margin.

7.4 Scaled Model Results

The design optimization converges in seven nonlinear iterations and the final results are summarized in *Table 7.2*. Global average error is obtained as an average of the errors (overall mass and natural frequencies) and average errors (static deflection and translational and rotational mode shapes).

Comparing the results between *Table 7.2* and *6.13* one can note a global average error lower when the *Equivalent Static Loads* approach is used (see *Table 7.3*). The main improvement concerns the matching of the overall mass and the sixth and seventh mode shape.

	Configuration 2
	Error
Overall Mass	2.34
1st Natural Frequency	0.98
2nd Natural Frequency	1.98
3rd Natural Frequency	6.12
4th Natural Frequency	3.12
5th Natural Frequency	4.09
6th Natural Frequency	4.55
7th Natural Frequency	5.94
	Average Error
Static deflection	1.42
1st Translational Mode Shape	1.12
2nd Translational Mode Shape	2.06
3rd Translational Mode Shape	6.41
4th Translational Mode Shape	2.14
5th Translational Mode Shape	5.12
6th Translational Mode Shape	6.48
7th Translational Mode Shape	6.12
1st Rotational Mode Shape	3.21
2nd Rotational Mode Shape	3.34
3rd Rotational Mode Shape	6.12
4th Rotational Mode Shape	4.11
5th Rotational Mode Shape	5.46
6th Rotational Mode Shape	4.98
7th Rotational Mode Shape	5.21
	Global Average Error
	4.01

Table 7.2: ESL optimization, results for Configuration 2

Figure 7.3 and *7.4* shows the differences between the classical (see Chapter 6 - Method 2) and modern (*ESL*) approaches to match the first seven natural frequencies and respective mode shapes of the full model. The ordinate of the plots is again normalized with the relative target value in order to improve the interpretation of results (see Section 6.6).

It may be noted that the modern approach, in this case, allows to match mainly the translations of the fourth mode shape (see *Figure 7.4a*) and the rotations of the sixth and seventh mode shape (see *Figure 7.4b*).

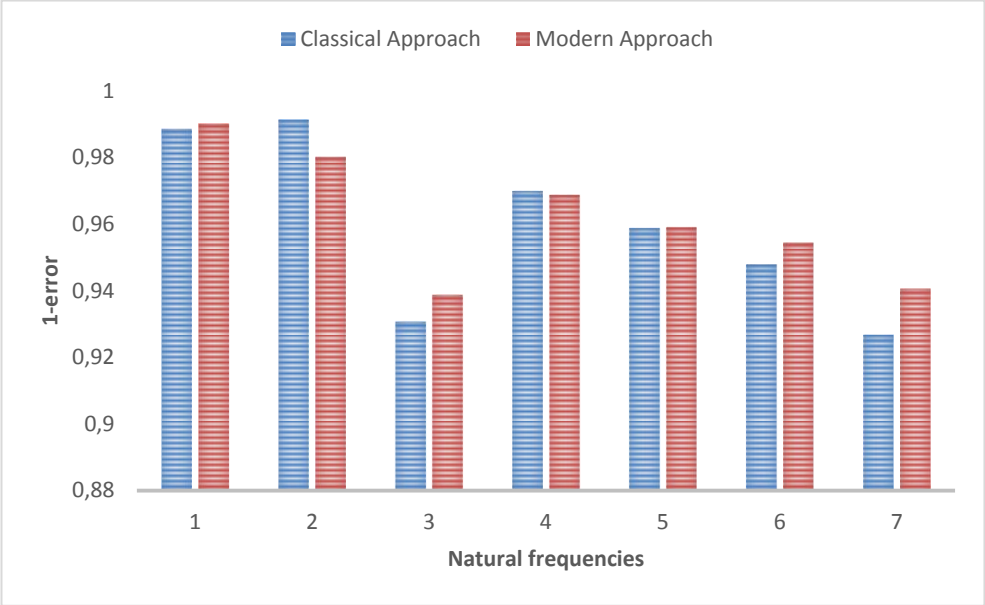

Figure 7.3: Discrepancies between classical (Method 2) and modern approach (ESL) for Configuration 2 to match the first seven natural frequencies of the full model

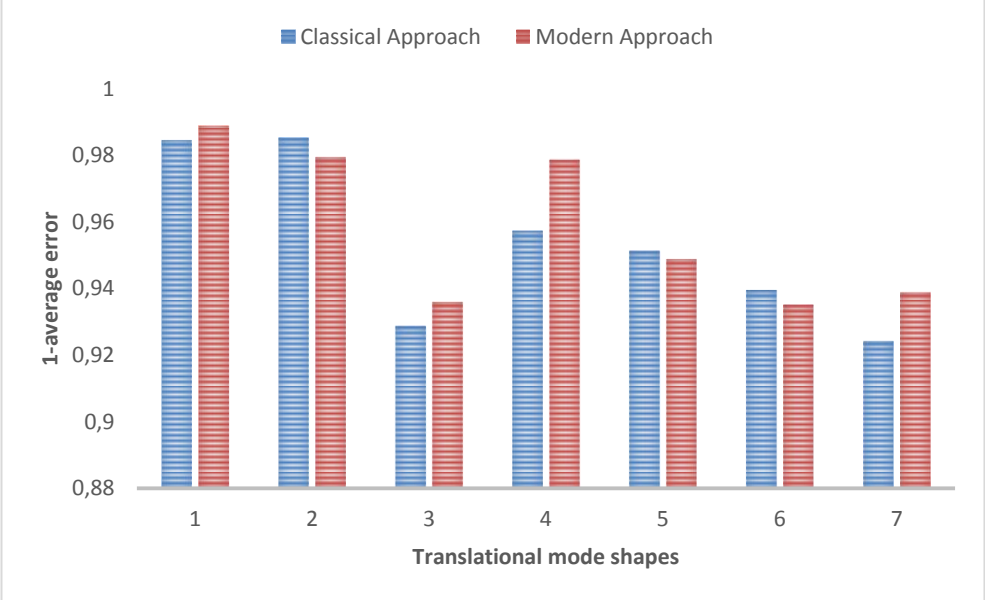

(a): Discrepancies between classical and modern approach for translational mode shapes

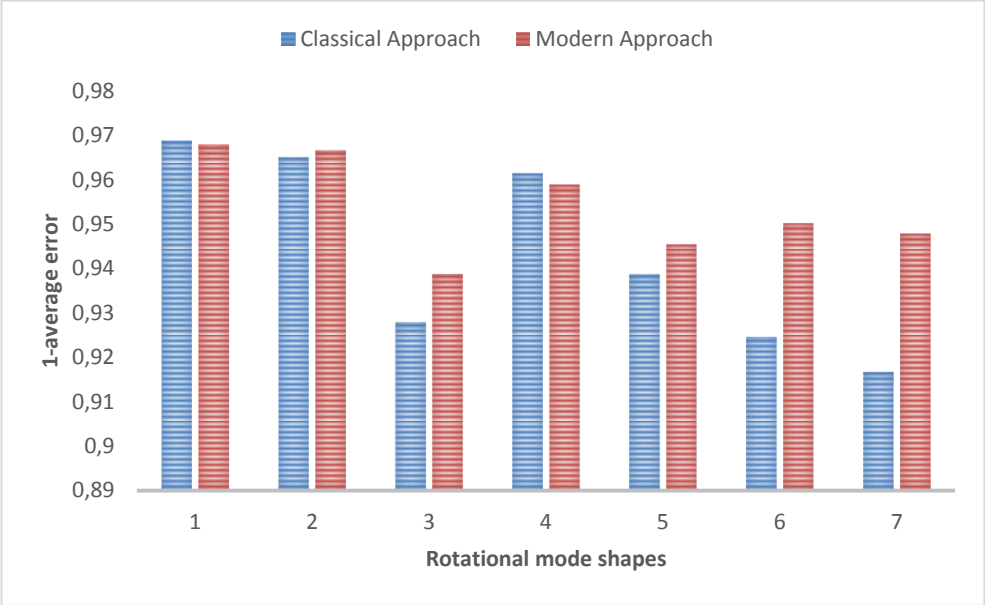

(b): Discrepancies between classical and modern approach for rotational mode shapes

Figure 7.4: Discrepancies between classical (Method 2) and modern approach (ESL) for Configuration 2 to match the first seven mode shapes of the full model

Table 7.3 summarizes the main differences between the classical and modern approach.

	Configuration 2	
	Classical Approach (Method 2)	**Modern Approach (ESL)**
Global average error	4.70 %	4.01%
Computational Time	17.4 h (7 *h* + 10.4 *h*)	55 h (47 *h* + 8 *h*)
Number of design variables	86	

Table 7.3: Results Comparison for Configuration 2

From *Table 7.3* it is observable that the modern approach allows obtaining a global average error lower compared to classical approach, but the latter considerably needs less computational time to attain good results. Therefore, the modern approach is not recommended when the structure does not experience nonlinear effects. In addition, the optimization process in the modern approach was not able also to obtain errors and average errors less than 5% and this is mainly due to the complexity of the structural model.

The size of the structural elements in the modern approach (see *Table A2*) are lower than the classical approach (see *Table A1*) and it is the main reason because the overall mass error in modern approach (2.34%) is lower than the classical approach (5.71%).

The optimization process was performed also in this section with a personal computer with the same characteristics as described in Section 6.6.

The aeroelastic analysis of the scaled model obtained applying the modern approach was performed to verify if the aeroelastic response of the scaled model reproduces the aeroelastic behavior of the baseline wing model.

To evaluate the aeroelastic behavior of the scaled model, it was considered the condition of the full model operating at 38000 feet without fuel (see Section 5.4.3). *Table 6.15* shows the aeroelastic target values for the scaled model (see Section 6.7). *Table 7.4* shows the discrepancies between aeroelastic target values and the results obtained after an aeroelastic analysis (flutter analysis) when nonlinear effects are included in the scaled model.

Flutter Mode	Error	
	ΔV_{FL}	Δf_{FL}
4	2.31%	6.52%

Table 7.4: Discrepancies between target and aeroelastic values of the scaled model obtained applying the modern approach

Comparing the results summarized in *Table 7.4* and *6.16* one can note that applying the modern approach allows to obtain errors lower than the classical approach. Especially the flutter frequency error tends to decrease significantly.

Fr-g and *Fr-k* diagram is shown in *Figure 8.2*.

Optimized design variables obtained applying the modern approach are listed in *Table A2* while *Figure 7.5* shows the first seven mode shapes of the new scaled model.

New scaled model

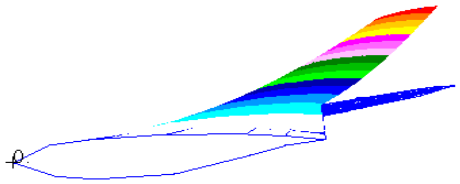

(a): First mode shape

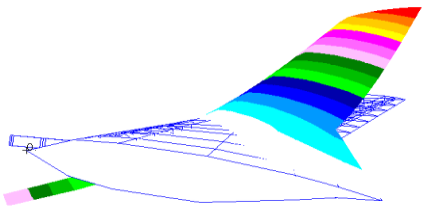

(b): Second mode shape

(c): Third mode shape

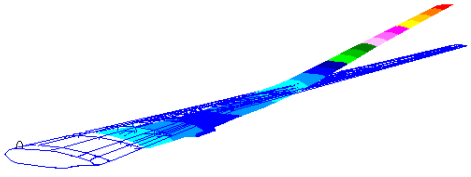

(d): Fourth mode shape

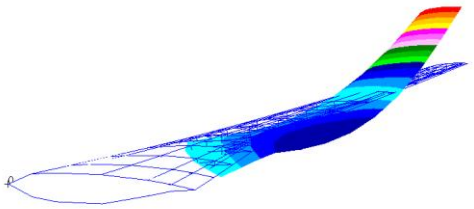

(e): Fifth mode shape

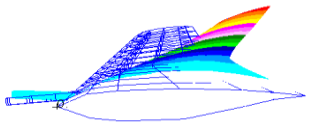

(f): Sixth mode shape

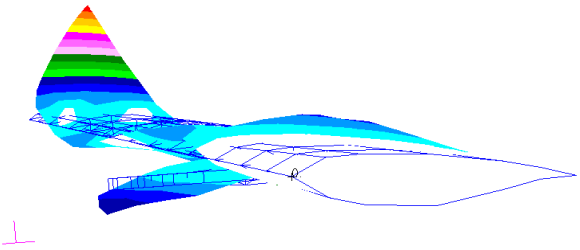

(g): Seventh mode shape

Figure 7.5: First seven mode shapes for the scaled model obtained applying the modern approach

Chapter 8

CONCLUSIONS AND FUTURE WORK

This dissertation aimed to address methodology needs for aeroelastic scaling of aircraft with geometrically nonlinear behavior. Classical and modern approaches to aeroelastic scaling were reviewed. Truncation of higher-frequency modal degrees of freedom from the classical scaling optimization may lead to designs that do not correctly capture the nonlinear kinematic effects.

Two methods, Method 1 and Method 2, describing the classical approach for aeroelastic scaling were developed. Aerodynamic scaling was accomplished by analytically matching the scaled flight condition through selection of the test altitude and speed. The structural properties could not realistically be matched analytically. Partial global similitude was achieved by optimization of a truncated number of mode shapes so that they matched the scaled target values. Method 1 uses a single-step direct modal matching. Natural frequencies and mode shapes are matched in a simultaneous optimization analysis. In Method 2 a two-step optimization procedure is used. First, the structure is designed to minimize the differences in scaled static deflections between the design and target model. Then, assuming the structure stiffness complete and accurate, nonstructural masses are designed by constraining the natural frequencies to match the scaled ones while at the same time minimizing the differences between reduced and full scaled models mode shapes.

The first question in this dissertation was to decide how to model the pylon. Usually in aeroelastic scaled models only the wing is scaled as a ladder structure, but in this case it was decided to scale also the pylon. Two different *Configurations* have been developed for this purpose, *Configuration 1* and *Configuration 2*. In *Configuration 1* the pylon is modeled as a ladder structure while in *Configuration 2* it is an exact scale down of the full model. The results summarized in *Table 6.12* and *6.13* show that the choice to approximate the pylon with a ladder structure is not wrong, in fact the global average error between *the two Configurations* is equal to 0.20% and 0.16% for Method 1 and Method 2 respectively. *Configuration 2* allows to obtain more accurate results. Global average error is obtained as an average of the computed errors, which contains natural frequencies, overall mass, translational and rotational mode shapes, and in Method 2 case the static deflection is also included.

The difference between the global average errors of both methods, Method 1 and 2, for *Configuration 2* is small, 0.21%. Method 1 is a more robust optimization process due to the coupling of mass and stiffness matrices. Method 1 allows obtaining a global average error slightly lower compared to Method 2 which uses two routines instead, one for stiffness distribution matching and the other for mass distribution matching. The latter

(Method2) considerably needs less computational time to attain good results. From the employed scaling methodologies, it is recommended to use Method 2, due to the lower computational time required to attain good results, which can be of great relevancy.

A modern aeroelastic approach using *Equivalent Static Loads (ESL)* for nonlinear static response matching was used in order to help capturing structural nonlinearities. This was the first demonstration of an optimization simultaneously combining *Equivalent Static Loads* for nonlinear statics with structural dynamics for high aspect ratio wings. The main goal is to compare the results obtained with the same *Configuration* of scaled model (*Configuration 2*) when classical (Method 2) and modern approach (ESL) are performed.

Results in *Figure 7.3* and *7.4* show that when the structure experiences nonlinear effects, matching nonlinear static response and mode shapes allows to obtain a more accurate scaled model. Nonlinear tip wing deflection obtained using the modern approach is compared to the target and traditionally designed model in *Figure 8.1*. Tip wing deflection error is reduced to 14% and 11% at 4g for classical and modern approach, respectively. The trend of the tip wing deflection is considerably better when the scaled model is obtained using the modern approach.

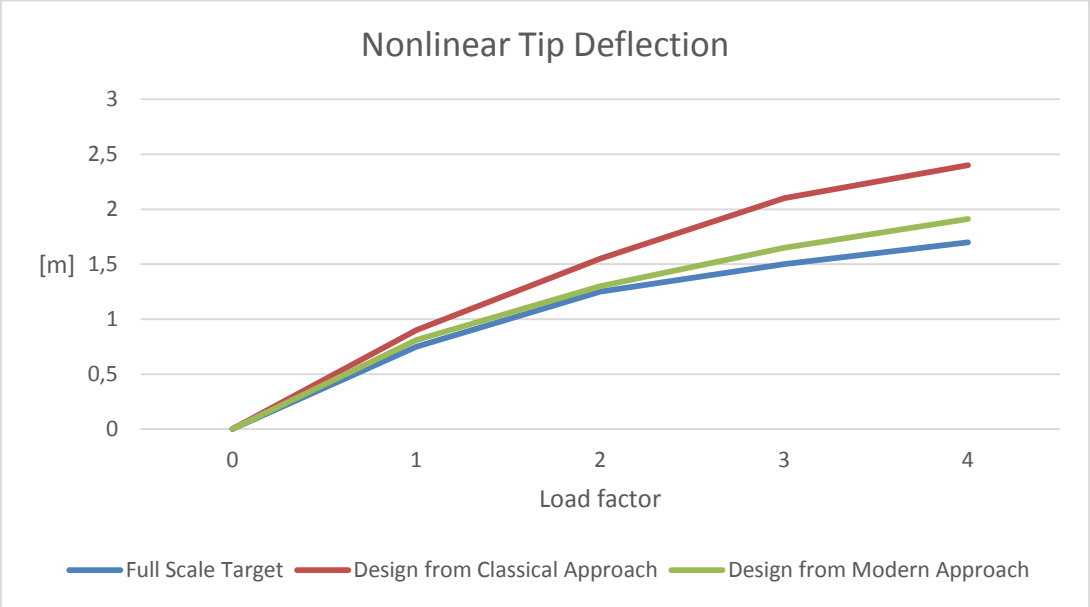

Figure 8.1: Nonlinear tip deflection

Figure 8.2 shows the *Fr-g* and *Fr-k* diagram for mode 4 and 7 when the classical and modern approach are applied in order to match the aeroelastic response of the full model. In this figure it was decided to include only the fourth and the seventh mode because the flutter mode is due to a combination of these two modes (see Section 5.4.3). In the plot appears *Fr* which is the Froude number (see Section 3.3) while *k* is the reduced frequency and it is evaluated as:

$$k = \frac{f \cdot b}{V}$$

Equation 8.1: Reduced frequency

The *Fr-g* and *Fr-k* diagram are necessary to include on the same plot the target values of the full model and the values achieved from the scaled model obtained by classical and modern approach, respectively. The aeroelastic response is considerably more agreeable when the modern approach is applied in fact the accuracy is noticeably better than the results obtained for traditionally scaled models.

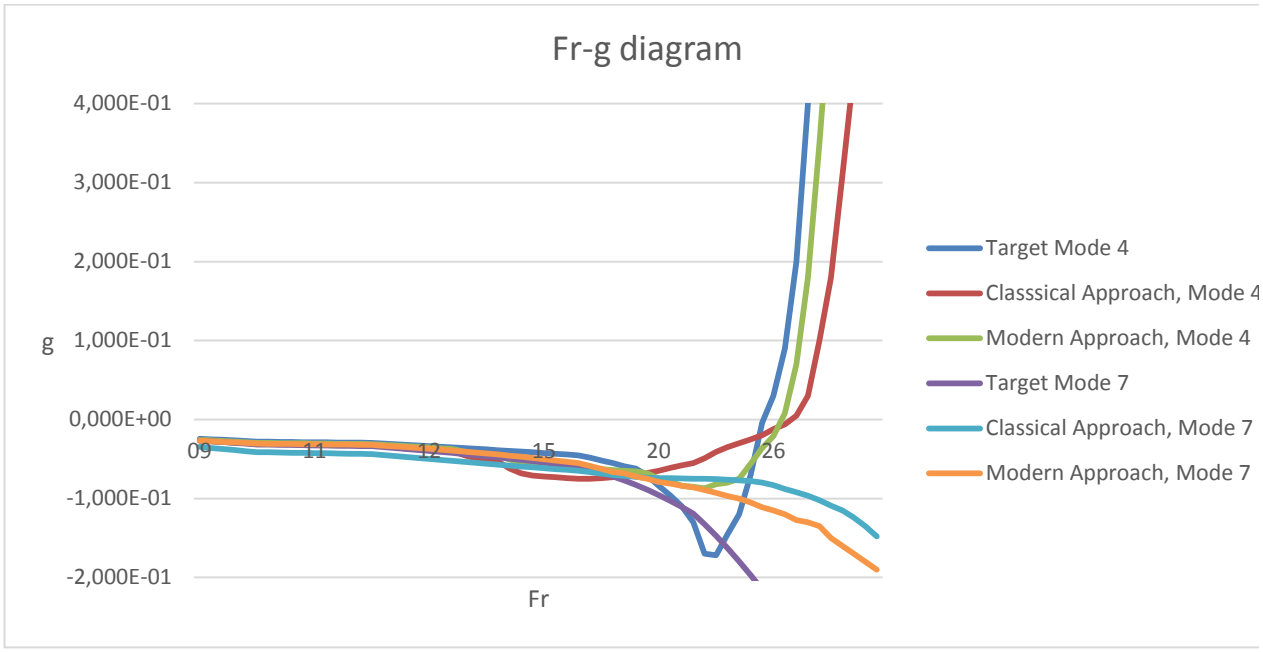

(a): Fr-g diagram

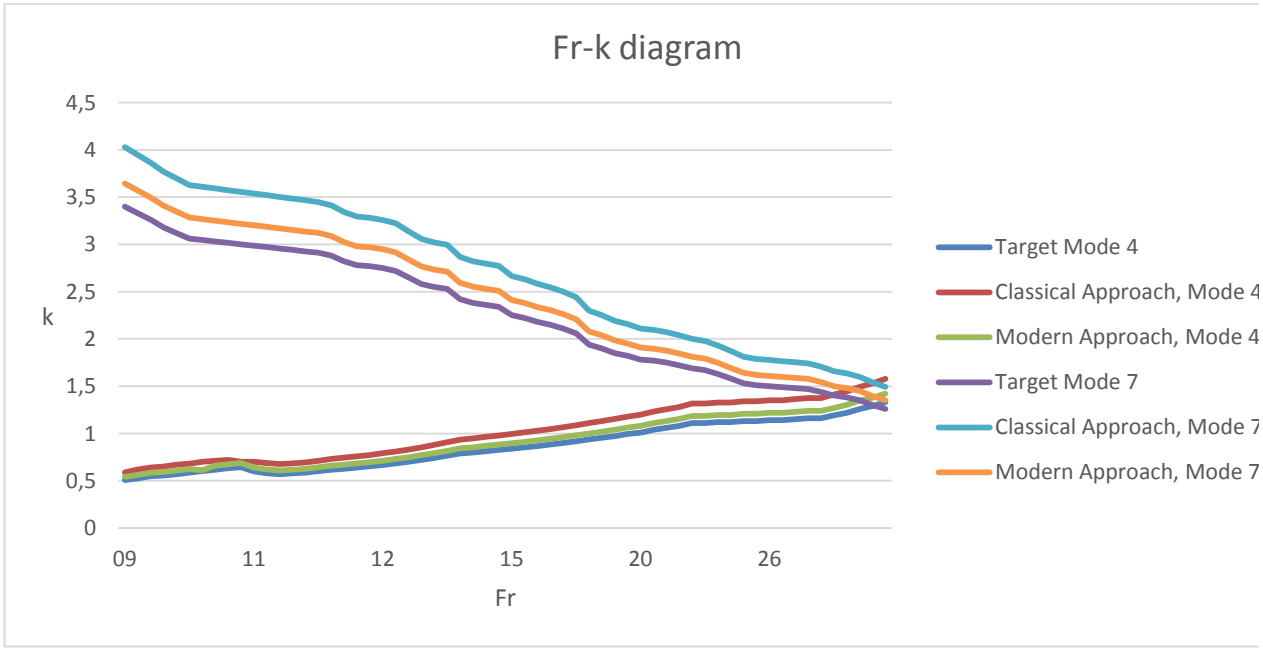

(b): Fr-k diagram

Figure 8.2: Aeroelastic results for classical and modern approach for mode 4 and 7 respectively

The main recommendations of this work pervade beyond geometrically nonlinear applications to any modern aeroelastic scaling program.

Each term of the Objective functions must be normalized by its target value in order to increase the convergence speed of the problem.

The modern approach allows obtaining a global average error lower compared to classical approach, but the latter considerably needs less computational time to attain good results. Therefore, the modern approach is not recommended when the structure does not experience nonlinear effects.

In addition, local optima may occurs in the design optimization because the Objective function is nonlinear with respect to the design variables and because the optimization problem can be underdetermined. A global search is recommended for optimization process to avoid results with low accuracy.

In the near future, the presented modifications (*ESL*) for the modern aeroelastic scaling approach should be tested for scaling aircraft with high aspect ratio wings.

In the longer term, the results obtained in this dissertation should be applied to design experimental testing models that can demonstrate nonlinear geometric aeroelastic responses in flight. The scaled model should be tested in a wind tunnel for validating the applied methodology. The design methodology should be tested on higher fidelity computational models with more complex structural layouts (including for example composite materials, flight control surfaces, pylon modeled with a titanium alloy, a more accurate structural model in MSC Nastran^{TM} software using solid elements, instead of just beam and shell elements, wing attachment should be also considered) and specially aerodynamic models. Comparison of nonlinear transient response to atmospheric gust should also be considered in the scaled model validation.

Bibliography

[1] Abbott, I., H. and Von Doenhoff, A. E., "Theory of Wing Sections, Including a Summary of Airfoil Data", Dover Pubblications, Inc., 1959

[2] Afonso, F., "Dynamic Scaling of a Joined Wing Aircraft Configuration", MSc Thesis, Universidade Técnica de Lisboa - Instituto Superior Técnico, July 2011

[3] Albano, E., and Rodden, W. P., "A Doublet Lattice Method for Calculating Lift Distributions on Oscillating Surfaces in Subsonic Flows", AIAA J., Vol. 7, 1969

[4] ASM Aerospace Specification Metals Inc., "Aluminium 7075-T6, 7075-T651", [online], 2014, [Cited: May 21, 2014], http://asm.matweb.com/search/SpecificMaterial.asp?bassnum=MA7075T6

[5] ASM Aerospace Specification Metals Inc., "AISI Type Stainless Steel", [online],2014, [Cited: May 21, 2014], http://asm.matweb.com/search/SpecificMaterial.asp?bassnum=MQ304A

[6] Bhasin, S., " An Interface for Aeroelastic Analysis of Joined Wing Configuration Including Structural Non Linearities", PhD Dissertation, San Diego State University, Ca, USA, 2011

[7] Bisplinghoff, R. L., Ashley, H. and Halfman, R. L., "Aeroelasticity", Dover Pubblications, Addison-Wesley Publishing Company, Inc., New York, USA, 1996

[8] Bond, V. L., Canfield, R. A., Suleman, A. and Blair, M., "Aeroelastic Scaling of a Joined Wing for Nonlinear Geometric Stiffness", AIAA Journal, 50:513-522, 2012

[9] Buckingham, E. "On Physically Similar Systems; Illustrations of the Use of Dimensional Equations", Phys. Rev., 4:345-376, 1914

[10] Cecrdle, J. and Vich, O., "Eigenvalue and Flutter Sensitivity Analysis of Airliner Wing", 28th International Congress of the Aeronautical Sciences, ICAS 2012, 2012

[11] Cesnik, C. E. S., Patil, M. J. and Hodges, D. H., "Non Linear Aeroelasticity and Flight Dynamics of High-Altitude Long Endutrance Aircraft", AIAA Paper-99-1470, 1998

[12] Cooper, Professor J. E., et al., "Experimental Validation of an Aeroelastically Scaled Sensorcraft Model", EOARD Contract FA 8655-07-1-3111, 2007

[13] Cooper, J. E. and Harmin, M. Y., "Dynamic Aeroelstic Prediction for Geometrically Nonlinear Arcraft", IFASD,2001.

[14] Corke, T. C., "Aircraft Design", Pearson Education, Inc, 2003

[15] Cox, D. and Curtiss, J. H., "A Modern Course in Aeroelasticity", 4th edition Netherlands: Sijthoff and Noordhoff, 2004

[16] Dorbath, F., Nagel, B. and Gollnick, V., "A knowledge Based Approach for Automated Modeling of Extended Wing Structures in Preliminary Aircraft Design", German Aerospace Center (DLR), Hamburg

[17] Drela, M., "Integrated Simulation Model for Preliminary Aerodynamic, Structural, and Control-Law Design of Aircraft", In AIAA/ASME/ASCE/AHS/ASC Structures, Structural Dynamics, and Materials Conference and Exhibit, 40th, 1999

[18] FAA Federal Aviation Regulations (FARS, 14 CFR), [online], 2014, [Cited: May 24, 2014], http://www.flightsimaviation.com/data/FARS/part_25-629.html

[19] Frazer, R. A. and Duncan, W. J., "The Flutter of Aeroplane Wings", British A.R.C., R. & M., 1155

[20] French, M., "An Application of Structural Optimization in Wind Tunnel Design", AIAA/ASME/ASCE/AHS/ASC Structures, Structural Dynamic and Materials Conference, CA, USA, 1990

[21] French, M., "Design of Aeroelastically Scaled Wind Tunnel Models Using Sensivity Based", School of Enginnering, University of Dayton, 1993

[22] French, F. and Eastep, F. E., "Aeroelastic Model Sesign Using Parameter Identification", Journal of Aircraft, 33(1):198-202, 1996

[23] Galeán, O., "Optimization and Redesign of the Reaming Beam for Airbus A350 Pylons", Phd Thesis, Universidad Pontificia ICAI ICADE COMILLAS, Madrid, 2012

[24] Giesing, J. P., Kalman, T. P. and Rodden, W. P., "Subsonic Unsteady Arodynamics for General Configurations", Part I, Vol I - Direct Application of the Nonplanar Doublet-Lattice Method, Air Force Flight Dynamics Laboratory Report No. AFFDL-TR-71-5, 1971

[25] Giesing, J. P., Kalman, T. P. and Rodden, W. P., "Subsonic Unsteady Arodynamics for General Configurations", Part II, Vol I - Application of the Doublet-Lattice Method and the Method of Images to Lifting-Surface/Body Interference, Air Force Flight Dynamics Laboratory Report No. AFFDL-TR-71-5, 1972

[26] Giesing, J. P., Kalman, T. P. and Rodden, W. P., "Subsonic Unsteady Arodynamics for General Configurations", Part II, Vol II -Computer Program N5KA, Air Force Flight Dynamics Laboratory Report No. AFFDL-TR-71-5, 1972

[27] Giesing, J. P., Kalman, T. P. and Rodden, W. P., " Subsonic Steady and Oscillatory Aerodynamics for Multiple Interfering Wings and Bodies", J. Aircraft, Vol. 9, 1972

[28] Green, D. W., Winandy, J. E. and Kretschmann, D. E., "Mechanical Properties of Wood", Chapter 4, [online], 2014, [Cited: May 21, 2014], http://www.conradfp.com/pdf/ch4-Mechanical-Properties-of-Wood.pdf

[29] Hassig, H. J., "An approximate True Damping Solution of the Flutter Equation by Determinant Iteration", J. Aircraft, Vol. 8, 1971

[30] Jinwu, X., Yongju, Y. and Daochun, L. "Recent Advance in Nonlinear Aeroelastic Analysis and Control of the Aircraft", Chinese Journal of Aeronautics, CSAA, 2013

[31] Kim, Y. I., Park, G. J., Kolonay, R. M., Blair, M. and Canfield, R. A., "Nonlinear Response Structural Optimization of a Joined Wing Using Equivalent Loads (ESL)", AIAA journal, 46(11):2703-2713, 2008

[32] Kratochvìl, A. and Slavik, S., "Aeroelasticity Analysis of Wing UL-39", [online],2014, [Cited: May 21, 2014], http://stc.fs.cvut.cz/pdf/KratochvilAles-320194.pdf

[33] Lee BHK, Price SJ, Wong YS., "Nonlinear Aeroelastic Analysis of Airfoil: Bifurcation and Chaos", Prog. Aerospace, Sci, 1999

[34] Lee, H. A., Kim, Y. I., Park, G. J., Kolonay, R. M., Blair, M. and Canfield, R. A., "Structural Optimization of a Joined Wing Using Equivalent Static Loads", Journal of AIrcraft, 44(4):1302-1308, 2007

[35] Liu, D., Chen, P., Zhang, Z. and Wang, Z., "Continuous Dynamic Simulation of Morphing Wing Aeroelasticity", 50th AIAA Structures, Structural Dynamics and Materials Conference, Palm Springs, CA.AIAA-2009-2572, 2009

[36] Maffei, F., "Analisi di Whirl Flutter per un Convertiplano di Nuova Generazione", PhD thesis, Università Degli Studi di Napoli "FEDERICO II"

[37] Magnesium Elektron, Service & Innovation in Magnesium, "Elektron 43", [online],2014, [Cited: May 21, 2014], http://www.aircraftinteriorsexpo.com/__novadocuments/32293?v=635100810391270000

[38] MathWorks, "fmincon", [online], 2014, [Cited: May 21, 2014], http://www.mathworks.com/help/optim/ug/fmincon.html

[39] Matlab Toolbox, "SQP Implementation", [online], 2014, [Cited: May 21, 2014], http://nf.nci.org.au/facilities/software/Matlab/toolbox/optim/tutor16b.html

[40] Megson, T. H. G., " Aircraft Structures for Engineering Structures", Fourth Edition, ELSEVIER, 2007

[41] Moon, S., " Aero-Structural Optimization of Divergence-Critical Wings", PhD Dissertation, University of Toronto, Canada, 2009

[42] MSC. Software Corporation, "MSC Nastran 2010, Quick Reference Guide", USA, 2010

[43] MSC. Software Corporation, "MSC Nastran FlightLoads and Dynamics User's Guide, Version 2006", Los Angeles USA, 2006

[44] MSC. Software Corporation, "MSC Nastran Version 68, Aeroelastic Analysis, User's Guide", Los Angeles, USA, 2004

[45] Park, G. J., "Equivalent Static Loads Method for Nonlinear Static Response Structural Optimization", LS-DYNA Forum, Bamberg 2010

[46] Patil, M. J., Hodges, D. H., and Cesnik, C. E. S., "Characterizing the Effects of Geometrical Nonlinearities on Aeroelastic Behavior of High Aspect Ratio Wings", In Proceedings of the International Forum on Aeroelasticity and Structual Dynamics, 1999

[47] Patil, M. J. and Hodges, D. H., "Flight Dynamics of Highly Flexible Flying Wings", Journal of Aircraft, 2006

[48] Pereira, P., Almeida, L., Suleman, A., Bond, V., Canfield, R.A. and Blair, M., "Aeroelastic Scaling and Optimization of a Joined Wing Aircraft Concept", AIAA/ASME/ASCE/AHS/ASC Structures, Structural Dynamics and Materials Conference, 2007

[49] Pittit, C. L., Cranfield, R. A. and Ghanem, R., " Stochastic Analysis of a Aeroelastic System", New York : ASCE, 2002

[50] Ricciardi, P. A., "Geometrically Nonlinear Aeroelastic Scaling", Phd Dissertation, Faculty of the Virginia Polytechnic and State University, Blacksburg, Virginia, 2013

[51] Richards, J., "An Experimental Investigation of a Joined Wing Aircraft Configuration Using Flexible, Reduced Scale Flight Test Vehicles", Phd Dissertation, University of Victoria, Victoria, BC, Canada, 2014

[52] Richards, J. and Suleman, A., "Aeroelastic Scaling of Unconventional Joined Wing Concept for Exploration of Gust Load Response", IFASD-2009-177

[53] Richards, J., Suleman, A., Canfield, R. A. and Blair M., " Design of a Scaled rpv for Investigation of Gust Response of Joined-Wing Sensorcraft". AIAA/ASME/ASCE/AHS/ASC Structures, Structural Dynamics and Materials Conference, AIAA 2009-2218, 2009

[54] Rodden, W. P., Taylor, P. F. and McIntosh, S. C. Jr., "Further Refinement of the Nonplanar Aspects of the Subsonic Doublet-Lattice Lifting Surface Method", 20th Congress of the International Council of the Aeronautical Sciences, Paper ICAS 96-2.8.2, 1996

[55] Rodden, W. P., Taylor, P. F., McIntosh, S. C. Jr. and Baker, M. L., "Further Convergence Studies of the Enhances Subsonic Doublet-Lattice Oscillatory Lifting Surface Method", International Forum on Aeroelasticity and Structural Dynamics, 1999

[56] Sitx, J. J. BS, "Aeroelastic Analysis of a Joined-Wing Sensorcraft", Air force Institute of Technology, Wright-Patterson Air Force Base, Ohio, 2004

[57] Statoil, " Jet A-1 - Product information", [online], 2014, [Cited: May 21, 2014], http://www.statoilaviation.com/en_EN/pg1332347009500/ar1334072083204/statoilAviation/fuel_jeta1.html

[58] Strutt, J. W. (Lord Rayleigh), "The Theory of Sound", Macmillan, 1877

[59] Van Schoor, M. C. and Von Flotow, A. H., "Aeroelastic Characteristics of a Flexible Aircraft", Journal of Aircraft, vol 27, 1990

[60] Waszak, M. R. and Schmidt, D. K., "Flight dynamics of Aeroelastic Vehicles", Journal of Aircraft, vol 25, 1988

[61] Wright, J. R. and Cooper, J. E., "Introduction to Aircraft Aeroelasticity and Loads", John Wiley & Sons, Ltd, England, 2007

Appendix A

WING		1st Section	2nd Section	3rd Section	4th Section	5th Section	6th Section	7th Section
Spar Width	lb [m]	0.001	0.001	0.001	0.001	0.001	0.001	0.001
	ub [m]	0.068	0.052	0.043	0.035	0.03	0.025	0.020
	x_front [m]	0.055	0.049	0.038	0.021	0.012	0.006	0.003
	x_rear [m]	0.048	0.047	0.035	0.022	0.009	0.006	0.002
Spar Height	lb [m]	0.001	0.001	0.001	0.001	0.001	0.001	0.001
	ub [m]	0.022	0.017	0.014	0.012	0.010	0.008	0.007
	x_front [m]	0.018	0.015	0.011	0.01	0.008	0.005	0.001
	x_rear [m]	0.018	0.016	0.009	0.008	0.007	0.005	0.001
Rung Diameter	lb [m]	0.001	0.001	0.001	0.001	0.001	0.001	0.001
	ub [m]	0.022	0.017	0.014	0.012	0.010	0.008	0.007
	x [m]	0.011	0.012	0.013	0.008	0.006	0.004	0.003
Lumped Masses	lb [kg]	0.001	0.001	0.001	0.001	0.001	0.001	0.001
	ub [kg]	0.150	0.150	0.150	0.150	0.150	0.150	0.150
	Leading edge [kg]	0.002	0.003	0.001	0.013	0.031	0.049	0.062
	$0.5 \cdot \bar{c}$ [kg]	0.080	0.110	0.121	0.086	0.089	0.078	0.037
	Trailing edge [kg]	0.004	0.008	0.003	0.005	0.001	0.081	0.031

PYLON		1st Section	2nd Section	3rd Section	4th Section	5th Section
Spar Width	lb [m]	0.001	0.001	0.001	0.001	0.001
	ub [m]	0.014	0.013	0.011	0.007	0.004
	x [m]	0.010	0.008	0.009	0.006	0.004
Spar Height	lb [m]	0.001	0.001	0.001	0.001	0.001
	ub [m]	0.005	0.004	0.004	0.003	0.002
	x [m]	0.002	0.003	0.002	0.001	0.001
Lumped Masses	lb [kg]	0.001	0.001	0.001	0.001	0.001
	ub [kg]	0.150	0.150	0.150	0.150	0.150
	$0 \cdot \bar{c}$ [kg]	0.001	0.001	0.003	0.002	0.001
	$0.5 \cdot \bar{c}$ [kg]	0.001	0.002	0.006	0.009	0.007
	$1 \cdot \bar{c}$ [kg]	0.003	0.002	0.002	0.001	0.001
Ribs	lb [mm]	0.001	0.001	0.001	0.001	0.001
	ub [mm]	0.004	0.004	0.004	0.004	0.004
	x [mm]	0.002	0.002	0.001	0.001	0.001

Table A1: Design variables for best design in Configuration 2, Method 2

WING		1st Section	2nd Section	3rd Section	4th Section	5th Section	6th Section	7th Section
Spar Width	lb [m]	0.001	0.001	0.001	0.001	0.001	0.001	0.001
	ub [m]	0.068	0.052	0.043	0.035	0.03	0.025	0.020
	x_front [m]	0.048	0.039	0.033	0.020	0.011	0.006	0.003
	x_rear [m]	0.045	0.036	0.033	0.018	0.008	0.005	0.002
Spar Height	lb [m]	0.001	0.001	0.001	0.001	0.001	0.001	0.001
	ub [m]	0.022	0.017	0.014	0.012	0.010	0.008	0.007
	x_front [m]	0.015	0.014	0.009	0.009	0.005	0.004	0.002
	x_rear [m]	0.015	0.013	0.010	0.008	0.005	0.003	0.001
Rung Diameter	lb [m]	0.001	0.001	0.001	0.001	0.001	0.001	0.001
	ub [m]	0.022	0.017	0.014	0.012	0.010	0.008	0.007
	x [m]	0.011	0.011	0.013	0.008	0.005	0.004	0.003
Lumped Masses	lb [kg]	0.001	0.001	0.001	0.001	0.001	0.001	0.001
	ub [kg]	0.150	0.150	0.150	0.150	0.150	0.150	0.150
	Leading edge [kg]	0.006	0.012	0.074	0.082	0.071	0.009	0.004
	$0.5 \cdot \bar{c}$ [kg]	0.061	0.092	0.105	0.125	0.108	0.008	0.006
	Trailing edge [kg]	0.005	0.007	0.005	0.011	0.009	0.004	0.002

PYLON		1st Section	2nd Section	3rd Section	4th Section	5th Section
Spar Width	lb [m]	0.001	0.001	0.001	0.001	0.001
	ub [m]	0.014	0.013	0.011	0.007	0.004
	x [m]	0.009	0.007	0.005	0.003	0.003
Spar Height	lb [m]	0.001	0.001	0.001	0.001	0.001
	ub [m]	0.005	0.004	0.004	0.003	0.002
	x [m]	0.002	0.002	0.001	0.001	0.001
Lumped Masses	lb [kg]	0.001	0.001	0.001	0.001	0.001
	ub [kg]	0.150	0.150	0.150	0.150	0.150
	$0 \cdot \bar{c}$ [kg]	0.001	0.003	0.008	0.004	0.005
	$0.5 \cdot \bar{c}$ [kg]	0.005	0.008	0.011	0.014	0.01
	$1 \cdot \bar{c}$ [kg]	0.003	0.004	0.005	0.008	0.007
Ribs	lb [m]	0.001	0.001	0.001	0.001	0.001
	ub [m]	0.004	0.004	0.004	0.004	0.004
	x [m]	0.002	0.002	0.001	0.001	0.001

Table A2: Design variables for modern approach (ESL)